DESIGN OF HARDWARE ARCHITECTURE FOR IMPLEMENTATION OF REAL TIME DEHAZING ALGORITHMS OF WEATHER DEGRADED IMAGES

THESIS SUBMITTED BY

AVRA GHOSH

DOCTOR OF PHILOSOPHY (Engineering)

Under the supervision of

Dr. Sheli Sinha Chaudhuri

Professor

Department of Electronics and Telecommunication Engineering

Jadavpur University

Kolkata - 700032

West Bengal, India

December, 2025

JADAVPUR UNIVERSITY
KOLKATA-700032, INDIA

TITLE OF THE THESIS:

DESIGN OF HARDWARE ARCHITECTURE FOR IMPLEMENTATION OF REAL TIME DEHAZING ALGORITHMS OF WEATHER DEGRADED IMAGE

NAME, DESIGNATION & INSTITUTION OF THE SUPERVISORS:

- **Dr. SHELI SINHA CHAUDHURI**
  Professor,
  Department of Electronics and Telecommunication Engineering,
  Jadavpur University, Kolkata-700032

LIST OF PUBLICATIONS:

a) JOURNAL:

1. **A. Ghosh**, A. Ali and S. S. Chaudhuri, "**Novel Parametric Based Time Efficient Portable Real-Time Dehazing System**". Journal of Real-Time Image Processing. https://doi.org/10.1007/s11554-023-01283-x,**Impact Factor- 3.0**

2. A. Ali, **A. Ghosh** and S. S. Chaudhuri, "**LIDN: A Novel Light Invariant Image Dehazing Network**". Engineering Applications of Artificial Intelligence. https://doi.org/10.1016/j .engappai.2023.106830. 2023, **Impact Factor- 8.0**

3. **A. Ghosh**, S. Bhowmick and S. S. Chaudhuri, "**Real-Time Image Dehazing via a Novel Parallel Architecture: An Empirical Comparison of Hardware Platforms**". Journal of Signal, Image and Video Processing. Communicated,**Impact Factor- 2.0**

4. **A. Ghosh**, A. Ali and S. S. Chaudhuri, "**A Review of Image Quality Assessment Metrics for Haze Removal: Bridging Objective and Human Perception**". Journal of Real-Time Image Processing. Submitted,**Impact Factor- 3.0**

b) COPYRIGHT:

1. **A Ghosh**, A. Ali, S. Banerjee and S. S. Chaudhuri, "**No Reference Dataset for Daytime and Nighttime Synthetic Hazy Image**". Diary No. 18933/2023-CO/L. ROC Number: L-133885/2023. Registered

c) CONFERENCE:

1. **A. Ghosh**, S. Roy and S. Sinha Chaudhuri, **"Hardware Implementation of Image Dehazing Mechanism using Verilog HDL and Parallel DCP**," 2020 IEEE Applied Signal Processing Conference (ASPCON), Kolkata, India, 2020, pp. 283-287, doi: 10.1109/ASPCON49795.2020.9276702.

2. **A. Ghosh** and S. S. Chaudhuri, **"IOT based Portable Image Dehazing Machine,"** 2021 8th International Conference on Signal Processing and Integrated Networks (SPIN), Noida, India, 2021, pp. 31-35, doi: 10.1109/SPIN52536.2021.9565998.

3. U. Biswas, A. Karmakar, **A. Ghosh** and S. S. Chaudhuri, **"Enhancing Image Clarity in Real Time: An Automated Gamma Correction Approach for Dehazing,"** 2023 7th International Conference on Electronics, Materials Engineering and Nano-Technology (IEMENTech), Kolkata, India, 2023, pp. 1-6, doi: 10.1109/IEMENTech60402.2023.10423457.

4. U. Biswas, **A. Ghosh**, S. Chakraborty and S. S. Chaudhuri, **"Power Law-Based Night-Time Image Dehazing Fused with Luminance Mapping for Enhanced Visibility,"** 2023 7th International Conference on Electronics, Materials Engineering and Nano-Technology (IEMENTech), Kolkata, India, 2023, pp. 1-6, doi: 10.1109/IEMENTech60402.2023.10423451.

5. U. Biswas, **A. Ghosh**, S. Chakraborty and S. S. Chaudhuri, **"Power Law-Based Night-Time Image Dehazing Fused with Luminance Mapping for Enhanced Visibility,"** 2023 7th International Conference on

Electronics, Materials Engineering and Nano-Technology (IEMENTech), Kolkata, India, 2023, pp. 1-6, doi: 10.1109/IEMENTech60402.2023.10423451.

6. Dey, A., **Ghosh, A.**, Chaudhuri, S.S. (2023). **Image Restoration from Weather Degraded Images Using Markov Random Field**. In: Roy, S., Sinwar, D., Dey, N., Perumal, T., Tavares, J.M.R.S. (eds) Innovations in Computational Intelligence and Computer Vision. ICICV 2022. Lecture Notes in Networks and Systems, vol 680. Springer, Singapore. `https://doi.org/10.1007/978-981-99-2602-2_6`

7. **Ghosh, A**., Dey, A., Chaudhuri, S.S. (2023). **A Fast Restoration of Weather Degraded Images.** In: Das, N., Binong, J., Krejcar, O., Bhattacharjee, D. (eds) Proceedings of International Conference on Data, Electronics and Computing. ICDEC 2022. Algorithms for Intelligent Systems. Springer, Singapore. `https://doi.org/10.1007/978-981-99-1509-5_21`

8. **A. Ghosh**, S. Roy, S. Chatterjee, and S. S. Chaudhuri, "HazeClear: A Hardware-Accelerated ASIC for Real-Time Video Dehazing," *2026 39th International Conference on VLSI Design and 25th International Conference on Embedded Systems (VLSID)*, Kolkata, India, 2026 (Accepted).

LIST OF PRESENTATIONS IN INTERNATIONAL CONFERENCES:

1. U. Biswas, **A. Ghosh**, S. Chakraborty and S. S. Chaudhuri, **"Power Law-Based Night-Time Image Dehazing Fused with Luminance Mapping for Enhanced Visibility,"** 2023 7th International Conference on Electronics, Materials Engineering and Nano-Technology (IEMENTech), Kolkata, India, 2023, pp. 1-6, doi: 10.1109/IEMENTech60402.2023.10423451.

2. Dey, A., **Ghosh, A.**, Chaudhuri, S.S. (2023). **Image Restoration from Weather Degraded Images Using Markov Random Field**. In: Roy, S., Sinwar, D., Dey, N., Perumal, T., Tavares, J.M.R.S. (eds) Innovations in Computational Intelligence and Computer Vision. ICICV 2022. Lecture Notes in Networks and Systems, vol 680. Springer, Singapore. `https://doi.org/10.1007/978-981-99-2602-2_6`

3. **A. Ghosh** and S. S. Chaudhuri, **"IOT based Portable Image Dehazing Machine,"** 2021 8th International Conference on Signal Processing and Integrated Networks (SPIN), Noida, India, 2021, pp. 31-35, doi: 10.1109/SPIN52536.2021.9565998.

4. **A. Ghosh**, S. Roy, S. Chatterjee, and S. S. Chaudhuri, "HazeClear: A Hardware-Accelerated ASIC for Real-Time Video Dehazing," *2026 39th International Conference on VLSI Design and 25th International Conference on Embedded Systems (VLSID)*, Kolkata, India, 2026 (Accepted).

PROFORMA – 1

Statement of Originality

I **AVRA GHOSH** registered on **28/04/2022** do hereby declare that this thesis entitled - **"DESIGN OF HARDWARE ARCHITECTURE FOR IMPLEMENTATION OF REAL TIME DEHAZING ALGORITHMS OF WEATHER DEGRADED IMAGES"** contains literature survey and original research work done by the undersigned candidate as part of Doctoral studies.

All information in this thesis have been obtained and presented in accordance with existing academic rules and ethical conduct. I declare that, as required by these rules and conduct, I have fully cited and referred all materials and results that are not original to this work.

I also declare that I have checked this thesis as per the "Policy on Anti Plagiarism, Jadavpur University, 2019", and the level of similarity as checked by iThenticate software is **7 %**.

Avra Ghosh

Signature of Candidate
Date: 04/12/2025

S. S. Chaudhuri 4/12/25

Prof. Sheli Sinha Chaudhuri
Supervisor
Department of Electronics and Telecommunication Engineering
Jadavpur University

Dr. Sheli Sinha Chaudhuri
Professor
Dept. of Electronics & Tele-Comm. Engg.
JADAVPUR UNIVERSITY
Kolkata-700 032

PROFORMA – 2

CERTIFICATE FROM THE SUPERVISOR

This is to certify that the thesis entitled **"DESIGN OF HARDWARE ARCHITECTURE FOR IMPLEMENTATION OF REAL TIME DEHAZING ALGORITHMS OF WEATHER DEGRADED IMAGES"** submitted by **Mr. Avra Ghosh**, who got his name registered on **28/04/2022** for the award of Ph. D. (Engg.) degree of Jadavpur University is absolutely based upon his own work under the supervision of **Prof. SHELI SINHA CHAUDHURI** (Dept. of E.T.C.E., JU) and that neither his thesis nor any part of the thesis has been submitted for any degree/ diploma or any other academic award anywhere before.

S. S. Chaudhuri 9/12/25

Prof. Sheli Sinha Chaudhuri
Supervisor
Department of Electronics and
Telecommunication Engineering
Jadavpur University

Dr. Sheli Sinha Chaudhuri
Professor
Dept. of Electronics & Tele-Comm. Engg.
JADAVPUR UNIVERSITY
Kolkata-700 032

ACKNOWLEDGEMENTS

I am profoundly grateful to the individuals whose contributions have been instrumental in bringing this thesis to fruition. Foremost, I extend my heartfelt appreciation and admiration to my esteemed supervisor, Prof. Sheli Sinha, whose unwavering guidance, unwavering support, attentive care, invaluable advice, and consistent oversight have been indispensable throughout this journey.

I also wish to convey my sincere gratitude to Prof. Mrinal Kanti Naskar, Professor Sayan Chatterjee, Assistant Professor Abhijit Chandra and Professor Sudhabindu Ray, Head of the Department of Electronics and Communication Engineering at Jadavpur University, , for their constant inspiration, support, and invaluable suggestions throughout the course of this thesis work. Additionally, I am grateful to the faculty and staff members of the Department of Electronics and Telecommunication Engineering at Jadavpur University for their support during my research endeavors.

I extend my thanks to Dr. Sangita Roy, Dr. Chinmoy Ghorai and Dr. Ratna Chakrabarty for their unwavering support and invaluable suggestions, which have been instrumental in the successful completion of my research. I am also grateful to my fellow researchers, Mr. Asfak Ali, for his steadfast support during the research process. I am deeply appreciative of the encouragement and camaraderie extended by my fellow researchers, including Sumanta Bhowmick, Simontini Roy, Suvojit Acharjee, Uma Biswas, Ajoy dey, and Aurgha Karmakar of the Computer Vision and Data Analytic Laboratory and IoT and Embedded ML Laboratory at Jadavpur University.

Lastly, I owe an immense debt of gratitude to my beloved Father (Late Santi Kumar Ghosh), Mother (Ms. Sujata Ghosh), Sister (Mrs. Juin Ghosh), Wife (Mrs. Keka Jana), Son (Master Alik Ghosh), and other close friends whose unwavering love, support, encouragement, well-wishes, and inspiration have been the driving force behind the completion of this thesis.

Avra Ghosh 04/12/2025

Avra Ghosh
Electronics & Telecommunication Engineering
Electronics & Telecommunication Engineering Department
Jadavpur University
Kolkata-32, West Bengal, India

Abstract

Visibility degradation due to haze is a major challenge in outdoor computer vision systems, significantly impacting the performance of downstream tasks such as object detection, tracking, and scene understanding. This thesis presents a comprehensive investigation into video dehazing techniques, with an emphasis on restoring visibility and contrast in real-time video streams under varying atmospheric conditions. The study classifies video dehazing methodologies into three primary categories: multi-image aggregation methods, prior-based approaches, and data-driven techniques. Multi-image aggregation methods exploit temporal coherence and scene redundancy across frames to improve dehazing accuracy, while prior-based approaches rely on handcrafted assumptions such as the dark channel prior, color-lines, and atmospheric light models. Data-driven methods, in contrast, leverage deep learning architectures to implicitly learn haze-relevant features from annotated datasets, offering significant advantages in generalizability and performance. A key contribution of this work lies in the proposal of an efficient parallel method to implement the real-time processing in embedded system and its critical evaluation and comparative analysis of these techniques in both offline and real-time settings. Extensive experimentation is conducted on publicly available and custom-collected hazy video datasets. The study proposes a unified evaluation framework encompassing PSNR, SSIM, perceptual quality metrics, and processing latency to assess the trade-offs between visual quality and computational efficiency. To bridge the gap between algorithmic sophistication and real-world deployment, this thesis explores the integration of video dehazing algorithms with edge-computing platforms. In particular, it demonstrates the effectiveness of the PYNQ (Python Productivity for Zynq) platform, which offers hardware-software co-design capabilities to accelerate dehazing pipelines. Experimental results reveal that the PYNQ implementation not only achieves state-of-the-art visual restoration but also meets the latency constraints of real-time applications such as autonomous navigation and surveillance.

Keywords: Dehazing, Parallel Processing, Embedded Vision, Embedded Sytem, Verilog, Hardware Accelerator

Table of Contents

Front Page i

Declaration iii

Statement of Originality vii

Certificate from the supervisor/s ix

Acknowledgment xi

Abstract xiii

Table of Contents xv

List of Figures xxi

List of Tables xxv

1 INTRODUCTION 1

1.1 Introduction . . . 3
1.1.1 Components of the Image Scattering Model . . . 4
1.1.2 Mathematical Representation . . . 4
1.1.3 Effects on Human Perception . . . 5
1.2 Applications of Image Dehazing . . . 5
1.2.1 Video Surveillance . . . 6
1.2.2 Intelligent Transportation Systems . . . 6
1.2.3 Underwater Image Enhancement . . . 7
1.2.4 Remote Sensing . . . 7
1.3 Issues and Challenges of Image Dehazing . . . 7
1.3.1 Under-Enhancement and Over-Enhancement . . . 7
1.3.2 Halo Artifacts and Noise Amplification . . . 8
1.3.3 Handling Varying and Dense Haze Conditions . . . 8
1.3.4 Parameter Sensitivity and Adaptivity . . . 8
1.3.5 Real-Time Dehazing . . . 9
1.4 **Motivation** . . . 9
1.5 Scope of This Thesis . . . 10
1.5.1 Haze Removal . . . 10
1.5.2 Lightweight Haze Removal for Real-Time Applications . . . 11
1.5.3 Hardware Implementation for Real-Time Processing . . . 12

1.6 Thesis Overview 12

2 LITERATURE SURVEY **15**
2.1 Image Dehazing Methods 17
2.2 Image Enhancement Techniques 18
2.3 Image Fusion Approaches 20
2.4 Restoration-based Methods 21
2.5 Polarization-based Methods 24
2.6 Terminator Line-based Approaches 24
2.7 Learning-based Methods 25
2.8 Comparative Analysis 26
2.9 Research Gaps 27
2.10 **Previous Work for Hardware Implementation** 27

3 Parameter Analysis **31**
3.1 Introduction 33
3.2 Related Work 34
3.3 Types of IQA Metrics and Mathematical Formulations 35
3.3.1 SSIM 35
3.3.2 MSE 37
3.3.3 PSNR 38
3.3.4 Correlation 39
3.3.5 Multi-scale structural similarity index (MS-SSIM) 40
3.3.6 MDSI 41
3.3.7 LPIPS 42
3.3.8 GMSD 43
3.3.9 BRISQUE 44
3.3.9.1 Equation for MSCN Features 45
3.3.9.2 BRISQUE Quality Score 45
3.3.10 NIQE 46
3.3.10.1 Natural Image Quality Evaluator (NIQE) 46
3.3.10.2 NIQE Feature Extraction 46
3.4 Performance Comparison 47
3.4.1 Dataset Selection 48
3.4.2 Performance Criteria 49
3.4.3 Correlation with Human Perception 50
3.4.3.1 Performance on No-Haze Images 50
3.4.3.2 Performance on Low-Haze Images 51
3.4.3.3 Performance on Dense Haze Images 53
3.4.3.4 Performance on Night Haze Images 54
3.4.4 Sensitivity to Distortions 55
3.5 GUI 55
3.6 Challenges and Limitations 57
3.7 Future Directions 58
3.8 **Discussion** 60

4 Parallel Processing of Atmospheric Light and Transmission Coefficient for Image Dehazing 63
4.1 Introduction . . . 65
4.1.1 Contribution of the Chapter . . . 65
4.2 Method 1 . . . 65
4.2.1 Proposed Method . . . 67
4.2.2 Contrast Enhancement . . . 68
4.2.3 Experimental Observations . . . 68
4.3 Method 2 . . . 72
4.3.1 Markov Random Field-Based Refinement . . . 72
4.3.2 Experimental Results . . . 73
4.4 Method 3 . . . 74
4.4.1 CLAHE Adoption including gamma correction(manual to automate) . . . 74
4.4.1.1 Contrast-Limited Adaptive Histogram Equalization (CLAHE) 74
Adaptive Histogram Equalization (AHE) . . . 74
Contrast-Limited Adaptive Histogram Equalization (CLAHE) 77
4.4.1.2 Spatial Domain Techniques and Gamma Correction . . . 78
Power-Law Transformation (Gamma Correction) . . . 78
4.4.1.3 Automatic Gamma Correction Formula . . . 78
4.4.1.4 Significance of Automatic Gamma Calculation . . . 79
4.5 Experimental Results . . . 81
4.5.1 Qualitative Comparison . . . 81
4.5.2 Quantitative Comparison . . . 81
4.6 Discussion . . . 83

5 Night Time Image Dehazing 85
5.1 Introduction . . . 87
5.2 Nighttime Haze Model and Image Enhancement Techniques . . . 88
5.2.1 Nighttime Haze Model . . . 88
5.2.2 Key Image Enhancement Techniques . . . 89
5.2.2.1 Guided Filtering . . . 89
5.2.2.2 Reflectance Mapping . . . 90
5.2.3 Estimating Atmospheric Light and Transmission . . . 90
5.3 This Method . . . 91
5.3.1 Gamma Mapping for Luminance Reduction . . . 91
5.3.2 Luminance and Lower Luminance Mapping . . . 92
5.4 Experimental Results . . . 93
5.4.1 Qualitative Comparison . . . 93
5.5 Discussion: . . . 93

6 Deep Learning Approach for Time invariant Image Dehazing 97
6.1 Introduction . . . 99
6.2 Contributions . . . 100
6.3 Background . . . 100
6.4 Proposed Method . . . 102
6.4.1 Data Pre-processing . . . 102

6.4.2 Model Architecture . . . 103
6.4.2.1 Feature Extraction Layer . . . 105
6.4.2.2 Medium Transmission Estimation . . . 105
6.4.2.3 Global Atmospheric Light Estimation Using Deep Networks . . . 107
6.4.2.4 Encoder-Decoder Integration Layer . . . 107
6.4.3 Model Training Procedure . . . 109
6.4.3.1 Datasets for Training and Evaluation . . . 109
6.4.3.2 Loss Function Strategy . . . 110
6.4.3.3 Hyperparameter Configuration and Training Setup . . . 116
6.5 Experimental Evaluation . . . 120
6.5.1 Quantitative Analysis . . . 120
6.5.2 Quantitative Evaluation . . . 121
6.5.3 Ablation Study . . . 121
6.6 Chapter Conclusion . . . 122

7 Hardware Implementation for Video Processing 123
7.1 Introduction . . . 125
7.1.1 Contributions . . . 125
7.1.1.1 Introduction of SATVAL . . . 126
7.1.1.2 SATVAL Video Dataset . . . 126
7.1.1.3 Real-Time Hardware Implementation . . . 126
7.1.1.4 Empirical Comparison of the algorithm in Different Hardware Accelerator . . . 126
7.2 Hardware Description . . . 126
7.2.1 Raspberry Pi . . . 127
7.2.2 PYNQ-Z2 . . . 127
7.2.3 Jetson Nano . . . 129
7.3 Method1: Video Dehazing in IoT Device . . . 130
7.4 SATVAL DataSet . . . 134
7.4.1 Acquisition . . . 134
7.5 Method3: Empirical Comparison between Different Hardware Accelerator 136
7.5.1 Atmospheric Light Estimation . . . 136
7.5.2 Transmission Guide . . . 139
7.5.2.1 Mean Calculations . . . 139
7.5.2.2 Covariance and Variance Calculations . . . 139
7.5.2.3 Linear Coefficients . . . 139
7.5.2.4 Mean of Coefficients . . . 140
7.5.2.5 Filtered Image Output . . . 140
7.5.3 Parallel Execution and Synchronization: . . . 140
7.5.4 Qualitative Analysis: . . . 141
7.5.5 Quantitative Analysis: . . . 142
7.6 Discussion: . . . 145

8 ASIC Implementation of Image Dehazing Algorithm 149
8.1 Introduction . . . 151
8.2 Background . . . 152

8.2.1 Dark Channel Calculation 153
8.2.2 Transmission Calculation 153
8.2.3 Dehazing Equation 153
8.3 Proposed Architecture 154
8.4 Experimental Result 154
8.5 Discussion 159

9 CONCLUSION AND FUTURE SCOPE 161
9.1 Conclusion 163
9.2 Limitations 164
9.3 Future Scope 165

References 167

List of Figures

1.1 Haze formation logic 3

1.2 Images of (a) fog, (b) mist, (c) haze, (d) Source: air pollutants, (e) Source: farming, (f) Source: wildfires 4

1.3 Applications of image dehazing: (a) Video surveillance, (b) Fog-related road accidents, (c) Road transportation, (d) Railway transportation, (e) Air transportation, (f) Underwater image enhancement, (g) Remote sensing. 6

2.1 Quantity of Papers Published in Recent Years 17

2.2 Different Image Dehazing Types 18

3.1 Image Parameter Calculation Based on Feature Extraction 33

3.2 Correlation with Human Perception in no haze images 49

3.3 Correlation with Human Perception in low haze images 50

3.4 Correlation with Human Perception in dense haze images 51

3.5 Correlation with Human Perception in night haze images 51

3.6 Qualitative and quantitative comparison using parameters. 52

3.7 Qualitative and quantitative comparison using parameters. 53

3.8 Image Parameter Calculation Graphical User Interface 56

3.9 Image Parameter Calculation Graphical User Interface for Calculation Page 57

4.1 Flowchart of the Proposed Dehazing Algorithm 68

4.2 Original image,Image after using CLAHE in the figure 77

4.3 A city view, Image after using CLAHE in the figure 77

4.4 Images with gamma values of 1.0, 1.5, and 2.0 respectively 78

4.5 Qualitative comparison: Top - dark channel prior-based methods; Middle - transmission-based method; Bottom - outputs from the proposed method 79

4.6 Quantitative comparison: Top - dark channel prior-based methods; Middle - color attenuation prior-based method; Bottom - proposed method . . 80

4.7 City view after applying CLAHE and gamma correction 80

4.8 Outdoor view with CLAHE and gamma correction enhancement 81

4.9 Urban scene with CLAHE and gamma correction 81

5.1 The nighttime haze model 89

5.2 Reflectance mapping and Atmospheric Light & Transmission Estimation . 91

5.3 Nighttime hazy image with high luminance 91

5.4 Luminance mapping using gamma correction 93

5.5 Qualitative results input images. Upper half: comparison to dark channel prior-based methods; middle half:histogram eqalization and Zhangs method ,bottom half: This apporoch of the nighttime images 95

6.1 Illustration of the same scene captured during nighttime and daytime, highlighting variations in light scattering and visibility under different illumination conditions. 99

6.2 Output of the proposed model train in YIQ, RGB and LAB color space, where in LAB color space the proposed model shows best results. 101

6.3 The overall framework of the proposed LIDN method. The network consists of four sub-blocks Feature Extractor, Medium Transmission Extraction, Deep Global Atmospheric Light Estimator and Encoder Decoder head. 103

6.4 Structural Representation of the Medium Transmission Extractor with Feature Map Annotations. 104

6.5 BReLU Activation Function: Representation of Maximum and Minimum Transmission in Dehazing 104

6.6 Extracted Transmission Map $t(x)$ from the Medium Transmission Extractor . . . 104

6.7 Schematic Representation of the Encoder-Decoder Architecture: Feature Maps Indicated in Boxes with Channel Count Annotated on Top, and Operations Depicted via Arrows . . . 105

6.8 Haze-relevant feature maps extracted under varying lighting conditions as computed by Equation 6.15. The right side illustrates the network inputs. 106

6.9 Results of dehazing with the proposed LIDN architecture using MSSIM, PSNR, SSIM, MSE, and Quadruplet Loss under various λ configurations. 108

6.10 Training and validation loss curve for the LIDN model across LAB, RGB, and YIQ color spaces. . . . 110

6.11 Training and validation loss curves for LIDN, trained using multiple loss functions including MSE, PSNR, SSIM, MSSIM, and Quadruplet Loss for different λ configurations. . . . 111

6.12 Comparative Analysis of the Proposed Method and Existing Models on Daytime Images from the Daytime and Nighttime Dehazing Benchmarking Database. . . . 114

6.13 Comparative Analysis of the Proposed Method and Existing Models on Nighttime Images from the Daytime and Nighttime Dehazing Benchmarking Database . . . 115

6.14 Qualitative Comparison of Image Dehazing Techniques on the SOTS-Mix Dataset. The first two rows represent indoor images, while the last two rows correspond to outdoor images. The first column displays the hazy input images, the second-to-last column presents the corresponding ground truth, and the final column showcases the dehazed results. . . . 116

7.1 Experimental setup with Raspberry Pi Model 4B . . . 127

7.2 PYNQ-Z2 Board . . . 128

7.3 Jetson Nano Board . . . 130

7.4 Geometric representation of the HSV color model . . . 131

7.5 Different haze quality in different positions on an image and also the saturation and value components are different for these positions as well. . 132

7.6 Flow chart of proposed dehazing algorithm using Raspberry Pi. Step-by-step procedure. 133

7.7 Flow Diagram for Proposed Method 138

8.1 Circuit Diagram for Image Dehazing Algorithm 154

List of Tables

2.1 Comparison of Dehazing Techniques 27

3.1 Quality Assessment Metrics 36

3.2 Comparison of Metrics Across Different Conditions 54

4.1 Comparison of Reference Image Quality Parameter for Images 69

4.2 Computational Complexity for proposed method 69

4.3 Experimental results for different videos in proposed 70

4.4 Qualitative Comparison with Different Algorithms 71

4.5 Quantitative Comparison with Different Algorithms for SSIM 71

4.6 Quantitative Comparison with Different Algorithms for MSE 71

4.7 Quantitative Comparison with Different Algorithms for PSNR(dB)(dB) . 72

4.8 Quantitative Comparison with Different Algorithms for Correlation 72

4.9 Comparison of Reference Image Quality Parameter for Images 74

4.10 Experimental results for different photos using this method 75

4.11 Qualitative Comparison with Different Algorithms 76

4.12 Quantitative PSNR(dB)/SSIM/CORR/MSE results of proposed approach 82

4.13 PSNR(dB) and MSE of proposed method vs. DCP, CAP 82

4.14 CORR and SSIM of proposed method vs. DCP, CAP 82

5.1 PSNR of This method vs. DCP, Histogram Equalization(H.E.), and Zhang's method 93

5.2 MSE of This method vs. DCP, Histogram Equalization(H.E.), and Zhang's method 94

5.3 SSIM of This method vs. DCP, Histogram Equalization(H.E.), and Zhang's method 94

5.4 CORR of This method vs. DCP, Histogram Equalization(H.E.), and Zhang's method 94

6.1 Configuration Details of the Deep Global Atmospheric Light Estimator Network 102

6.2 Hyper-parameter details for training LIDN 113

6.3 Performance Evaluation of the Proposed Method Against Existing Models on Daytime Images from the Daytime and Nighttime Dehazing Benchmarking Database. SSIM, MSSIM, PSNR, and MSE metrics are compared, with the top three results highlighted in red, blue, and green fonts, respectively. In most cases, the proposed model demonstrates superior performance over other existing methods. 115

6.4 Evaluation of SSIM, MSSIM, PSNR, and MSE Metrics for the Proposed Method Against Existing Models on **Nighttime Images** from the Daytime and Nighttime Dehazing Benchmarking Database. The top three results are highlighted in red, blue, and green fonts, respectively. In most cases, the proposed model outperforms other existing methods. 116

6.5 Evaluation of SSIM, MSSIM, PSNR, and MSE Metrics for the Proposed Method Against Existing Models on **Real Hazy Images** from the Daytime and Nighttime Dehazing Benchmarking Database. The top three results are highlighted in red, blue, and green fonts, respectively. In most cases, the proposed model demonstrates superior performance compared to existing methods. 117

6.6 Evaluation of SSIM, MSSIM, PSNR, and MSE Metrics for the Proposed Method Against Existing Models on **Synthetic Hazy Images** from the Daytime and Nighttime Dehazing Benchmarking Database. The top three results are highlighted in red, blue, and green fonts, respectively. In most cases, the proposed model outperforms other existing methods. 117

6.7 Performance Comparison of SSIM, MSSIM, PSNR, and MSE for the Proposed Method Against Existing Models in the Daytime and Nighttime Dehazing Benchmarking Database. The top three results are highlighted using red, blue, and green fonts, respectively. In the majority of cases, the proposed model demonstrates superior performance compared to other existing methods. 117

6.8 Evaluation of SSIM, PSNR, MSE, and MSSIM Metrics for the Proposed Model on the **RESIDE6K** Database. The model is assessed using MSE, PSNR, MSSIM, and SSIM loss functions, as well as Quadruplet loss with varying values in the LAB color space. Additionally, its performance is analyzed with Quadruplet loss applied to RGB, LAB, and YIQ color spaces.. 118

6.9 Comparison of PSNR, SSIM, MSE, and MSSIM Metrics for the Proposed Method and Existing Models in the **I-HAZE, O-HAZE, Dense-HAZE, and NH-HAZE Databases**. The top three results are highlighted in red, blue, and green fonts, respectively. In most cases, the proposed model demonstrates superior performance compared to other existing methods. 118

6.10 Evaluation of PSNR, SSIM, MSE, MSSIM, and Overhead for the Proposed Method Compared to Existing Models in the **ITS, OTS** Database. The top three results are highlighted in red, blue, and green fonts, respectively. In most cases, the proposed model exhibits superior performance compared to other existing methods. 119

6.11 Evaluation of PSNR, SSIM, MSE, and MSSIM Metrics for the Proposed Method Compared to Existing Models in the **RESIDE6K** Database. The top three results are highlighted in red, blue, and green fonts, respectively. In most cases, the proposed model outperforms other existing methods. . 119

7.1 Comparison of Hardware for Image Dehazing 129

7.2 Performance comparison of the Video processing with different sizes of frames in Raspberry Pi Model. 134

7.3 Experimental Results for Different Videos in Raspberry Pi Model 135

7.4 Qualitative Comparison Of Different Dehazing Algorithms With SATVAL 136

7.5 Comparison of Reference Image Quality Parameter for nine Videos for SSIM (Structural Similarity Index),PSNR(dB)(dB)(Peak Signal to Noise Ratio), MSE(Mean Square Error), CORR(Correlation) 137

7.6 Comparison of SSIM for Different Algorithms 137

7.7 Comparison for PSNR(dB) Values for Different Algorithms 137

7.8 Comparison of MSE Values for Different Algorithms 137

7.9 Comparison of Correlation Values for Different Algorithms 138

7.10 Experimental results for different images in PYNQ Board and Jetson Nano 142

7.11 Qualitative Comparison Of Different Dehazing Algorithms With SATVAL 143

7.12 Comparison of Reference Image Quality Parameter for 10 Images Dehazed in PYNQ Board for PSNR(dB) (Peak Signal to Noise Ratio), MSE (Mean Square Error), CORR (Correlation), SSIM (Structural Similarity Index), MS-SSIM (multi-scale structural similarity index for motion detection), MDSI (Mean Deviation Similarity Index), LPIPS(d) (Learned Perceptual Image Patch Similarity) 144

7.13 Comparation of Reference Image Quality Parameter for 10 Images Dehazed in Jetson Nano for PSNR(dB) (Peak Signal to Noise Ratio), MSE (Mean Square Error), CORR (Correlation), SSIM (Structural Similarity Index), MS-SSIM (multi-scale structural similarity index for motion detection), MDSI (Mean Deviation Similarity Index), LPIPS(d) (Learned Perceptual Image Patch Similarity 145

7.14 PSNR(dB), MSE, correlation, SSIM, MSSIM, MDSI, and distortion (D) are among the image quality metrics for Raspberry Pi pictures that are displayed in the table. These measures assess the degree of distortion, structural similarity, and visual clarity. 145

7.15 Table 7.15 presents the processing times (in seconds) for dehazed images on three different hardware platforms: Jetson Nano (J Nano), PYNQ FPGA, and Raspberry Pi (R.PI). 146

8.1 Table of Circuit Diagrams with Headings 155

8.2 Experimental results for different images in PYNQ Board 157

8.3 Hardware Area and Timing Metrics for Dehazing System 158

8.4 Performance and Efficiency Comparison 158

8.5 Evaluation of Hardware Architectures on Chip 159

Type tet e

Chapter 1

INTRODUCTION

1.1 Introduction

Outdoor scene images often experience degradation due to adverse weather conditions, where atmospheric phenomena such as fog, haze, mist, vog, dust, and industrial pollutants significantly reduce visibility. The presence of airborne particles causes light scattering, resulting in lower contrast, faded colors, and reduced sharpness, making distant objects appear unclear. This challenge has gained growing attention in recent research due to its significant impact on image clarity and scene perception.

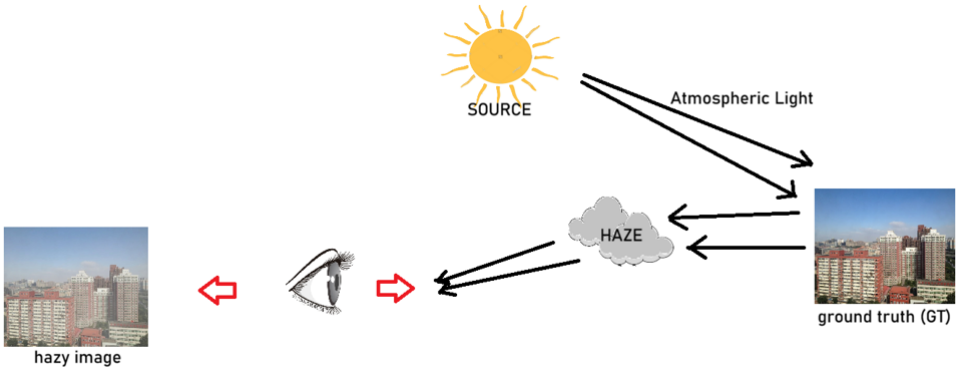

FIGURE 1.1: Haze formation logic

The **image scattering model** shown in Figure 1.1 explains how light interacts with atmospheric particles, leading to haze formation and reduced image clarity. As light travels from a scene to the observer (or a camera), it undergoes **scattering** due to small airborne particles such as dust, water droplets, and pollutants. This scattering process alters the intensity and color of the light, resulting in a hazy appearance. Fog, mist, and haze are atmospheric phenomena that degrade image visibility. Fog and mist occur due to the presence of moisture in the air in the form of water droplets or wet particles. While both terms describe similar conditions, the distinction lies in visibility range: if visibility drops below 1 km, it is termed as fog; if it extends beyond 1 km, it is referred to as mist. Haze, on the other hand, involves a different mechanism. It results from the suspension of extremely fine, dry particles—such as dust, smoke, air pollutants, or chemicals—in the air. Although these particles are too small to be seen by the naked eye, they significantly reduce image quality by diminishing visibility, contrast, and color accuracy. Haze typically reduces visibility to less than 1.25 miles. These dry particles originate from a variety of sources including agriculture, traffic emissions, industrial processes, and wildfires. Figure 1.2 (1) illustrates example images of fog, mist, and haze, along with common sources contributing to hazy image formation.

Type text hee



FIGURE 1.2: Images of (a) fog, (b) mist, (c) haze, (d) Source: air pollutants, (e) Source: farming, (f) Source: wildfires

1.1.1 Components of the Image Scattering Model

The formation of a hazy image can be attributed to two primary components: the **direct transmission** and the **airlight**. The direct transmission component refers to the portion of scene radiance $I(x)$, which is the original light emitted or reflected by an object, that reaches the observer without being scattered. However, due to atmospheric particles, only a fraction of this light is transmitted, governed by the **transmission coefficient** $t(x)$, which is dependent on the density of the haze. On the other hand, the **airlight component** arises from the scattering of ambient light—typically skylight—by atmospheric particles, which then reaches the observer's eye and adds to the captured image. This scattered light, denoted as A, increases the perceived brightness of the scene while simultaneously reducing contrast, causing distant objects to appear faded or washed out. The impact of airlight becomes more prominent as haze density increases, often involving multiple scattering events that further degrade visual clarity.

1.1.2 Mathematical Representation

The observed hazy image intensity at any pixel $I_h(x)$ can be expressed as:

$$I_h(x) = I(x) \cdot t(x) + A \cdot (1 - t(x)) \tag{1.1}$$

Here, $I_h(x)$ denotes the observed hazy image, while $I(x)$ represents the original scene radiance or the clear image. The term A stands for the global atmospheric light, also known as airlight, which contributes to the haze effect. The transmission map, denoted as $t(x) = e^{-\beta d(x)}$, quantifies the fraction of scene radiance that reaches the observer without being scattered. In this expression, β is the atmospheric scattering coefficient that reflects the density of haze in the scene, and $d(x)$ is the scene depth at pixel x, indicating the distance between the object and the observer.

1.1.3 Effects on Human Perception

Objects located farther from the observer exhibit lower transmission values due to increased atmospheric scattering, making them appear fainter and less distinct. As a result, colors become desaturated, and fine details are blurred, contributing to the overall hazy appearance of the scene. The characteristic bluish-white tint observed in foggy environments is primarily caused by Rayleigh scattering, wherein shorter wavelengths (such as blue) scatter more than longer wavelengths. This understanding forms the basis for dehazing algorithms, which focus on estimating the transmission map $t(x)$ and the global atmospheric light A to reconstruct a clearer image by reversing the effects of scattering.

Airbourne contamination in the atmosphere makes image quality poor, whitish and faded in colour. This type of low contrast image are not suitable for vision applications, leading to requirement of efficient contrast restoration techniques which would make the details of the image visible.

Over the years, numerous dehazing methods have been proposed that rely on various priors or assumptions to estimate scene depth information. However, the effectiveness of these approaches heavily depends on the accuracy of the assumed priors, which can result in challenges such as color distortion, incomplete haze removal, and halo artifacts. In addition, image enhancement-based dehazing techniques have been explored in the literature, which avoid the need for transmission estimation and its associated computational cost. However, these methods do not explicitly model the image degradation process, often leading to over- or under-enhancement, color oversaturation, loss of image details, and poor performance on dense hazy scenes. To address the limitations of both restoration- and enhancement-based methods, machine learning and deep learning approaches have been developed to estimate more accurate transmission maps. While these learning-based models have shown promising results, they require large datasets containing paired hazy and ground truth clear images, which are difficult to obtain in real-world scenarios. The related work section presents a comprehensive overview of recent dehazing techniques across these categories, highlighting their advantages and limitations.

1.2 Applications of Image Dehazing

Image dehazing is a significant area of research in computer vision, as it enhances visual clarity and contributes to the effectiveness of many downstream applications. The output

of dehazing algorithms often serves as a critical preprocessing step for various real-world vision tasks. Some of the key applications, illustrated in Fig. 1.3, are discussed below.

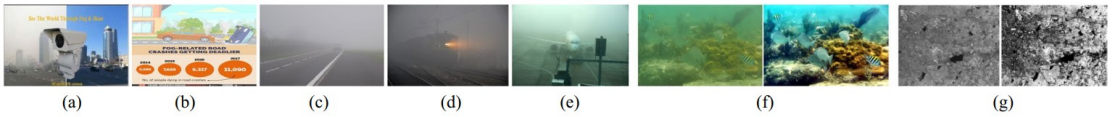

FIGURE 1.3: Applications of image dehazing: (a) Video surveillance, (b) Fog-related road accidents, (c) Road transportation, (d) Railway transportation, (e) Air transportation, (f) Underwater image enhancement, (g) Remote sensing.

1.2.1 Video Surveillance

Video surveillance systems are vital in the field of security and public safety. Their performance heavily depends on the clarity of the captured visual data. However, adverse weather conditions such as fog or haze significantly degrade video quality due to the scattering and absorption of light by atmospheric particles. Videos recorded in hazy conditions suffer from reduced visibility, making it difficult for law enforcement or security personnel to detect events or individuals, particularly during investigations. Therefore, integrating robust image dehazing techniques into surveillance systems is essential for maintaining operational effectiveness under varying environmental conditions.

1.2.2 Intelligent Transportation Systems

Fog and haze present serious challenges to transportation safety by impairing driver vision and increasing the likelihood of accidents. In recent years, fog-related road fatalities have risen dramatically. Thousands of accidents, injuries, and deaths occur annually on highways due to poor visibility. The issue is not limited to roadways; air and rail transport are also affected. Aircraft take-offs and landings become hazardous in foggy weather, often resulting in flight delays or cancellations. Likewise, railway operations face dangers as drivers may miss crucial signals, endangering passengers and crew. An intelligent transportation system enhanced by image dehazing can provide clearer visibility, helping to prevent accidents and improve safety across multiple modes of transport.

1.2.3 Underwater Image Enhancement

Underwater imaging is another domain where visibility is inherently poor. Light scattering by water molecules and suspended particles introduces a haze-like effect, significantly degrading image quality. Moreover, color distortions occur due to the differential attenuation of light wavelengths, often causing a strong bluish tint. To address these challenges, image dehazing is used as a preprocessing step in underwater vision systems, enabling clearer visualization of submerged objects and scenes for applications such as marine biology, archaeology, and underwater exploration.

1.2.4 Remote Sensing

Remote sensing involves capturing images from satellites or aircraft to extract information about terrestrial or atmospheric features. Due to the long distances involved, these images often suffer from atmospheric haze, which reduces clarity and contrast. Dehazing techniques are crucial in such cases to restore image quality and enhance the accuracy of further analysis. Beyond remote sensing, image dehazing is essential in several other fields including astronomy, medical imaging, agronomy, border surveillance, archaeology, and environmental monitoring.

Despite advances in optical hardware such as super-telephoto lenses with specialized coatings and filters to reduce contrast loss, these devices are often expensive, bulky, and impractical for routine use. As a result, computational image dehazing techniques have gained significant attention for their ability to restore visibility in a cost-effective and scalable manner.

1.3 Issues and Challenges of Image Dehazing

Although substantial progress has been made in the field of image dehazing, several significant challenges persist. These include issues such as color distortions, loss of structural information, excessive or insufficient enhancement, and limitations in handling varying haze conditions. A detailed discussion of these challenges is provided below.

1.3.1 Under-Enhancement and Over-Enhancement

One common issue in dehazing is the failure to accurately balance the enhancement level. Under-enhancement occurs when the algorithm does not remove haze effectively, leading

to minimal improvement in visibility. On the other hand, over-enhancement can lead to color distortions and alterations in haze-free regions. This often results in unnatural appearance, especially in dense haze areas with low contrast, where pixel saturation and over-darkening may occur. Effective dehazing techniques must enhance visibility in hazy regions while maintaining the natural appearance of unaffected areas.

1.3.2 Halo Artifacts and Noise Amplification

Patch-based transmission estimation, widely used in many dehazing methods, can introduce distortions when assumptions about uniform depth across image patches are violated. These inaccuracies can result in visual defects such as halo artifacts near depth discontinuities and unwanted noise amplification. While various post-processing techniques like guided filtering and regularization have been proposed to reduce these artifacts, they are not always completely effective. Moreover, dense haze tends to conceal noise in the original image, and dehazing algorithms may inadvertently amplify this noise, leading to degraded visual quality or even blurring.

1.3.3 Handling Varying and Dense Haze Conditions

Many existing dehazing approaches are designed primarily for daytime scenes with moderate haze and often fail under more complex conditions. These include dense fog, nighttime haze, and non-uniform or non-homogeneous haze distributions. For example, nighttime dehazing is particularly challenging due to the presence of multiple artificial light sources with varying intensities and colors. Traditional airlight estimation techniques, which rely on identifying the brightest pixels, become unreliable in such scenarios. Additionally, in very dense haze, scene reflectance becomes minimal, and the proportion of scattered light or airlight increases significantly, making accurate reconstruction extremely difficult.

1.3.4 Parameter Sensitivity and Adaptivity

The effectiveness of many dehazing methods depends heavily on manually set parameters such as patch size, gamma correction value, filter size, regularization terms, and scaling factors. These parameters are often tuned empirically for specific conditions and may not generalize well across images with different haze densities and distributions. For instance, a small patch size can underestimate transmission in bright regions,

causing over-enhancement, while a large patch size may increase computational complexity and introduce artifacts. Therefore, adaptive parameter selection strategies that respond to local image characteristics are necessary to improve dehazing robustness and performance.

1.3.5 Real-Time Dehazing

A significant limitation of current dehazing techniques is their computational cost, which hinders their application in real-time systems. Many algorithms involve computationally intensive steps, such as separate estimation of airlight and transmission maps or iterative refinement procedures. This makes them unsuitable for time-critical applications like autonomous navigation, live video surveillance, or augmented reality. Developing efficient algorithms with low latency and reduced complexity, possibly through joint estimation techniques and simplified models, remains a key area of ongoing research.

1.4 Motivation

Image dehazing is a critical and timely research area with growing significance across multiple real-world applications. Hazy environments caused by fog, mist, smoke, and pollution significantly impair visual quality by reducing contrast, obscuring details, and distorting colors. These challenges not only affect human perception but also degrade the performance of automated computer vision systems in safety-critical domains such as autonomous driving, aerial surveillance, remote sensing, and smart city monitoring.

The urgency of addressing haze-related visibility issues is particularly evident in India, where extreme weather conditions frequently affect transportation safety. According to a 2022 report by the Ministry of Road Transport and Highways, India recorded 34,262 road accidents caused by foggy and misty conditions, resulting in 14,583 deaths and 30,796 injuries. This marks a 9% increase in fatalities over the previous year, highlighting a pressing need for vision enhancement systems that can support safe mobility under low-visibility conditions. Experts advise drivers to refrain from speeding, use blinkers, and remain highly attentive during such conditionssource†Economic Times—but these human responses can be greatly aided by real-time visual restoration technology.

Traditional dehazing methods—often reliant on handcrafted priors—struggle with generalization and fail under complex or non-uniform haze. While deep learning-based models offer promise, they are typically data-hungry and computationally intensive,

limiting their deployment on edge devices.My work aims to bridge this gap by developing efficient, adaptive, and hardware-compatible dehazing techniques. By leveraging both physical haze modeling and lightweight learning-based enhancements, I seek to enable real-time dehazing for embedded platforms.

Ultimately, this research strives to improve visual clarity in real-world conditions, thereby enhancing safety, enabling robust automation, and supporting intelligent decision-making in haze-affected environments.

1.5 Scope of This Thesis

Hazy weather conditions pose a significant obstacle to the performance of computer vision systems, particularly in tasks involving object detection, tracking, and scene understanding. Visibility degradation due to haze not only affects image quality but also impairs the accuracy of downstream applications such as video surveillance, intelligent transportation systems, and autonomous navigation. Conventional dehazing techniques, while effective under controlled settings, often suffer from limited generalization across diverse illumination conditions and typically incur high computational costs, making them unsuitable for real-time deployment.

This research addresses these challenges by exploring both accuracy-driven and efficiency-oriented haze removal techniques. It focuses on developing robust, illumination-invariant dehazing solutions suitable for both still-image and video-based applications. The proposed approaches are evaluated under varying lighting and atmospheric conditions to ensure reliability and generalization.

In addition to algorithmic contributions, the work emphasizes practical implementation on embedded platforms to demonstrate real-time feasibility. By bridging the gap between high-quality dehazing and hardware-efficient execution, this research aims to contribute to the development of intelligent, vision-based systems capable of operating reliably in adverse weather scenarios.

1.5.1 Haze Removal

Among various adverse weather conditions, haze poses a significant challenge to object tracking and visual perception systems. Its presence often leads to degraded image quality, which adversely impacts the accuracy of computer vision tasks. Therefore,

developing robust haze removal techniques is essential to ensure reliable performance under such visibility-reducing conditions.

The majority of dehazing methods currently in use are designed exclusively for either daytime or nighttime circumstances, which limits their efficacy in a variety of lighting scenarios. The study presents the Light Invariant Dehazing Network (LIDN) (2), an end-to-end CNN architecture made up of four main modules: an encoder-decoder, a feature extractor, a medium transmission extractor, and a deep global atmospheric light estimator. A quadruplet loss function is used to guide training in order to improve structural fidelity and lessen visual artifacts in the dehazed output.

LIDN demonstrates superior performance across a broad range of illumination conditions by effectively generating sharper, artifact-free images. Extensive evaluation on benchmark datasets such as RESIDE6K (3) confirms its robustness and improved accuracy over existing state-of-the-art daytime and nighttime dehazing techniques.

1.5.2 Lightweight Haze Removal for Real-Time Applications

While significant progress has been achieved in still-image dehazing, many existing methods are computationally intensive and not suitable for real-time video applications. This limitation hampers their deployment in time-critical systems such as autonomous navigation, video surveillance, and smart transportation.

To overcome this challenge, a novel lightweight and real-time video dehazing approach is introduced, which incorporates a new haze descriptor termed *SATVAL* (4). Derived from the ratio of the maximum saturation to the maximum value in an RGB frame, SATVAL enables efficient haze detection. Frames with a SATVAL value below a predefined threshold are identified as dehazed, allowing the system to bypass unnecessary processing. This selective strategy not only accelerates performance but also maintains competitive visual quality compared to more computationally expensive approaches.

Although this technique shows promising results in improving processing speed and reducing complexity, challenges remain in its generalization across diverse scenes and environments.

1.5.3 Hardware Implementation for Real-Time Processing

For practical deployment in real-world systems, the proposed lightweight haze removal algorithm is further implemented on embedded hardware platforms, such as the PYNQ-Z2 FPGA and NVIDIA Jetson series. These platforms are selected for their balance between computational efficiency and power consumption, making them suitable for edge applications in smart cities and autonomous systems.

Hardware acceleration enables real-time processing of video streams at acceptable frame rates while maintaining the quality of dehazed output. The integration of the SATVAL-based approach on these hardware platforms highlights the feasibility of deploying haze removal algorithms in constrained environments, reinforcing the method's applicability to safety-critical tasks such as intelligent transportation and aerial surveillance.

1.6 Thesis Overview

Each chapter of this thesis is dedicated to a comprehensive exploration of the challenges inherent in object tracking amidst adverse weather conditions, as well as an examination of the currently available datasets and recent standard methods pertaining to this task. Furthermore, proposed solutions are rigorously analyzed and discussed. Except for Chapter 1, which serves as the introduction, the subsequent chapters are organized as follows:

Chapter 2: The following chapter, titled "Literature Survey," provides an overview of previous research in both software and hardware implementations related to dehazing method. It explores various existing methodologies and highlights advancements in classical methods, deep learning method and many more other techniques.

Chapter 3: The following chapter, titled "Parameter Analysis," presents a comparative study of reference-based and no-reference parameters to evaluate the quality of image dehazing. It analyzes the effectiveness of these parameters in assessing image clarity and restoration accuracy. Additionally, the chapter introduces a user-friendly GUI designed to facilitate easy data retrieval and enhance accessibility for researchers and practitioners.

Chapter 4: The following chapter, titled "Parallel Processing of Atmospheric Light and Transmission Coefficient for Image Dehazing," proposes a parallel architecture to

enhance the efficiency of the dehazing process. It explores various contrast enhancement techniques and guided filter methods to improve image clarity while maintaining computational efficiency.

Chapter 5: The following chapter, titled "Night Time Image Dehazing," proposes a dehazing technique specifically designed for nighttime images. It utilizes the power law method with an automatic gamma calculation to enhance visibility and restore image clarity in low-light conditions.

Chapter 6: The following chapter, titled "Deep Learning Approach for Time-Invariant Image Dehazing," proposes a novel deep learning model based on CNN for efficient image dehazing. It introduces four distinct loss functions to enhance dehazing performance and improve image restoration quality. Additionally, it presents a meticulously designed deep learning-based haze removal network aimed at enhancing image clarity. To evaluate its effectiveness, the proposed network undergoes rigorous testing across various benchmarking databases, including the Daytime and Night-time Dehazing Benchmarking Database, Reside6K, I-Haze, O-Haze, Dense-Haze, and NH-Haze Database.

Chapter 7: The following chapter, titled "Hardware Implementation for Video Processing," presents the implementation of a parallel architecture on Raspberry Pi, PYNQ-Z2, and Jetson Nano boards. It provides a detailed comparison of these hardware platforms, analyzing their computational efficiency for real-time video processing applications.

Chapter 8: The following chapter, titled "ASIC Implementation of Image Dehazing Algorithm," presents the implementation of the dehazing algorithm in Verilog, followed by ASIC design optimization using Synopsys Design Compiler. Additionally, it provides a comparative analysis of FPGA and ASIC implementations, evaluating their performance and efficiency.

Chapter 9: The chapter, titled "Conclusion Future Directions," presents a summary of the contributions made by the proposed datasets and methods toward achieving an efficient implementation of the dehazing method in adverse weather conditions. Additionally, it highlights the limitations of the proposed approaches and discusses potential future research directions for further improvements.

Chapter 2

LITERATURE SURVEY

Researchers have developed different enhancement and restoration algorithms over the last three decades. Figure 2.1 [Source: Google Scholar] illustrates the number of research papers published per year that focus specifically on dehazing or are related to image dehazing implementations. The data spans from 1970 to March' 2025, showing a significant increase in publications over time, particularly after 2010. The count remained relatively low until the early 2000s, after which there was a notable rise, peaking between 2021 and 2024. The trend reflects growing research interest and advancements in dehazing techniques, with a sharp increase in publications from 2015 onward.

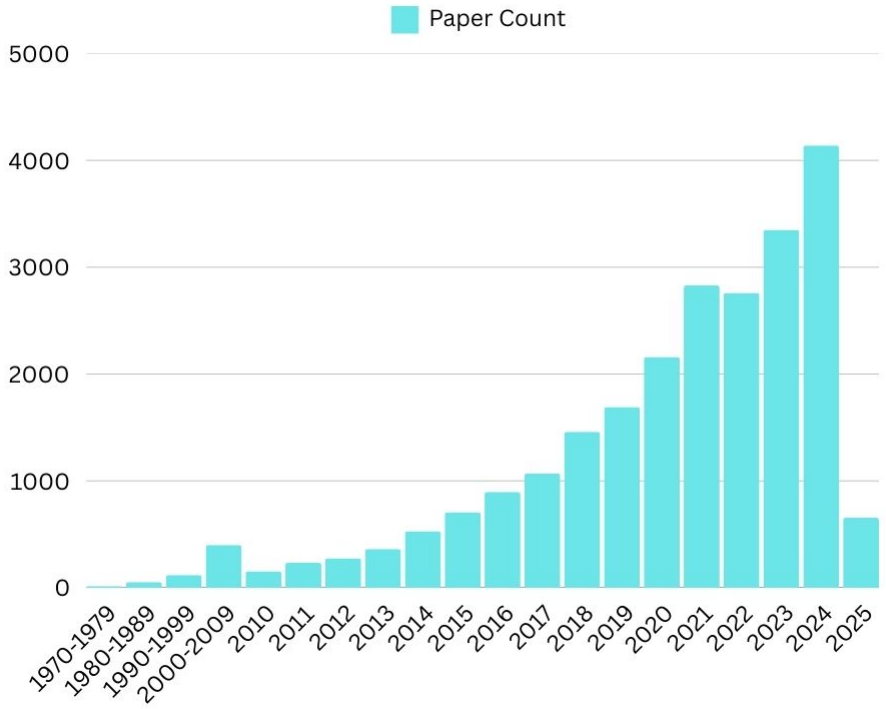

FIGURE 2.1: Quantity of Papers Published in Recent Years

Due to latency caused by both time and space complexity, the output of video sequence dehazing frequently experiences buffering. Therefore, computational efficiency must be the top priority for an algorithm to work well in real-time applications.

2.1 Image Dehazing Methods

Image dehazing is a vital preprocessing step in many computer vision and remote sensing applications, especially in outdoor environments affected by haze or fog. The presence of haze degrades image quality, reduces visibility, and affects scene understanding tasks.

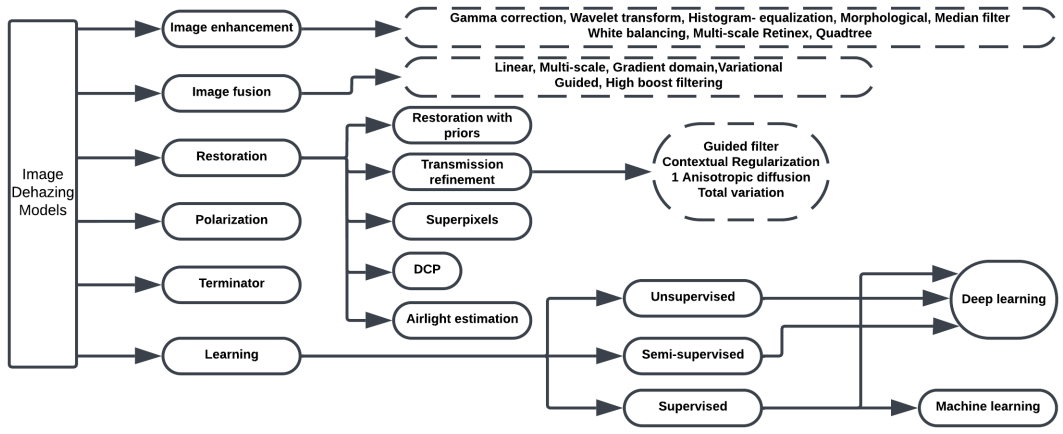

FIGURE 2.2: Different Image Dehazing Types

This chapter surveys prominent image dehazing techniques organized into six key categories: Image Enhancement, Image Fusion, Restoration, Polarization, Terminator-based approaches, and Learning-based methods. This classification provides a structured perspective for understanding the evolution and trends in the field.

2.2 Image Enhancement Techniques

Image enhancement methods focus on improving the visibility and contrast of hazy images without explicitly modeling the haze formation process. Classical techniques include histogram equalization, contrast stretching, and white balancing. More advanced approaches utilize Retinex theory to estimate the reflectance component, assuming illumination variations are responsible for degraded visibility.

In 1998, C. Tomasi et. al.(5) introduced Bilateral filtering, a technique for gray and color image dehazing that preserves edges while smoothing nearby pixel values.In contrast to traditional filters, which process each color channel independently, bilateral filtering leverages the perceptual metric embedded within the CIE-Lab color space. This enables bilateral filtering to harmoniously smooth colors and safeguard edges in accordance with human visual perception. Additionally, bilateral filtering outperforms standard filtering techniques by eradicating phantom colors along edges in color images and minimizing their manifestation in the original image.

A physics-based model is proposed by S.G. Narasimhan et. al. (6) to elucidate scene appearances under uniform adverse weather conditions. By leveraging changes in scene point intensities across different weather conditions, depth disparities within the scene

are facilitated for detection, and scene structure computation is enabled by their model. Subsequently, a rapid algorithm tailored for contrast restoration is presented. In contrast to previous approaches, their weather removal algorithm operates without necessitating prior knowledge of scene structure, scene reflectance distributions, or intricate understanding of specific weather conditions.

Oakley et. al. (7) introduced a technique to estimate the uniform level of airlight across an image, assuming its consistency throughout. This method hinges on minimizing a global cost function and is applicable to both monochrome and color images. It showcases resilience and remains unaffected by scaling discrepancies. Once the airlight estimate is obtained, image correction becomes a simple process. The algorithm's efficacy is scrutinized via Monte Carlo simulations using synthetic images across a range of statistical assumptions.

In this work, a simple and adaptive single image dehazing algorithm was proposed by Jin-Hwan Kim et. al. (8). The observation that a hazy image generally exhibits low contrast guides the effort to restore the original image by enhancing contrast. First, the airlight in a given hazy image is estimated based on quad-tree subdivision. Then, the transmission map is estimated by the proposed algorithm to maximize the contrast of the output image. A cost function is developed to measure contrast, comprising a standard deviation term and a histogram uniformness term.

Z. Li et al. (9) introduced an innovative approach for image defogging and enhancement that incorporates a replaceable plug-in segmentation module along with region-adaptive processing. Their method models medium transmission using color lines, which determine the ratio of ambient light to scene brightness. Additionally, color lines are used to characterize an object's surface reflection properties, specifically capturing the relationship between illumination chromaticity and diffusion chromaticity. This technique enhances image clarity while maintaining accurate color representation, improving overall visibility in foggy conditions.

Based on the Retinex theory, Yu et al. (10) proposed a method for nighttime single-image dehazing. In their approach, the transmission map is estimated through pixel-wise alpha blending, where transmissions derived from both dark channel priors and bright channel priors are combined into a single map, guided by a brightness-aware weight map. However, this method shares a common limitation with many other approaches

that rely on atmospheric scattering models, namely the challenge of accurately estimating transmission in highly complex or variable hazy conditions.

Although these methods are simple and fast, they may produce artifacts or over-enhanced regions, and they typically do not handle severe haze conditions effectively.

2.3 Image Fusion Approaches

Fusion-based methods combine multiple images of the same scene captured under different conditions or derived through preprocessing to enhance visibility. A notable method by Ancuti et al. proposes a multi-scale fusion of inputs generated from white-balanced and contrast-enhanced versions of the hazy image.

Ancuti et al. (11) introduced a fusion-based approach that utilizes two original hazy image inputs, incorporating white balance and contrast enhancement mechanisms. The method restores degraded images by adjusting their contrast and compensating for color shifts.

Y. Li et al. (12) developed a distinctive nighttime haze model that effectively considers the glow effects produced by multiple artificial light sources in low-light environments. This model enhances visibility in nighttime hazy images by incorporating the varying intensities and distributions of artificial lighting. While the approach performs well in dehazing nighttime scenes, it encounters challenges as haze density increases, leading to a rise in noise and artifacts that can degrade overall image quality.

A color image dehazing method using a near-infrared (NIR) image is proposed in this study by Dong-Wan Jang(13). The wavelength of light and the size of air particles both affect haze, a type of visual degradation brought on by light scattering. Near-infrared (NIR) images scatter less than red-green-blue (RGB) images, according to Rayleigh's law. This study finds that the high-frequency (HF) components of RGB and NIR images differ greatly in a hazy image, whereas they closely resemble each other in a small portion of a haze-free image. A unique dehazing technique that merges the HF components of RGB and NIR images inside a local hazy patch is presented in order to address this. Weight maps are then created using these fused HF components in order to combine detail layers. The proposed approach enhances the detail layer of a hazy RGB image by integrating the detail layers of RGB and NIR images, while the base layer is recovered using an existing single-image dehazing technique.

By using image fusion, Yakun Gao(14) offers a unique single-image dehazing technique that deviates from conventional picture restoration and enhancement techniques. The goal of dehazing is to get rid of haze effects between the camera and the scene. The first input image is obtained by subtracting the haze layer from the hazy image and adding depth information to improve color saturation. The second input image is then created by applying gamma correction and then detail enhancement on the grayscale image. The final restored image is produced by fusing the two input images using a local linear model.

Weight maps based on contrast, saturation, and visibility guide the fusion process. These methods are effective in improving perceptual quality and preserving naturalness, especially when multi-exposure or multi-polarization inputs are available.

2.4 Restoration-based Methods

An approach is derived by S. Shwartz et. al. (15) in this paper for blindly recovering the parameter required to separate the airlight from the measurements, consequently restoring contrast, without the need for user interaction or the presence of the sky in the frame. This simplifies the interaction and prerequisites necessary for image dehazing, which also entails compensation for attenuation. The success of this approach has been demonstrated in experiments, some of which are presented here.

A single-image dehazing technique designed for real-time applications including tracking, object detection, and surveillance was presented by J.P. Tarel and N. Hautière (16). To improve visibility and clarity in foggy conditions, their method combines methods such as tone mapping, picture restoration, and atmospheric veil inference.

Using a single input image, R. Fattal (17) presented a novel technique for calculating optical transmission in foggy settings. This estimation is used to eliminate dispersed light, improving scene visibility and restoring contrast free of haze. This method resolves ambiguities in the data by developing an improved image creation model that includes surface shading in addition to the transmission function. Making sure that the resulting shade and transmission functions continue to be locally statistically uncorrelated yields the answer. The color of the haze is also estimated using a similar technique.

Kaiming He. et. al.(18) proposesd a novel approach for removing haze from a single input image. The method relies on a prior called the "dark channel," which exploits the statistical properties of outdoor haze-free images. By analyzing the dark channel of a hazy image, which represents the minimum intensity in a local patch, the algorithm

estimates the scene's haze thickness and removes it effectively. The approach is robust and efficient, capable of restoring clear visibility and enhancing contrast in hazy scenes without requiring multiple images or complex scene assumptions. This paper introduced a simple yet powerful technique that has become a cornerstone in the field of single image haze removal, with widespread applications in computer vision, remote sensing, and image processing.

Because it is ill-posed by nature, haze removal from a single hazy image is a substantial issue. Q. Zhu et al.(19) provide a straightforward yet efficient color attenuation prior for dehazing in order to overcome this. A linear model with parameters learnt by supervised learning is developed under this innovative prior to represent the scene depth of the blurry image. This method makes it possible to recover depth information efficiently. Effective haze removal from a single image is made possible by the atmospheric scattering model, which restores scene radiance and allows for precise transmission determination using the predicted depth map.

In this paper, a new image and video dehazing method utilizing view-based cluster segmentation was proposed by Y. Feng et. al. (20) to avoid distortion in sky regions and ensure clarity in the sky and white objects. To estimate the sky region, the depth map is first grouped using the Gaussian Mixture Model (GMM) based on distant views. The transmission estimation is then refined to reduce distortion. Then, GMM improves atmospheric light estimate for increased global contrast by segmenting a single hazy image into classifications using the Color Attenuation Prior. Finally, for efficient video dehazing, an online GMM clustering technique is used.

An efficient scene-adaptive single image dehazing approach via opening dark channel model (ODCM) is presented by Xin Liu et. al.(21) to address issues such as color distortion and halo artifacts often encountered in traditional dark channel prior based haze removal schemes in remote scenes. First, the image depth information is detected and separated into close view and distant view. Then, an ODCM is proposed to optimize the entire atmospheric veil, with the values of close view being regularized by a minimum channel image while the distant parts are estimated by an appropriate lower constant. Subsequently, the transmission map can be further optimized by a guided filter and smoothed by a domain transform filter. Finally, the haze-degraded image can be well restored by the atmosphere scattering model.

D. Berman et al. (22) observed that pixels belonging to a specific cluster are often non-local, meaning they are distributed across the entire image rather than being confined

to a specific region. They proposed that the colors in a haze-free image could be effectively represented by a limited set of a few hundred unique colors, which naturally form compact clusters in RGB space. This observation led to the development of the hazy image priors used in their dehazing approach, where the transmission map is estimated by leveraging the assumption that the color clusters in a clear image remain distinguishable, even under the influence of haze. Their method significantly improves haze removal by efficiently estimating scene transmission while preserving color consistency.

M. Ju et al. (23) introduced the Enhanced Atmospheric Scattering Model (EASM), a novel parameter designed to mitigate the dim effect and improve the modeling of outdoor hazy scenes. They proposed a grey-world assumption-based technique called Image Dehazing and Exposure (IDE), which effectively enhances the visibility of hazy images. However, their method faces challenges in accurately estimating transmission, leading to incomplete haze removal and unwanted color variations in the processed images.

The implementation of dark-channel-prior (DCP)-based dehazing, specifically for outdoor video applications, is examined by Yongmin Park et al.(24). A number of optimization strategies are presented in order to speed up execution. The computational cost of airlight estimation is greatly reduced by employing distributed sorting with scaled luminance and selectively applying it by taking use of the coherence between subsequent frames in a video stream. Additionally, an assumption about the chrominance of airlight in outdoor settings is included to reduce the complexity of transmission calculation. A prototype implementation is used to evaluate the dehazing quality and execution time of the suggested DCP-based dehazing technique.

S. Roy. Et. al. (25) proposed a method where an attempt has been made to remove artifacts in the depth map of the hazy image using a Weighted Least Mean Square-based edge-preserved smoothing technique, which in turn results in the estimation of an artifact-free transmission map. The original bright, clear, and natural image radiance is restored using refined transmission estimation and an image recovery optical model, showcasing effectiveness compared to state-of-the-art techniques. Extensive experiments (both qualitative and quantitative) validate that the proposed technique is computationally less expensive, simple, and efficient.

These methods require accurate estimation of physical parameters and may suffer in heterogeneous haze conditions or in the presence of bright objects.

2.5 Polarization-based Methods

Polarization-based techniques utilize the fact that scattered light from atmospheric particles is partially polarized. By capturing multiple images using different polarizer orientations, it is possible to estimate the airlight and recover the true scene radiance.

In 2001, Schechner et al. (26) introduced a method for effectively eliminating haze from images by exploiting the partial polarization of airlight scattered by atmospheric particles. While polarization filtering alone is often found insufficient for haze removal, their approach is noted for its versatility and ability to function across diverse atmospheric and viewing conditions. By scrutinizing the image formation process and considering polarization effects in atmospheric scattering, a technique is devised to reverse this process and restore clarity to hazy images. As few as two images captured through a polarizer at varying orientations are required by their method, offering instant results regardless of weather changes. Experimental findings demonstrating significant contrast enhancement and color correction are presented, even in challenging conditions unsuitable for traditional polarization filtering. Additionally, a depth map of the scene is produced by their method, furnishing insights into atmospheric particle properties as an ancillary benefit. Though physically grounded and effective, these methods require special hardware and precise image alignment, limiting their use in real-time or consumer applications.

2.6 Terminator Line-based Approaches

These methods exploit scene geometry, such as the horizon line (often referred to as the terminator), vanishing points, or object boundaries, to assist in haze removal. Depth estimation is often guided by the assumption that sky regions are infinitely far and thus fully hazed.

An effective approach to geometry-guided dehazing is presented by Eigen et al. in their work on depth prediction from a single image using a multi-scale deep network (27). Although not a direct dehazing method, their model leverages scene layout and geometric priors—such as vanishing points and horizon cues—to estimate depth maps. These predicted depth maps have since become foundational components in subsequent dehazing methods that utilize depth-aware transmission estimation. Their framework assumes the sky to be at infinite depth, aligning well with the terminator-type dehazing

assumption, and it is particularly suitable for scenes containing prominent geometric structures such as roads, buildings, and the skyline.

In another significant contribution, Zhang et al. propose a variational approach to haze-aware visibility enhancement by integrating geometric structure analysis into the dehazing process (28). Their model accounts for vanishing lines and object boundaries, using them to guide the visibility estimation and regularization within a variational framework. This method improves transmission map accuracy, particularly in complex outdoor environments, by exploiting strong scene priors that rely on the layout and organization of urban structures. The use of vanishing points and sky-based infinite depth assumptions enhances robustness in natural scenes with known geometry.

Ju et al. further extend this line of research by explicitly incorporating horizon-based priors into a depth-aware single-image dehazing framework (29). Their method segments the sky region—assumed to be infinitely distant—and uses the detected horizon line as a key cue for guiding the transmission estimation. This geometry-aware approach allows for better handling of depth discontinuities near the skyline and object boundaries, which are common pitfalls in traditional methods. The model is especially effective in road and landscape imagery, where the geometric cues are prominent and reliable.

2.7 Learning-based Methods

Recent advancements leverage deep learning to learn haze removal directly from data. Supervised models like DehazeNet, AOD-Net, and GridDehazeNet are trained on synthetic datasets to regress clean images or transmission maps.

A trainable end-to-end system called DehazeNet is proposed by Bolun Cai et. al. (30) for medium transmission estimation. DehazeNet takes a hazy image as input and outputs its medium transmission map, which is subsequently used to recover a haze-free image via the atmospheric scattering model. DehazeNet adopts a convolutional neural network-based deep architecture, with layers specially designed to embody the established assumptions/priors in image dehazing. Specifically, Maxout units are used for feature extraction in the layers, capable of generating almost all haze-relevant features. Additionally, a novel nonlinear activation function called bilateral rectified linear unit is proposed in DehazeNet, which is able to enhance the quality of the recovered haze-free image. Connections between the components of the proposed DehazeNet and those used in existing methods are established.

Ju Mingye et al.(31) presented IDBP, a robust picture dehazing method based on the atmospheric scattering model (ASM) that successfully overcomes the drawbacks of single-prior methods. The two main components of IDBP are multiple prior constraint (MPC) and atmospheric light estimation (ALE). In order to improve image brightness while reducing information loss, the ALE module uses a revolutionary global brightening technique. In the meantime, the MPC module overcomes the limitations of single-prior approaches by combining non-local, local, and global priors to improve the haze removal procedure. In contrast to other methods, IDBP uses multiple priors and the principle of minimal information loss to enforce the ASM without the need for training, guaranteeing greater robustness and ease of implementation.

B. Ganguly (32) uses two different models to propose an effective single-image dehazing technique. The first model is a new framework for atmospheric scattering that calculates the transmission map and atmospheric light. A haze map is produced by the second model, which is known as the sparse haze model. The haze map is subjected to a least-square optimization in order to recover a haze-free image. In order to measure the amount of haze removed from input photos with different haze levels, the haze removal procedure is also examined using a membership function. Three different dataset types are used to evaluate the dehazing performance: synthetic photos with varying haze intensities, real-world hazy photographs, and a customized dataset with heavy haze.

Unsupervised models such as CycleDehaze utilize cycle-consistency and perceptual losses to remove haze without paired data. Transformer-based and GAN-based architectures further improve the perceptual quality of results. However, generalization to real-world haze and dependency on training data remain key challenges.

2.8 Comparative Analysis

The table 2.1 titled "Comparison of Dehazing Techniques" provides a detailed analysis of various methods based on key parameters, such as whether they are model-based, data requirements, processing speed, hardware dependencies, and generalization capabilities. Enhancement methods are non-model-based, require no additional data, operate at high speed without hardware reliance, and exhibit low generalization. Fusion techniques use multi-view data, have medium speed, optional hardware needs, and medium generalization. Restoration is model-based, independent of data, with medium speed and generalization, requiring no specific hardware. Polarization relies on polarized images, special cameras, operates at low speed, but achieves high generalization. Terminator approaches

depend on scene geometry, operate at medium speed, and generalize moderately with optional hardware. Finally, learning-based methods vary between model-based and non-model-based, utilize large datasets, have variable speed, rely on GPU/TPU hardware, and exhibit high or low generalization depending on their implementation.

TABLE 2.1: Comparison of Dehazing Techniques

Method	**Model-based**	**Data Required**	**Speed**	**Hardware**	**Generalization**
Enhancement	No	None	High	None	Low
Fusion	No	Multi-view	Medium	Optional	Medium
Restoration	Yes	None	Medium	None	Medium
Polarization	Yes	Polarized Images	Low	Special Camera	High
Terminator	Yes	Scene Geometry	Medium	Optional	Medium
Learning	No/Yes	Large Dataset	Variable	GPU/TPU	High/Low

2.9 Research Gaps

The evolution and innovation in image dehazing techniques are highlighted by these diverse approaches, with each addressing specific challenges and pushing the boundaries of visibility enhancement in degraded images. Continued research in this area is promising further advancements, ultimately benefiting applications such as surveillance, autonomous driving, and medical imaging. This survey categorizes existing dehazing methods based on their underlying principles and practical constraints. While enhancement and fusion techniques are computationally simple, they may fail in dense haze. Restoration-based methods offer physical interpretability but are sensitive to parameter estimation. Learning-based methods have achieved state-of-the-art results but face issues of generalization and dataset bias.

2.10 Previous Work for Hardware Implementation

In 2013, (33) reported a quick and effective haze reduction technique in this letter. The ambient light is extracted using an extremum approximation method, and transmission

is obtained by alternating between mean and edge-preserving filters using a contour-preserving estimator. This method effectively keeps the reconstructed image free of the halo artifact. An 11-stage pipelined hardware architecture for the haze removal approach is presented in order to satisfy the requirements of real-time applications. The design uses TSMC 0.13-m technology to achieve a frequency of 200 MHz with a gate count of 12.8 K. When compared to earlier algorithms, simulation results show that same results are achieved with less execution time, which qualifies the design for low-cost, high-performance hardware implementation for haze removal.

A real-time haze reduction technique based on the dark channel prior was presented by Bin (34) in 2017. An approximation technique for predicting atmospheric light and transmission is used to improve haze removal efficacy. A hardware design that can remove haze in real time is suggested for embedded system applications. Using a Stratix FPGA, this system reaches a frequency of 116 MHz. According to simulation results, the hardware architecture is very effective and efficient, satisfying real-time requirements and producing good image recovery outcomes—even for huge images.

A method and architecture design for a hardware-efficient image dehazing engine were presented in this paper by (35) Low-complexity airlight estimate (LAE) and independent transmission rate estimation (ITRE) are the two primary methods used in the dehazing algorithm. Without the need for laborious sorting procedures or computationally demanding filtering, LAE is made to effectively anticipate the airlight. To enable effective data scheduling, a preluded airlight estimation is also incorporated into the hardware architecture. ITRE's ability to forecast transmission rates independently of airlight allows it to process LAE and ITRE simultaneously, increasing the hardware architectures' throughput. This study performs competitively when compared to other cutting-edge techniques in terms of peak signal-to-noise ratio, structural similarity, contrast distortion, and computational efficiency. Taiwan Semiconductor Manufacturing Company's CMOS 0.18-m technology, with a logic gate count of 32.6 K, was used to build the hardware design. The architecture supports 4096×2160 resolution at 60 frames per second and runs at a frequency of 200 MHz with a power consumption of 16.5 mW. Its maximum throughput is 600 megapixels per second. According to experimental data, this study exhibits excellent energy and area efficiency.

A data-driven image dehazing technique based on a convolutional neural network (CNN) and dark channel prior (DCP) was proposed by (36) in 2021 as a solution to this problem of real-time video dehazing and to meet strict requirements. This approach automatically learns crucial features and yields better results. The hardware implementation of the suggested approach is also shown, and it has been designed to be hardware-friendly. By storing activations in a few line buffers, the system does not require off-chip memory

like dynamic random-access memory (DRAM). Implementations of application-specific integrated circuits (ASIC) and field programmable gate arrays (FPGA) have demonstrated that the design is ideal for use in scenarios requiring stringent power budgets, little memory, and limited computing capabilities. Quantitative analysis demonstrates more than an 11% average PSNR improvement in image quality on standard datasets compared to state-of-the-art hardware methods while consuming comparable hardware resources and power.

A 4K-capable hardware implementation of an effective haze removal method was proposed by (37) in 2022. It has two notable enhancements. First, a linear model with four haze-relevant properties is used to predict the depth-dependent haze distribution. Maximum likelihood estimates are used to establish the model parameters. Second, the approximated quad-decomposition approach is used to estimate the ambient light. The effectiveness of the suggested approach is confirmed by extensive experimental findings compared to established benchmark techniques. A pipelined architecture made up of specially designed macros, including split multipliers, parallel dividers, and serial divisions, is also introduced to facilitate real-time processing. This hardware architecture can handle DCI 4K videos at a rate of 30.8 frames per second, according to the implementation results.

A straightforward and effective saturation-based transmission map estimate technique was presented by (38) in 2023 for real-time single-image dehazing. Furthermore, the suggested image dehazing technique includes a very large scale integration (VLSI) architecture that is hardware-efficient. In order to estimate the saturation-based transmission map, the algorithm reduces halo artifacts using an edge-preserving filter, improves the robustness of atmospheric light estimation through a hardware-friendly local atmospheric light estimation module based on pixel saturation values, and does away with computationally demanding sorting operations to calculate the dark channel. This technology performs competitively in terms of dehazed image quality when compared to earlier sophisticated dehazing techniques. The suggested architecture and the best dehazing architecture currently in use are both synthesized using the Cadence Genus compiler, functionally validated using the Vivado 2019.1 simulator, and defined in Verilog hardware description language (HDL). Results from implementation demonstrate that the recommended architecture achieves improved throughput and is hardware-efficient. The suggested dehazing architecture is appropriate for applications with hardware limitations since it performs better in terms of space and delay than current techniques.

Chapter 3

Parameter Analysis

3.1 Introduction

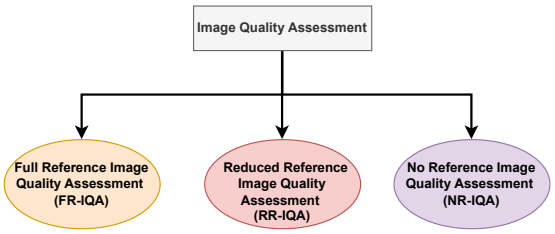

FIGURE 3.1: Image Parameter Calculation Based on Feature Extraction

In computer vision, high-quality images are essential across many applications to ensure accurate analysis and interpretation. However, image quality can often degrade due to environmental factors like haze, fog, or limitations in imaging technology, leading to the loss of critical information. Image quality refers to the visual characteristics that influence human perception, typically assessed through both quantitative measures and qualitative, perception-based techniques.

Image Quality Assessment (IQA) methods can be categorized into three main types . The first type, Full-Reference Image Quality Assessment (FR-IQA)(39) (40) (41) (42) (43) (44) (45) (46) (47) (48) (49) (50) (51), evaluates an image's quality by comparing it with an ideal reference image. FR-IQA methods are widely used because they provide objective, quantitative measurements by treating the reference image as a benchmark . When only partial reference data is available, Reduced-Reference Image Quality Assessment (RR-IQA)(52)(53)is used. RR-IQA methods extract and compare specific features or statistical characteristics (such as edges or textures) from the original and distorted images. This approach is particularly useful in bandwidth-limited situations, like real-time streaming, where the entire reference image cannot be transmitted. For example, in video streaming over a constrained network, certain features can be extracted from the original frames and transmitted; these are then compared to the received frames to gauge quality, making RR-IQA efficient for applications with limited storage or transmission capabilities.

The third type, No-Reference Image Quality Assessment (NR-IQA)(54) (55) (56) (57) (58) (59) (60) (61), evaluates image quality without any reference image. NR-IQA is essential for applications where reference images are unavailable, such as real-time video streaming, surveillance, and user-generated content. NR-IQA methods rely on assessing the quality of a single image based on various perceptual attributes, making it suitable for uncontrolled, dynamic environments.

[0] **A. Ghosh**, A. Ali and S. Sinha Chaudhuri, "A Review of Image Quality Assessment Metrics for Haze Removal: Bridging Objective and Human Perception". Journal of Real-Time Image Processing. Submitted,Impact Fac- tor- 3.0

This chapter systematically reviews ten key IQA metrics—MSE, PSNR, SSIM, MSSIM, Correlation, MDSI, LPIPS, GMSD, BRISQUE, and NIQE—for their effectiveness in measuring haze removal performance. Main contributions are as follows:

1. A systematic review of ten prominent IQA metrics for their ability to assess haze removal effectiveness.
2. A newly proposed Human-Level Perception for Haze Quality Assessment (HLHQA) dataset, consisting of 36 hazy and haze-free images rated on a 0–10 scale, serving as a perceptual benchmark.
3. Analysis of each metric's alignment with Human-Level Perception (HLP) under four haze conditions: no haze, low haze, dense haze, and night haze.
4. Development of a graphical user interface (GUI) for efficient and accessible comparison of haze removal models.

3.2 Related Work

Image quality assessment is a critical evaluation metric for determining the effectiveness of generated data. A common approach involves comparing the "true" pixel values of the original image with the degraded image using the mean squared error (MSE). MSE represents the average of the squared differences between the original and degraded images. A lower MSE indicates a better reconstruction, while a higher Peak Signal-to-Noise Ratio (PSNR) suggests a more accurate restoration of the original image, as it measures the ratio of maximum signal power to noise.

(39) introduced the Structural Similarity Index (SSIM) for comparing image quality with respect to the original image or ground truth. Later, in the same year, Zhou Wang et al.(42) proposed the Multi-Scale Structural Similarity Index (MSSSIM), which enhances image quality evaluation by analyzing structural similarity across multiple scales and resolutions.

(40) introduced the Learned Perceptual Image Patch Similarity (LPIPS) metric in 2018, improving perceptual similarity assessment through learned feature representations. In 2016, (41) proposed the Mean Deviation Similarity Index (MDSI), which considers luminance and contrast variations to measure perceptual quality. Similarly, the Gradient Magnitude Similarity Deviation (GMSD) was introduced in 2014 by (43), emphasizing gradient magnitude similarity for image quality assessment.

For no-reference image quality assessment, (54) developed the Blind/Referenceless Image Spatial Quality Evaluator (BRISQUE) in 2012, utilizing natural scene statistics for quality evaluation. In the same year, (55) introduced the Natural Image Quality Evaluator (NIQE), a no-reference metric comparing statistical features of an image with a natural scene model.

(62) proposed the Feature Similarity Index (FSIM), which evaluates image quality by analyzing low-level features such as phase congruency and gradient magnitude, essential for human visual perception. Additionally, in 2014, (63) introduced the Visual Saliency-based Index (VSI), which incorporates visual saliency information to assess image quality, reflecting the importance of visually significant regions in human perception.

3.3 Types of IQA Metrics and Mathematical Formulations

There are various parameters available for comparing images, but I have selected 10 key metrics to evaluate image quality and background. Among them is SSIM , a perceptual metric used to assess image quality in comparison to a reference image. SSIM is a full-reference metric, meaning it requires two input images and evaluates one image's quality relative to another.

3.3.1 SSIM

SSIM proposed by (39) focuses on structural information, emphasizing the relationship between neighboring pixels, which provides important insights into the visual scene's composition. Unlike metrics such as MSE or PSNR, which measure absolute errors, SSIM considers perceptual phenomena like contrast and luminance masking. Contrast masking refers to how distortions become less noticeable in areas of high activity or texture, while luminance masking means that distortions are harder to detect in brighter parts of an image.

Developed by Hamid Sheikh and Eero Simoncelli, SSIM was first introduced in 2004 in the IEEE Transactions on Image Processing. The paper laid the foundation for perceptual quality assessment by linking SSIM to human visual neuroscience and validating it with human evaluations.

$$\text{SSIM}(x, y) = \frac{(2\mu_x\mu_y + C_1)(2\sigma_{xy} + C_2)}{(\mu_x^2 + \mu_y^2 + C_1)(\sigma_x^2 + \sigma_y^2 + C_2)}$$

TABLE 3.1: Quality Assessment Metrics

Metric	Class	Description	Better	Range
MSE	FR	Measures the average squared difference between reference and distorted images.	lower	$[0, \infty)$
PSNR	FR	Ratio of the distortion's power to the highest pixel intensity.	higher	$[0, \infty)$
SSIM(39)	FR	Local similarity of luminance, contrast, and structure between two images.	higher	$(0, 1]$
MS-SSIM(42)	FR	Based on SSIM, it integrates structure and contrast at various scales with brightness at the maximum resolution.	higher	$(0, 1]$
Correlation	FR	Measures the linear correlation between reference and distorted images.	higher	$[0, 1]$
MDSI(41)	FR	Multiscale difference between structure and intensity of reference and distorted images.	lower	$[0, \infty)$
LPIPS(40)	FR	L2 distance between neural network activations of reference and distorted images.	lower	$[0, \infty)$
GMSD(43)	FR	Measures gradient magnitude similarity.	lower	$[0, \infty)$
BRISQUE(55)	NR	Trains an SVM to learn a mapping from natural image statistics to quality score.	lower	$[0, \infty)$
NIQE(54)	NR	Mahalanobis distance between natural and distorted image feature distributions.	lower	$[0, \infty)$

The SSIM formula compares two input images, x and y. Here, μ_x represents the mean of image x, and μ_y represents the mean of image y. The variance of x is denoted as σ_x^2, while σ_y^2 refers to the variance of y. The covariance between x and y is σ_{xy}. Constants $C_1 = (k_1 L)^2$ and $C_2 = (k_2 L)^2$ are introduced, where L is the dynamic range of pixel values, and typical values for k_1 and k_2 are 0.01 and 0.03, respectively.

Pros:

- Closely models human visual perception, focusing on structural information, luminance, and contrast.
- Widely regarded as a good general-purpose metric for image quality assessment.
- Effective for structural distortions and has good sensitivity to haze removal.

Cons:

- Sensitive to small shifts or alignment issues, potentially limiting use in real-world scenarios.
- May produce inconsistent results in extremely low-quality or dense haze images.

3.3.2 MSE

The Mean Squared Error (MSE) is one of the most widely used estimators for evaluating image quality. It measures the average squared difference between the estimated values and the actual values. A value closer to 0 indicates better performance, as smaller errors mean higher accuracy. MSE is a full-reference metric, requiring both the original and distorted images for comparison.

MSE accounts for both the estimator's bias and variance. For an unbiased estimator, MSE equals the estimator's variance. The variance is measured in the same units as the square of the quantity being estimated, making MSE a useful indicator of the overall error. The Root-Mean-Square Deviation (RMSD), or standard deviation of the variance, can also be derived from MSE to offer more insights.

In other terms, MSE is also known as the Mean Squared Deviation (MSD), which measures the average of the squares of errors, where an error is the difference between the estimator and what is estimated. In image processing, it serves as a function of risk, calculating the expected value of the quadratic or squared error loss.

The formula for MSE is:

$$\text{MSE} = \frac{1}{mn} \sum_{i=1}^{m} \sum_{j=1}^{n} [I(i,j) - K(i,j)]^2$$

Where:$I(i,j)$ represents the pixel intensity of the original image, $K(i,j)$ denotes the pixel intensity of the distorted image, and m and n correspond to the dimensions of the image.

Pros:

- Simple and computationally efficient, making it suitable for large-scale comparisons.
- Provides a direct measure of pixel-wise error.

Cons:

- Low perceptual relevance: does not account for human visual perception.
- Sensitive to minor pixel variations, making it less effective for dehazing tasks where overall structure is important.
- Lacks robustness against image transformations or structural inconsistencies.

3.3.3 PSNR

Peak Signal-to-Noise Ratio (PSNR) quantifies the ratio of the maximum possible signal power to the power of the noise that corrupts the quality of the signal, typically caused by distortion or compression. It is expressed in decibels (dB) to account for the high dynamic range of signals. The PSNR is used to evaluate the quality of image or video reconstruction, especially in lossy compression codecs. The higher the PSNR value, the better the reconstruction quality.

The original uncompressed image is considered the "signal," while any deviations introduced by compression or noise are the "noise." PSNR provides an approximation of human perception regarding reconstruction quality, although higher PSNR values generally indicate better image quality.

For an 8-bit image, the PSNR value typically ranges from 30 to 50 dB, while for a 16-bit image, it ranges from 60 to 80 dB. For applications like wireless transmission, a PSNR of 20–25 dB is considered acceptable.

The formula for PSNR is:

$$\text{PSNR} = 10 \cdot \log_{10} \left(\frac{L^2}{\text{MSE}} \right)$$

Where:

- L is the dynamic range of the pixel values (e.g., 255 for 8-bit images),
- MSE is the Mean Squared Error between the original and distorted images.

PSNR is widely used for comparing the quality of compressed images or videos, and a higher PSNR indicates less distortion and better quality.

Pros:

- Widely used in image processing for its simplicity.

- Easy to interpret: higher PSNR usually indicates better reconstruction quality.
- Effective for comparing images with relatively minor variations.

Cons:

- Limited sensitivity to perceptual quality, especially for structural differences and visual artifacts.
- Ignores human visual perception; high PSNR may not equate to perceived quality.
- More suitable for simple additive noise, less effective in complex haze conditions.

3.3.4 Correlation

Correlation is a key operation in image processing that helps extract meaningful information from visual data. It is often simpler than convolution and serves as a fundamental tool for analyzing and interpreting images. This document provides an overview of correlation, including both theoretical and practical aspects.

The correlation operation measures the similarity between an image and a filter (or kernel) by sliding the filter over the image and computing the dot product at each position. It is commonly used to identify patterns or features within the image.

The correlation between an image I and a filter K is given by:

$$(I \star K)(x, y) = \sum_i \sum_j I(x + i, y + j) \cdot K(i, j)$$

Where (x, y) denotes the position of the filter center, $I(x + i, y + j)$ represents the pixel value at position $(x + i, y + j)$ in the image, and $K(i, j)$ corresponds to the value of the filter at position (i, j).

In practice, correlation is used in various applications, such as image matching, template detection, and feature extraction. By comparing the image to different filters, correlation helps identify specific patterns and features, providing valuable insights from visual data.

Pros:

- Measures similarity in structure between images, focusing on structural alignment rather than pixel differences.

- Effective for assessing general patterns and structural similarity.

Cons:

- Insensitive to fine details and noise.
- Cannot capture perceptual quality effectively on its own; often used alongside other metrics.

3.3.5 Multi-scale structural similarity index (MS-SSIM)

The Multi-Scale Structural Similarity (MSSIM)(42) index extends the Structural Similarity Index (SSIM) by incorporating luminance, contrast, and structure information at multiple scales. This method enhances flexibility compared to single-scale approaches by accommodating variations in viewing conditions and image resolutions.

The MSSIM is computed by combining SSIM values obtained at various resolutions or scales. This allows the method to evaluate the quality of an image in a more comprehensive manner, considering both fine and coarse details.

The MSSIM index is defined as:

$$\text{MSSIM}(x, y) = \prod_{i=1}^{N} \text{SSIM}_i(x, y)$$

where N represents the number of scales, and $\text{SSIM}_i(x, y)$ is the SSIM computed at scale i.

In this approach, I use image synthesis techniques to calibrate the parameters that determine the relative importance of each scale. This calibration improves the method's ability to handle different viewing conditions and variations in image quality.

Experimental results demonstrate that the proposed MSSIM-based method offers superior performance compared to traditional single-scale SSIM approaches, highlighting its effectiveness in various image quality assessment scenarios.

Pros:

- Extends SSIM to multiple scales, enhancing its sensitivity to multi-scale artifacts in dehazing.

- Captures perceptual quality more comprehensively across different image resolutions.

Cons:

- Computationally more intensive than SSIM.
- Performance is affected by resizing and scale adjustments, making comparisons challenging.

3.3.6 MDSI

The Multiscale Difference between Structure and Intensity (MDSI)(41) is a perceptual image quality assessment (IQA) metric designed to evaluate image quality in various processing applications, including acquisition, compression, restoration, and multimedia communication. This paper introduces a robust full-reference IQA model that leverages deviation pooling (DP), chromaticity similarity (CS), and gradient similarity (GS).

A novel GS approach is proposed, utilizing a fusion technique to more accurately reflect the human visual system (HVS), addressing limitations of existing GS methods. For measuring color changes, an efficient formula is provided to compute the joint similarity map of two chromatic channels:

$$\mathrm{CS}(x,y) = \frac{\sum_{i,j}(C_x(i,j)\cdot C_y(i,j))}{\sqrt{\sum_{i,j} C_x^2(i,j)\cdot \sum_{i,j} C_y^2(i,j)}}$$

where $C_x(i,j)$ and $C_y(i,j)$ are the chromaticity values of the two channels at pixel location (i,j).

The proposed CS map demonstrates greater efficiency and yields predictions comparable to or better than conventional methods. DP is formulated to integrate the GS and CS maps, drawing inspiration from recent advancements in standard deviation pooling:

$$\mathrm{DP} = \left(\sum_{i,j}(GS(i,j) - CS(i,j))^p\right)^{1/p}$$

where p represents the Minkowski power used in pooling, and an additional power pooling technique is also explored.

The proposed MDSI index, characterized by minimal complexity and high reliability, outperforms state-of-the-art IQA metrics in quality predictions when tested on six datasets of natural images, a synthetic dataset, and a digitally altered dataset.

Pros:

- Effective in capturing perceptual differences, including contrast and structure.
- Generally robust for measuring quality across images with variations in haze density.

Cons:

- Less widely used and standardized, so interpretability can be challenging.
- Can be more sensitive to noise in low-quality images.

3.3.7 LPIPS

The Learned Perceptual Image Patch Similarity (LPIPS)(40) metric addresses the limitations of traditional image quality measures like PSNR and SSIM, which often overlook complex aspects of human perception. While humans can easily judge visual similarity between images, the underlying perceptual processes are intricate and not fully captured by basic metrics.

Recent research has shown that features from deep networks, such as VGG models trained on ImageNet, are highly effective for evaluating image synthesis quality. To advance this field, a new dataset of human perceptual similarity judgments has been introduced. This dataset enables a comparison of deep features using conventional metrics, systematically evaluated across various tasks and systems.

The LPIPS metric quantifies perceptual similarity by comparing deep network features rather than pixel-level differences. The formula for LPIPS is:

$$\text{LPIPS}(I, K) = \frac{1}{L} \sum_{l=1}^{L} \|\phi_l(I) - \phi_l(K)\|^2$$

where ϕ_l represents the activation of the l-th layer in a deep neural network for images I and K, and L is the total number of layers considered. This approach shows that deep features, which capture more complex visual information, provide a significantly better

measure of perceptual similarity compared to traditional methods. This finding holds across various deep architectures and levels of supervision, suggesting that perceptual similarity is best modeled through deep visual features.

Pros:

- Uses deep learning to model human perceptual similarity, making it highly sensitive to perceptual details.
- Performs well in real-world applications, particularly with dehazing, where visual details are essential.

Cons:

- Computationally intensive due to deep neural network components.
- May be less interpretable than traditional metrics for some audiences.

3.3.8 GMSD

Accurately evaluating the perceptual quality of images is crucial in applications such as image compression, restoration, and multimedia streaming. For an image quality assessment (IQA) model, high prediction accuracy and computational efficiency are essential, especially with the increasing volume of visual data transmitted through high-speed networks.

A new IQA model, known as Gradient Magnitude Similarity Deviation (GMSD)(43), is introduced to address these needs effectively. The sensitivity of image gradients to distortions is leveraged in GMSD, with recognition given to the fact that different local structures degrade in varying ways. The global variation of a gradient-based local quality map is evaluated by this approach to predict overall image quality.

The GMSD metric is based on the following components:

- Gradient Magnitude Similarity (GMS):

  The pixel-wise Gradient Magnitude Similarity between the reference image I and the distorted image K is defined as:

$$GMS(i,j) = \frac{2\left|\nabla I(i,j)\right|\left|\nabla K(i,j)\right| + C_1}{\left|\nabla I(i,j)\right|^2 + \left|\nabla K(i,j)\right|^2 + C_1}$$

where $\nabla I(i,j)$ and $\nabla K(i,j)$ are the gradient magnitudes at pixel (i,j) for the reference and distorted images, respectively, and C_1 is a constant to avoid division by zero.

- Gradient Magnitude Similarity Map (GMSM):

  The Gradient Magnitude Similarity Map is the local quality map derived from GMS values:

  $$\text{GMSM}(i,j) = \text{GMS}(i,j)$$

- Gradient Magnitude Similarity Deviation (GMSD):

  The overall image quality is assessed by combining the standard deviation of the GMSM map:

  $$\text{GMSD}(I,K) = \sqrt{\frac{1}{mn}\sum_{i=1}^{m}\sum_{j=1}^{n}\left(\text{GMSM}(i,j) - \bar{\text{GMSM}}\right)^2}$$

  where $\bar{\text{GMSM}}$ is the mean of the GMSM values, and m and n are the dimensions of the image.

  The GMSD model is significantly faster than most state-of-the-art IQA methods and provides highly competitive accuracy in predicting perceptual image quality.

Pros:

- Effective in detecting gradient changes and edge artifacts, which are crucial in haze-affected areas.
- Provides good sensitivity to both structural and gradient distortions.

Cons:

- Can be overly sensitive to high-frequency noise.
- Not as widely validated in dehazing applications, leading to less standardization.

3.3.9 BRISQUE

The Blind/Referenceless Image Spatial Quality Evaluator (BRISQUE)(55) is a natural scene statistic-based, distortion-generic, blind/no-reference (NR) image quality assessment (IQA) model that operates in the spatial domain. Unlike distortion-specific models that target particular artifacts like ringing, blur, or blocking, BRISQUE utilizes scene

statistics of locally normalized luminance coefficients to quantify potential losses of "naturalness" due to distortions. This approach results in a holistic quality measure.

BRISQUE models Gaussian distributions of mean subtracted contrast normalized (MSCN) features and obtains 36-dimensional Gaussian parameters. It then trains a Support Vector Machine (SVM) to map these features to a quality score.

The feature extraction process is based on the empirical distribution of locally normalized luminances and their products. This is done without requiring transformation to other coordinate frames, such as Discrete Cosine Transform (DCT)(64) or wavelets, differentiating it from other NR IQA approaches.

3.3.9.1 Equation for MSCN Features

$$\text{MSCN}(i,j) = \frac{I(i,j) - \mu(i,j)}{\sigma(i,j)}$$

where $\mu(i,j)$ and $\sigma(i,j)$ are the local mean and standard deviation of the pixel intensity $I(i,j)$.

3.3.9.2 BRISQUE Quality Score

$$\text{Quality Score} = f(\text{MSCN Features})$$

where f represents the mapping function learned by the SVM.

Despite its simplicity, BRISQUE is statistically superior to traditional full-reference metrics like PSNR and SSIM and is highly competitive with other contemporary NR IQA algorithms. It boasts low computational complexity, making it suitable for real-time applications and practical for distortion identification. Additionally, BRISQUE features can enhance non-blind image denoising algorithms by providing a blind image denoising capability.

Pros:

- No-reference metric, making it effective for real-world dehazing where ground truth is unavailable.
- Analyzes natural scene statistics, which correlates well with human perception.

Cons:

- Limited sensitivity in dense haze cases, where structural details are heavily distorted.
- Less reliable in extreme low-light or high-haze images, where scene statistics vary widely.

3.3.10 NIQE

The aim of blind image quality assessment (IQA) research is to develop perceptual models that can estimate the quality of distorted images with minimal prior knowledge. While many current no-reference (NR) IQA algorithms rely on training data with human opinion scores and knowledge about expected distortions, the Natural Image Quality Evaluator (NIQE)(54) offers a "completely blind" approach.

NIQE does not require exposure to or training on human-rated distorted images. Instead, it relies on measurable deviations from statistical regularities observed in natural images. NIQE employs a straightforward and effective spatial domain natural scene statistic (NSS) approach to create a collection of statistical features that are sensitive to image quality.

3.3.10.1 Natural Image Quality Evaluator (NIQE)

NIQE evaluates image quality based on how much an image deviates from natural scene statistics, which are statistical regularities present in undistorted natural images. The model uses features derived from these statistics to assess image quality without requiring any prior training data on distorted images.

According to experimental results, NIQE performs better than well-trained NR IQA models in terms of accuracy and effectiveness. Its "blind" nature and reliance on natural scene statistics make it a robust choice for quality assessment where traditional training data is unavailable.

3.3.10.2 NIQE Feature Extraction

NIQE extracts features based on the deviation from natural scene statistics (NSS). This involves:

- Estimating Natural Scene Statistics:

$$\text{NSS Features} = f(\text{Image Data})$$

where f represents the process of deriving NSS features from the image data.

- Quality Score Calculation:

$$\text{Quality Score} = g(\text{NSS Features})$$

where g is the mapping function used to compute the final quality score based on the extracted features.

The efficiency of NIQE lies in its ability to provide reliable quality assessments without the need for large datasets or specific distortion types.

Finally, the quality of the distorted image is expressed as the distance between the quality-aware NSS feature model and the multivariate Gaussian (MVG) fit to the features extracted from the distorted image:

$$D(\nu_1, \nu_2, \Sigma_1, \Sigma_2) = \sqrt{\left((\nu_1 - \nu_2)^T \left(\frac{\Sigma_1 + \Sigma_2}{2}\right)^{-1} (\nu_1 - \nu_2)\right)}$$

where ν_1, ν_2 are the mean vectors and Σ_1, Σ_2 are the covariance matrices of the natural MVG model and the distorted image's MVG model, respectively.

Pros:

- Another no-reference metric that is effective for large datasets without ground-truth images.
- Utilizes natural image statistics, providing insights on general quality without specific comparisons.

Cons:

- May not capture fine perceptual details well, particularly in dehazing tasks.
- Lacks robustness in challenging conditions, such as dense haze or night-time haze.

3.4 Performance Comparison

This section presents a detailed evaluation of different image quality metrics used in haze removal. The analysis is conducted using benchmark datasets such as **DenseHaze,**

RESIDE6K, and Nighttime (65)(66)(67), which are specifically selected for their effectiveness in assessing dehazing performance.

To align with human perception, **36 hazy and haze-free images** are extracted from these datasets. Quality assessments are then collected from **115 participants**, leading to the development of a dataset named **Human-Level Perception for Haze Quality Assessment (HLHQA)**.

3.4.1 Dataset Selection

DenseHaze(65) : The DenseHaze dataset comprises 33 pairs of real-world hazy and corresponding clear images, capturing various outdoor environments under natural haze conditions. This dataset presents a significant challenge for dehazing algorithms, as it closely replicates real-world scenarios. The inclusion of diverse outdoor scenes enables a thorough evaluation of dehazing techniques across different illumination and environmental settings.

RESIDE6K(66) : RESIDE6K is a large-scale dataset designed to facilitate the training and assessment of dehazing models using synthetic haze. It consists of 6,000 training images, evenly distributed between 3,000 indoor and 3,000 outdoor scenes, each paired with its corresponding haze-free version. Additionally, a separate test set comprising 1,000 images (500 indoor and 500 outdoor) allows for standardized performance evaluation. The synthetic haze in RESIDE6K is generated using atmospheric scattering models, ensuring realistic haze effects that support comprehensive training and testing across both indoor and outdoor environments.

Daytime and Nighttime Dehazing Benchmarking Database (67): This database consists of both real and synthetic hazy images, each paired with its corresponding ground truth clear image. It encompasses a variety of lighting conditions in both daytime and nighttime scenes. With a total of 16 images, the dataset is specifically designed to evaluate the robustness of dehazing models under different illumination levels and environmental conditions. Its diverse lighting scenarios make it particularly valuable for assessing model performance and generalization in challenging low-visibility and non-uniform illumination conditions, which are critical for nighttime dehazing applications.

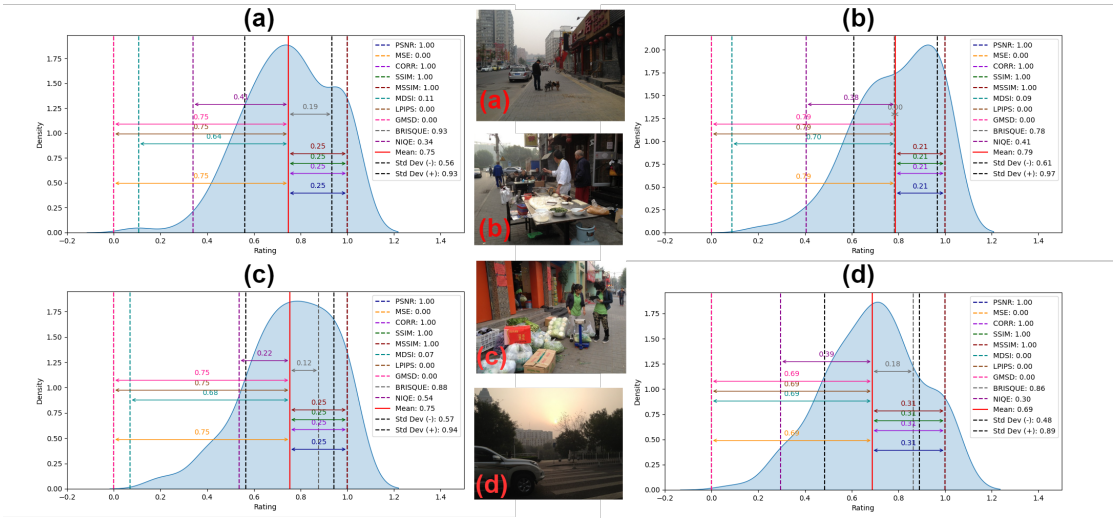

FIGURE 3.2: Correlation with Human Perception in no haze images

3.4.2 Performance Criteria

To evaluate the effectiveness of each metric, I curate a dataset of 36 images sourced from the RESIDE6k, DenseHaze, and Nighttime Haze datasets (65)(66)(67). This selection enables a comprehensive assessment under diverse haze and lighting conditions. Each image is assigned a visibility rating on a scale of 0 to 10, representing its perceived clarity and quality. These ratings are then normalized to a 0–1 scale to ensure consistency in comparisons.

To quantify perceived visibility, I analyze the distribution of normalized ratings and compute both the mean (μ) and standard deviation (σ) for each image's visibility scores. To maintain comparability, all performance metrics are similarly normalized to a 0–1 scale.

The performance of each metric is evaluated based on its alignment with human perception:

- **Optimal Performance:** A metric is considered highly effective if its values closely match the mean (μ) of the visibility distribution, indicating a strong correlation with human perception.
- **Good Performance:** Metrics falling within one standard deviation ($\mu \pm \sigma$) of the visibility distribution are regarded as reliable, as they demonstrate reasonable alignment with human perception.
- **Less Reliable Performance:** Metrics that fall outside the range of ($\mu \pm \sigma$) are considered less dependable, as they deviate significantly from the visibility ratings provided by human evaluators.

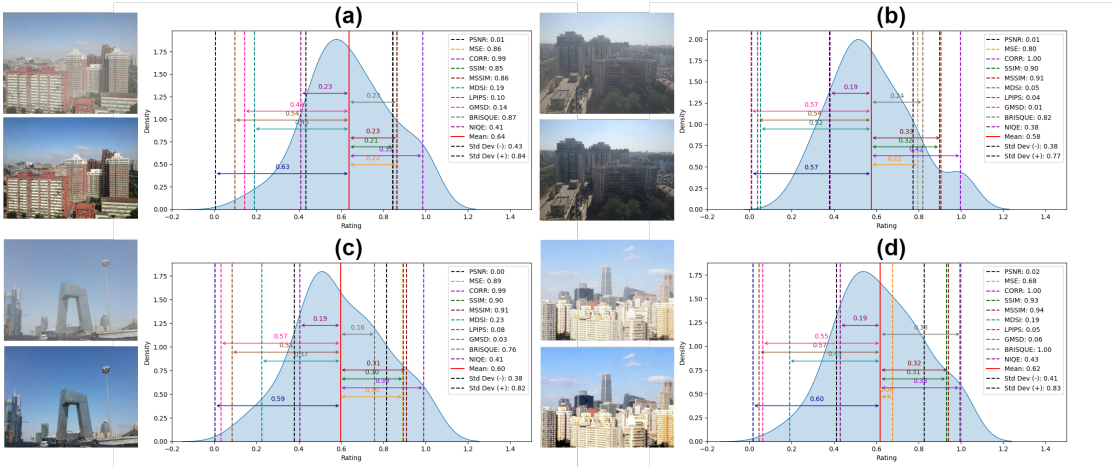

FIGURE 3.3: Correlation with Human Perception in low haze images

This evaluation framework prioritizes metrics that closely reflect human perception, ensuring robust and interpretable comparisons.

3.4.3 Correlation with Human Perception

To evaluate the alignment of metric performance with human perception, comparisons are carried out across four conditions: clear (haze-free) images, low haze, dense haze, and nighttime haze, using the HLHQA dataset.

3.4.3.1 Performance on No-Haze Images

The performance of various metrics on identical haze-free images, in comparison to human perception, is illustrated in Figure 3.2. Four images were analyzed for this assessment.

For Figure 3.2(a), the mean Human-Level Perception (HLP) score is 0.75, with a standard deviation of 0.19. The normalized BRISQUE metric falls within this standard deviation, maintaining a distance of only 0.19 from the mean. In contrast, metrics such as PSNR, CORRelation, SSIM, and MSSIM exhibit greater deviations, with a mean distance of 0.25, placing them outside the standard deviation range.

Similarly, for Figure 3.2(b), the mean HLP score is 0.79 with a standard deviation of 0.18. Here, the normalized BRISQUE metric registers a value of 0.78, remaining within the standard deviation range with a mean deviation of just 0.1. In contrast, PSNR, CORRelation, SSIM, and MSSIM show larger deviations of 0.21, exceeding the standard deviation threshold.

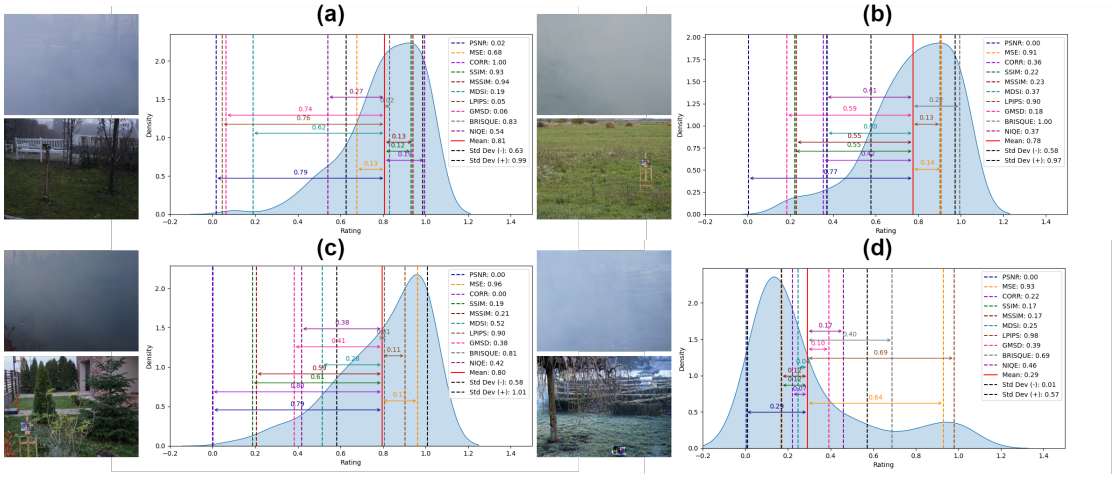

FIGURE 3.4: Correlation with Human Perception in dense haze images

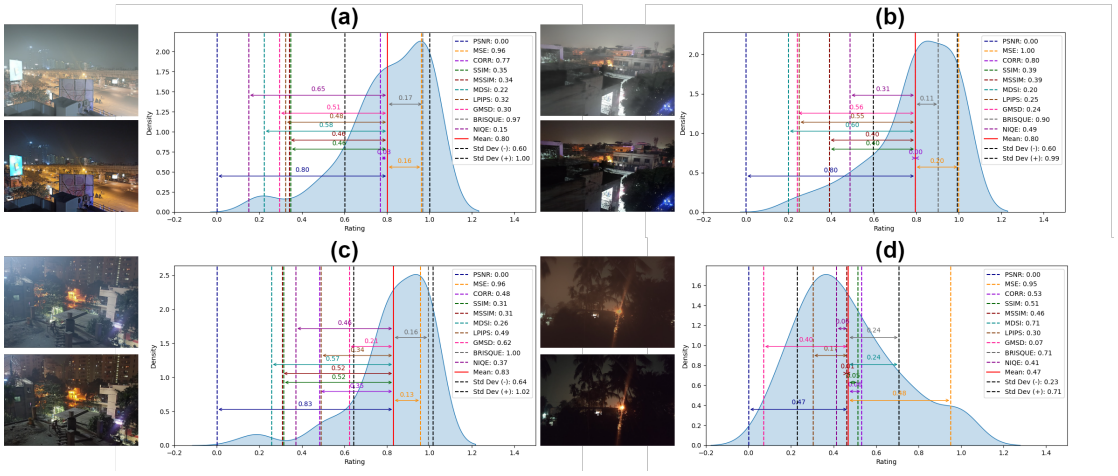

FIGURE 3.5: Correlation with Human Perception in night haze images

A similar pattern is observed in Figure 3.2(c) and (d), where only BRISQUE remains within the standard deviation, with distances from the mean of 0.12 and 0.18, respectively. Conversely, MSE, LPIPS, and GMSD exhibit the highest deviations from the mean, indicating a weaker correlation with human perception.

3.4.3.2 Performance on Low-Haze Images

The performance of various metrics on low-haze images, in comparison to human perception, is depicted in Figure 3.3.

In Figure 3.3(a), the mean Human-Level Perception (HLP) score is 0.64, with a standard deviation of 0.20. None of the evaluated metrics fall within this standard deviation; however, SSIM is the closest with a value of 0.85, followed by normalized MSE and



FIGURE 3.6: Qualitative and quantitative comparison using parameters.

MSSIM at 0.86, normalized NIQE at 0.41, and normalized BRISQUE at 0.87, indicating some degree of similarity to HLP.

For Figure 3.3(b), the mean HLP score is 0.58. Here, NIQE exhibits the smallest deviation from the mean at 0.19, placing it within the standard deviation range. Although MSE and BRISQUE show relatively lower deviations, they remain outside this range.

In Figure 3.3(c), where the mean HLP score is 0.60, BRISQUE and NIQE display the lowest mean deviations of 0.16 and 0.19, respectively. Similarly, in Figure 3.3(d), with an HLP mean of 0.62, NIQE and MSE exhibit minimal deviations of 0.19 and 0.06.

Overall, the results indicate that NIQE and BRISQUE closely align with human perception, while SSIM, MSSIM, and MSE demonstrate moderate agreement in low-haze conditions.



FIGURE 3.7: Qualitative and quantitative comparison using parameters.

3.4.3.3 Performance on Dense Haze Images

The performance of various metrics on dense haze images, relative to human perception, is illustrated in Figure 3.4.

In Figure 3.4(a), the mean Human-Level Perception (HLP) score is 0.81, with a standard deviation of 0.18. Among the evaluated metrics, BRISQUE is the closest to the mean, with a minimal deviation of 0.02. Additionally, MMSIM, SSIM, and MSE fall within the standard deviation range.

For Figure 3.4(b), the mean HLP score is 0.78, with a standard deviation of 0.18. Here, LPIPS and MSE show the smallest deviations from the mean, at 0.13 and 0.14, respectively, both within the standard deviation range.

Similarly, in Figure 3.4(c), where the mean HLP score is 0.80 with a standard deviation of 0.22, BRISQUE exhibits the smallest deviation from the mean, followed by LPIPS

and MSE, which remain within the standard deviation range with deviations of 0.11 and 0.17, respectively.

Finally, in Figure 3.4(d), the mean HLP score is 0.29. Here, MDSI, CORR, SSIM, MSSIM, GMSD, and NIQE all fall within the standard deviation range.

These findings indicate that LPIPS, MSE, SSIM, and MSSIM are well-suited for dense haze scenarios, as their values closely align with human perception.

3.4.3.4 Performance on Night Haze Images

The performance of various metrics on night haze images, in comparison to human perception, is shown in Figure 3.9.

In Figure 3.9(a), the mean Human-Level Perception (HLP) score is 0.80, with a standard deviation of 0.20. Among the metrics, CORR is the closest to the mean, with a minimal deviation of 0.03. BRISQUE and MSE also fall within the standard deviation range, with deviations of 0.17 and 0.16, respectively.

For Figure 3.9(b), the mean HLP score remains 0.80, with a standard deviation of 0.20. Here, CORR aligns exactly with the mean, showing a deviation of 0.0, while BRISQUE and MSE remain within the standard deviation range, with deviations of 0.20 and 0.11, respectively.

TABLE 3.2: Comparison of Metrics Across Different Conditions

Metrics	Hazy	Blur	Colorshift	Gaussian	Reduce Contrast	Distorted	Halo effect	Haze free	Average Change
PSNR	28.21	29.01(-1.4%)	28.72(-0.9%)	28.24(-0.1%)	28.17(0.1%)	28.24(-0.1%)	29.06(-1.5%)	128.00(-63.9%)	0.67%
MSE	99.43	87.63(6.3%)	91.32(4.3%)	98.09(0.7%)	100.21(-0.4%)	98.08(0.7%)	87.36(6.5%)	0.00(100%)	3.13%
Corr	0.551	0.642(-7.7%)	0.633(-7.0%)	0.589(-3.4%)	0.650(-8.3%)	0.589(-3.4%)	0.467(8.2%)	1.00(-29.0%)	6.32%
SSIM	0.566	0.570(-0.4%)	0.631(-5.4%)	0.223(43.4%)	0.453(11.1%)	0.223(43.5%)	0.501(6.1%)	1.00(-27.7%)	18.31%
MSSIM	0.555	0.563(-0.7%)	0.621(-5.6%)	0.229(41.5%)	0.449(10.6%)	0.229(41.5%)	0.496(5.6%)	1.00(-28.6%)	17.58%
MDSI	0.039	0.036(4.3%)	0.033(7.5%)	0.032(9.0%)	0.045(-7.8%)	0.032(9.0%)	0.032(8.9%)	0.00(100%)	7.74%
LPIPS	0.367	0.510(-16.3%)	0.339(3.9%)	0.822(-38.3%)	0.419(-6.7%)	0.821(-38.2%)	0.422(-7.0%)	0.00(100%)	18.40%
GMSD	0.003	0.004(-9.3%)	0.003(10.4%)	0.004(-7.3%)	0.003(-0.3%)	0.004(-7.2%)	0.011(-56.4%)	0.00(100%)	15.14%
BRISQUE	9.74	8.18(0.9%)	9.29(2.4%)	10.66(-4.5%)	7.90(10.4%)	10.66(-4.5%)	9.17(3.0%)	10.09(-1.8%)	5.59%
NIQE	13.36	14.72(-0.5%)	14.10(-2.7%)	16.60(-10.8%)	14.33(-3.5%)	15.97(-8.9%)	10.49(12.0%)	12.16(4.7%)	7.14%

Figure 3.9(c) has a mean HLP score of 0.83 with a standard deviation of 0.19. In this case, BRISQUE and MSE fall within the standard deviation range, with deviations of 0.16 and 0.13, respectively.

Similarly, Figure 3.9(d) has a mean HLP score of 0.47 with a standard deviation of 0.24. Here, metrics such as MSSIM, SSIM, CORR, LPIPS, MDSI, and BRISQUE remain within the standard deviation range. These results indicate that BRISQUE, CORR, and MSE are the most reliable metrics for evaluating night haze images, as they closely align with human-level perception (HLP).

3.4.4 Sensitivity to Distortions

This section examines the sensitivity of various image quality metrics to different types of distortions, including blur, color shift, Gaussian noise, reduced contrast, structural distortion, and halo effects. These distortions are applied to hazy images, and the corresponding metric responses are analyzed to quantify their sensitivity. Table 3.2 summarizes the percentage changes in metric values for each type of distortion, while Figure 3.6 and Figure 3.7 visually illustrate the distortions and the respective metric variations.

For blur, LPIPS and GMSD exhibit high sensitivity, whereas SSIM, MSSIM, NIQE, and BRISQUE are comparatively less affected. In the case of color shift, GMSD, MDSI, and CORR show significant sensitivity, while PSNR and NIQE remain largely unaffected. Gaussian noise has a strong impact on SSIM, MSSIM, and LPIPS, whereas PSNR and MSE demonstrate minimal sensitivity.

When contrast is reduced, CORR, SSIM, MSSIM, and BRISQUE exhibit notable sensitivity. LPIPS and MDSI also show some sensitivity, though to a lesser extent, while PSNR, MSE, and GMSD are relatively unaffected.

For structural distortion, SSIM, PSNR, and LPIPS demonstrate high sensitivity, followed by MDSI, NIQE, and GMSD, while PSNR and MSE remain the least sensitive. Finally, in the case of halo effects, GMSD is highly sensitive, with NIQE, CORR, and MDSI showing moderate sensitivity, whereas PSNR is the least affected.

Overall, LPIPS, SSIM, MSSIM, and GMSD prove to be highly effective metrics for assessing image quality under various distortions, making them well-suited for evaluating dehazing performance. In contrast, PSNR and MSE exhibit very low sensitivity to distortions and are therefore less effective in capturing their impact.

3.5 GUI

The **Image Quality Assessment Tool** is a user-friendly graphical user interface (GUI) developed using the Streamlit (68) library in Python 3.10. It is designed to facilitate the simultaneous computation of multiple image quality metrics. The GUI includes an *"About"* page, which provides detailed explanations and definitions of the various metrics used for image quality evaluation, ensuring users have a comprehensive understanding of the available tools.

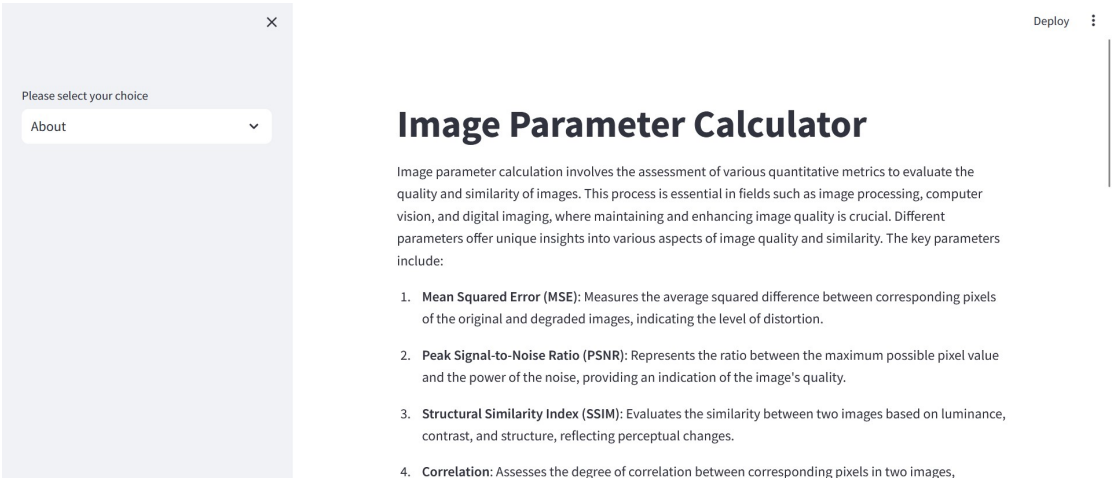

FIGURE 3.8: Image Parameter Calculation Graphical User Interface

This tool enables comprehensive analysis of image fidelity, degradation, and perceptual quality by computing a variety of metrics in parallel. These include:

- **Distortion Metrics**: Mean Squared Error (MSE), which quantifies the average squared difference between original and distorted images.
- **Overall Quality**: Peak Signal-to-Noise Ratio (PSNR), a widely used measure of image reconstruction quality. [•] **Perceptual Similarity**: Structural Similarity Index (SSIM) and Multi-Scale SSIM, which assess visual resemblance based on human perception.
- **Advanced Perceptual Quality**: Mean Deviation Similarity Index (MDSI) and Learned Perceptual Image Patch Similarity (LPIPS), which evaluate quality based on deep learning and perceptual differences.
- **Pixel Matching**: Correlation, which measures the similarity of pixel intensity patterns.
- which estimate quality without a reference image using statistical features.

By incorporating a variety of metrics, the tool enables both subjective and objective image quality assessments. This makes it an essential resource for researchers and industry professionals looking for thorough analysis and accurate image evaluation.

On the second screen of the GUI, users can upload a hazy image along with its corresponding ground truth image to compute image quality metrics. Once processed, the results are presented in a clear table format, displaying values for metrics such as PSNR,

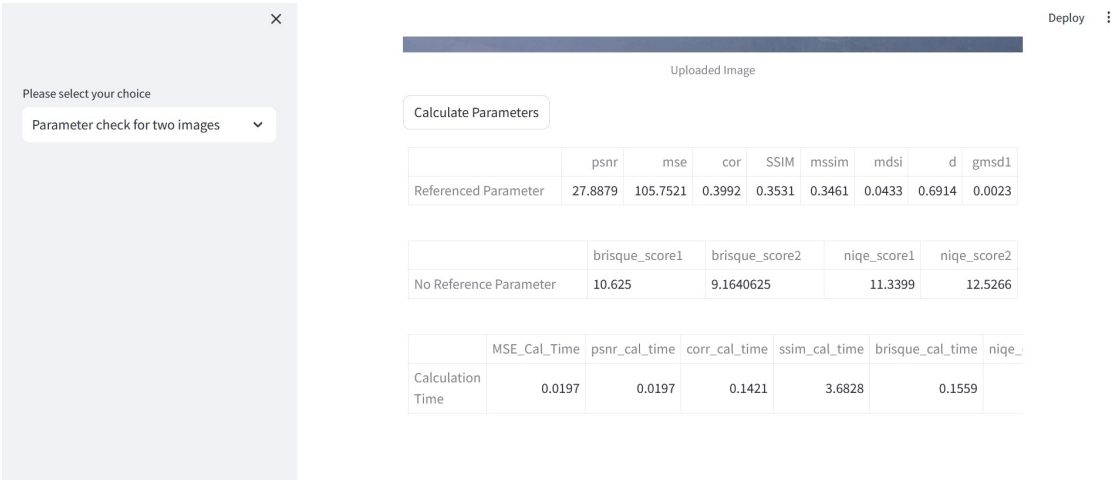

FIGURE 3.9: Image Parameter Calculation Graphical User Interface for Calculation Page

MSE, and SSIM. Additionally, the computation time for each parameter is shown, allowing users to efficiently assess the quality and similarity between the hazy and reference images.

3.6 Challenges and Limitations

Accurately evaluating the quality of dehazed images presents significant challenges due to the complex interplay between objective metrics and subjective human perception, particularly under different haze conditions. Below, I highlight the key challenges in this domain.

- **Alignment with Human Perception:** One of the key challenges in dehazing evaluation is the discrepancy between objective image quality metrics and human perceptual judgments across varying haze conditions. While some metrics, such as normalized BRISQUE, exhibit a stronger correlation with human-level perception (HLP) under controlled conditions, others—like PSNR, CORR, SSIM, and MSSIM—often fail to capture subtle perceptual details, particularly in dense or nighttime haze. For instance, normalized BRISQUE tends to fall within the standard deviation range of HLP, whereas MSE and LPIPS show significant deviations in high-density haze, highlighting the need for more perceptually relevant metrics that can reliably assess dehazing quality in diverse scenarios.
- **Lack of Dehazing-Specific IQA Metrics:** The absence of standardized image quality assessment (IQA) metrics tailored specifically for dehazing poses a major

challenge in ensuring consistent evaluation. Widely used metrics such as PSNR, SSIM, and MSE, while effective for general IQA, fail to account for haze-specific factors like depth perception and contrast restoration, which play a crucial role in the perceived clarity of dehazed images. This limitation makes it difficult to compare dehazing methods effectively, underscoring the need for dedicated IQA metrics that address the unique characteristics of haze removal.

- **Inconsistencies in Subjective Assessment and Dataset Limitations:** Subjective assessments provide valuable insights into perceptual quality, but they often suffer from inconsistencies among human evaluators, particularly when evaluating images under different haze densities and lighting conditions. This variability reduces the reliability of subjective assessments as reference benchmarks. Furthermore, existing dehazing datasets lack sufficient diversity to fully represent real-world haze conditions, limiting the generalizability of dehazing techniques. Expanding datasets to encompass a broader range of haze types and environmental conditions would strengthen both objective and subjective evaluations, improving the reliability of dehazing research.
- **High Computational Cost of Deep Learning-Based Metrics:** Deep learning-based IQA metrics, such as LPIPS, have demonstrated strong alignment with human perception but are computationally expensive, making them impractical for real-time or resource-constrained applications. This high computational demand presents a challenge for widespread adoption, especially in edge-computing environments where efficiency is critical. Developing lightweight, perceptually accurate IQA metrics remains an important research goal to balance assessment quality with computational efficiency, enabling broader applicability across different use cases.

These challenges highlight the necessity for advancements in dehazing IQA metrics, emphasizing perceptual consistency, computational efficiency, and diverse datasets to ensure accurate and reliable evaluations.

3.7 Future Directions

To further improve image quality assessment (IQA) for dehazing, several promising research directions can be explored:

- **Development of Dehazing-Specific IQA Metrics:** Existing IQA metrics, while useful, often fail to capture the unique perceptual characteristics of dehazed

images. Future research should focus on creating specialized metrics that better align with human perception, particularly in areas such as depth restoration, contrast enhancement, and edge sharpness. Tailoring metrics to haze-specific challenges would improve evaluation accuracy across different haze conditions, leading to more reliable assessments of dehazing algorithms.

- **Leveraging AI and Machine Learning for IQA:** AI and machine learning present significant opportunities for enhancing IQA in dehazing. Techniques such as GAN-based metrics and perceptual loss functions, which have proven effective in other vision tasks, could be adapted to better capture human-perceived quality in dehazed images. Training these models on human-labeled datasets would make IQA metrics more perceptually relevant. Additionally, AI-driven IQA models could enable real-time evaluation in resource-constrained environments, expanding their practical applications.

- **Hybrid Metrics Combining Objective and Subjective Evaluations:** A promising approach involves developing hybrid metrics that integrate traditional objective measures (e.g., SSIM, MSE) with subjective perceptual factors. By dynamically weighting attributes such as haze intensity, depth perception, and visual clarity, these metrics could provide scores that better reflect human judgment. Incorporating user feedback mechanisms could further refine these metrics, ensuring they adapt to specific dehazing requirements.

- **Application-Specific IQA Metrics for Dehazing:** Different applications have distinct dehazing requirements. For instance, autonomous navigation systems prioritize object detectability and depth accuracy, while surveillance applications focus on sharpness and detail retention. Future research could develop specialized IQA metrics tailored to the needs of various domains, enhancing their performance and reliability in real-world scenarios.

- **Combining Classical and Learned IQA Metrics:** Integrating traditional IQA metrics, which assess structural fidelity, with machine learning-based metrics, which better capture perceptual alignment, could improve overall assessment accuracy. A hybrid approach that combines conventional metrics (e.g., SSIM, MSE) with learned models (e.g., GAN-based perceptual loss) could provide a more comprehensive evaluation framework. This would be particularly beneficial for analyzing complex or severely degraded images, where traditional methods fall short.

- **Multi-Modal Inputs for Enhanced Dehazing IQA:** Most existing IQA metrics rely solely on RGB images, limiting their ability to fully assess haze effects. Incorporating additional modalities—such as depth information, infrared (IR) imaging, or environmental data—could provide a more holistic understanding of haze severity and spatial depth. Multi-modal approaches would improve metric robustness and adaptability across different environmental conditions, leading to more reliable IQA for dehazing.
- **Ensuring Temporal Consistency in Video Dehazing IQA:** As dehazing techniques extend to video applications, maintaining temporal consistency becomes crucial to preserving visual coherence across frames. Existing IQA metrics designed for static images often overlook temporal aspects, leading to flickering or other artifacts in dehazed videos. Future research should focus on developing IQA metrics that incorporate both spatial and temporal consistency, ensuring smoother, more natural-looking video dehazing results.

By addressing these future directions, the field of dehazing IQA can advance toward more perceptually accurate, computationally efficient, and application-specific solutions, ultimately improving the evaluation and effectiveness of dehazing techniques.

These research directions provide a comprehensive roadmap for improving IQA in dehazing, with potential benefits extending to various computer vision applications.

3.8 Discussion

In this chapter, I provide a comprehensive review of 10 commonly used metrics for evaluating the performance of haze removal algorithms, including MSE, PSNR, SSIM, MSSIM, Correlation, MDSI, LPIPS, GMSD, BRISQUE, and NIQE. I introduce a new dataset, the Human-Level Perception for Haze Quality Assessment (HLHQA), which consists of 36 hazy and haze-free images rated on a scale from 0 to 10, serving as a benchmark for human-level perception (HLP). Using HLHQA, I assess and analyze the performance of each metric in relation to human perception across four distinct conditions: no haze, low haze, dense haze, and night haze.

Our findings reveal that BRISQUE aligns most closely with human perception for haze-free images, while both NIQE and BRISQUE exhibit strong correspondence with HLP ratings under low haze conditions. For dense haze, LPIPS, MSE, SSIM, and MSSIM demonstrate high alignment with human perception, whereas BRISQUE, CORR, and MSE prove to be the most effective metrics under night haze conditions. To support

broader adoption, I have also developed a user-friendly GUI that streamlines the evaluation of haze removal models.

Additionally, this chapter discusses the strengths, limitations, and specific challenges associated with each metric, along with future research directions, such as the development of dehazing-specific metrics and enhancements in dataset diversity. Through these insights,I aim to improve the accuracy and reliability of haze removal performance assessments and contribute to the advancement of more perceptually aligned evaluation metrics in the field.

Chapter 4

Parallel Processing of Atmospheric Light and Transmission Coefficient for Image Dehazing

4.1 Introduction

Outdoor images often suffer from degradation due to atmospheric conditions such as fog, smog, and haze. This results in reduced contrast and visibility, affecting applications in autonomous driving, remote sensing, and video surveillance. Traditional dehazing methods include dark channel prior (DCP), contrast enhancement, and learning-based approaches. However, these methods often struggle with real-time performance. In this chapter, a parallel processing approach is introduced to compute atmospheric light estimation (ALE) and transmission coefficient (TC) simultaneously, reducing computational complexity.

4.1.1 Contribution of the Chapter

- A parallel hardware architecture is proposed to efficiently compute airlight estimation and transmission coefficients. Additionally, the airlight estimation process is modified to enhance time efficiency.
- A novel contrast enhancement technique is introduced that eliminates the need for computationally expensive procedures such as soft matting, thereby improving image quality without increasing processing time.
- An automatic gamma correction mechanism is implemented for image enhancement, removing the dependence on prior-based and time-intensive enhancement methods.

4.2 Method 1

In 1924, H. Koschmieder (69) introduced the following mathematical model to represent hazy images:

[0]**A. Ghosh**, A. Dey and S. Sinha Chaudhuri, "A fast restoration of weather degraded images," ICDEC 2022, International Conference on Data, Electronics and Computing (ICDEC-2022).

[0]Dey, A., **Ghosh, A.**, & Chaudhuri, S. S. (2023). *Image Restoration from Weather Degraded Images Using Markov Random Field*. In S. Roy et al. (Eds.), *Innovations in Computational Intelligence and Computer Vision* (pp. 63–72). Springer Nature Singapore.

[0]U. Biswas, A. Karmakar, **A. Ghosh** and S. S. Chaudhuri, "Enhancing Image Clarity in Real Time: An Automated Gamma Correction Approach for Dehazing," *2023 7th International Conference on Electronics, Materials Engineering Nano-Technology (IEMENTech)*, Kolkata, India, 2023, pp. 1-6, doi: 10.1109/IEMENTech60402.2023.10423457.

$$I(x) = J(x)t(x) + A(1 - t(x)) \tag{4.1}$$

where $J(x)$ represents the original scene without haze, $t(x)$ is the transmission coefficient, A denotes the atmospheric light, and $I(x)$ is the observed hazy image.

Analyzing the equation reveals that the only known parameter is the hazy image $I(x)$, whereas the haze-free image $J(x)$, transmission coefficient $t(x)$, and atmospheric light A remain unknown.

The estimation of these three unknown parameters involves three primary steps: 1. **Atmospheric Light (A) Estimation**: This step consists of two subparts—first, computing the dark channel and then estimating the atmospheric light. The **Dark Channel Prior (DCP)** method, introduced by Kaiming He et al. in 2009 (18), is used for this purpose. The dark channel is computed as:

$$I^{dark}(x) = \min_{y \in \Omega(x)} \left(\min(I^C(y))\right) \tag{4.2}$$

where $\Omega(x)$ represents a local patch centered at x, and C corresponds to the color channels {Red, Green, Blue}. The dark channel primarily highlights the shadowed or non-illuminated regions in an image. The atmospheric light A is estimated as the top 0.1% brightest pixels in the dark channel.

2. **Transmission Coefficient ($t(x)$) Estimation**: When haze distribution is homogeneous, the transmission coefficient follows the relation:

$$t(x) = e^{-d(x)} \tag{4.3}$$

where $t(x)$ denotes the scattering coefficient of the atmosphere, and $d(x)$ represents the scene depth. This equation illustrates the attenuation effect of haze based on distance d. Using aerial perspective, the transmission coefficient is further refined in the **HSV color model**. The values of **Saturation ($S(x)$) and Value ($V(x)$)** components are defined as follows (19):

$$S(x) = \begin{cases} 0, & \text{if } \max\limits_{C \in \{R,G,B\}} I^C(x) = 0, \\ 1 - \dfrac{\min\limits_{C \in \{R,G,B\}} I^C(x)}{\max\limits_{C \in \{R,G,B\}} I^C(x)}, & \text{otherwise.} \end{cases} \tag{4.4}$$

$$V(x) = \max_{C \in \{R,G,B\}} I^C(x) \tag{4.5}$$

Once $S(x)$ and $V(x)$ are computed, the **transmission coefficient** can be estimated using the depth function in the HSV model:

$$d(x) = \theta_0 + \theta_1 S(x) + \theta_2 V(x) \tag{4.6}$$

where the parameters are assigned values as $\theta_0 = 0.12$, $\theta_1 = 0.96$, and $\theta_2 = -0.78$ (19). Since $S(x)$ and $V(x)$ are independent, this formulation enables **parallel computation** of Atmospheric Light Estimation (ALE) and Transmission Coefficient (TC).

3. **Scene Recovery ($J(x)$)**: The final step involves reconstructing the haze-free scene using the following equation, derived from Equation (1) :

$$J(x) = \frac{I(x) - A}{\max(t(x), t_0)} + A \tag{4.7}$$

where $J(x)$ represents the recovered haze-free image, and t_0 is a lower bound for the transmission coefficient to prevent excessive amplification of noise in low-transmission regions.

4.2.1 Proposed Method

In a hazy image, brightness and saturation vary depending on the density of the haze. For a haze-free image, the difference between saturation and brightness is close to zero. Leveraging this property, a parallel architecture is proposed, where Atmospheric Light Estimation (ALE) and the transmission coefficient are computed simultaneously. To further enhance image quality, a contrast enhancement technique is applied. The parallel computation significantly reduces the overall time complexity. Atmospheric light is estimated in the RGB color model, ensuring efficient and accurate dehazing.

The following flowchart illustrates the step-by-step procedure of the proposed dehazing algorithm. Initially, Atmospheric Light Estimation (ALE) and the Transmission Coefficient (TC) are computed in parallel. Next, the scene is recovered, and finally, a contrast enhancement technique is applied to improve the image quality.

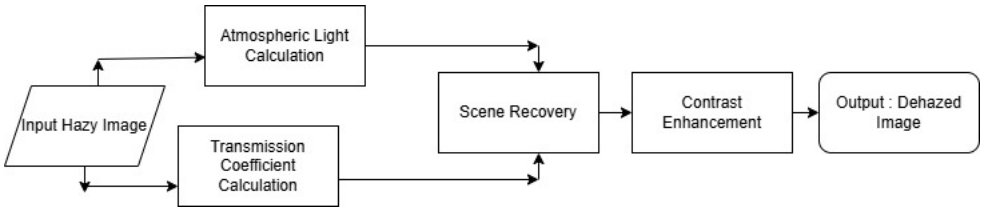

FIGURE 4.1: Flowchart of the Proposed Dehazing Algorithm

4.2.2 Contrast Enhancement

After scene recovery, a contrast enhancement method is applied to further refine the image quality. The contrast factor for the entire image is first computed using the equation below. To enhance contrast, an additional weight is assigned to each pixel, ensuring a more vivid and visually appealing output.

$$C = int\left(\frac{C_{Max}}{2}\right) \tag{4.8}$$

$$contrast = int\left(\frac{(contrast) \times 2C}{C_{Max} - C}\right) \tag{4.9}$$

Here, C_{Max} represents the maximum intensity of any color channel in the RGB model. If the computed contrast falls below a predefined threshold, it is adjusted accordingly to ensure optimal image enhancement.

4.2.3 Experimental Observations

The experiment is processed in a device with 16GB RAM, AMD Ryzen 5 5500U, 2.10Ghz Processor and Windows 11 Home Single Language operating system. The qualitative result with different images are shown in Table 2 with available data sets used in different algorithms. Also the quantitative analysis of no-reference parameter is shown in table 1. Structural Similarity Index (SSIM), Mean Square Error(MSE), Correlation(Cor) and Peak Signal to Noise Ratio(PSNR(dB)) is shown in the case of quantitative analysis.

Table 3 below displays the qualitative results of this algorithm's comparison with other current approaches. In particular, I have compared it to Meng's algorithm (70), the Dark Channel Prior-based approach (18), the Color Attenuation Prior-based method (19), and histogram equalization (H.E.). This algorithm maintains a lower computational complexity while exhibiting competitive performance.

TABLE 4.1: Comparison of Reference Image Quality Parameter for Images

Serial No	Image	SSIM	PSNR(dB)(dB)	MSE	Cor
1	fishers	0.9911	35.7303	17.37982	0.99774
2	foggy˙bench	0.9660	29.9711	65.4586	0.9903
3	foggy˙oaks	0.9073	31.4246	46.8402	0.9861
4	foggyHouse	0.9665	28.8945	83.8741	0.9955
5	Haze.jpg	0.9126	30.6263	56.2916	0.9980
6	hazyDay˙input	0.9592	28.9899	82.0509	0.9939
7	house˙input.jpg	0.87603	28.1955	98.5204	0.9925
8	lilyhazy	0.9469	29.5462	72.1869	0.9986
9	marin-headlands-bridge	0.8325	29.9279	66.1128	0.9966
10	moebius˙input	0.9570	29.3647	75.2675	0.9952
11	mountain-input	0.9460	28.4774	92.3289	0.9924
12	trees	0.8596	27.4586	116.7397	0.9893

TABLE 4.2: Computational Complexity for proposed method

Serial No	Image	Image Size	TC(in secs)
1	fishers	346*512*3	2.0914
2	foggy˙bench	600*800*3	5.5734
3	foggy˙oaks	376*520*3	2.2424
4	foggyHouse	1536*2048*3	29.7202
5	Haze.jpg	300*400*3	1.0901
6	hazyDay˙input	576*768*3	3.9548
7	house˙input.jpg	448*440*3	2.3640
8	lilyhazy	480*640*3	2.8576
9	marin-headlands-bridge	680*1024*3	8.0971
10	moebius˙input	956*1200*3	9.7631
11	mountain-input	384*512*3	2.3341
12	trees	723*1076*3	8.6899

The computational complexity is shown in table 4. TC refers for time complexity of proposed method.

Tables 5, 6, 7, and 8 present a quantitative comparison of various algorithms based on SSIM, MSE, PSNR (dB), and Correlation. The statistical analysis demonstrates competitive performance compared to other algorithms.

TABLE 4.3: Experimental results for different videos in proposed

Serial No	Image Name	Hazy Image	Dehaze Image
1	fishers		
2	foggy˙bench		
3	foggy˙oak		
4	foggyhouse		
5	Haze		
6	hazyDay˙input		
7	house˙input		
8	lilyhazy		
9	marin-headlands-bridge		

TABLE 4.4: Qualitative Comparison with Different Algorithms

Hazy Image	H.E.	DCP(18)	CAP(19)	Meng (70)	This Method
		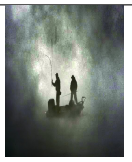			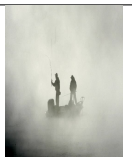
					
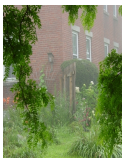	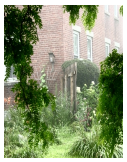		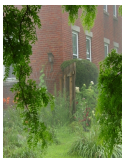		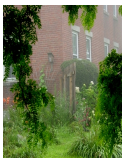
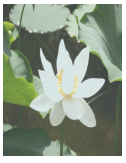					
				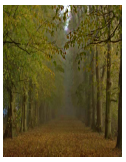	

TABLE 4.5: Quantitative Comparison with Different Algorithms for SSIM

Image Name	H.E.	DCP(18)	CAP(19)	Meng(70)	This Method
fishers	0.6321	0.9364	0.6112	0.4241	0.9911
hazyday	0.7257	0.8674	0.7108	0.5861	0.9592
house	0.7593	0.9751	0.9073	0.8068	0.8760
lilyhazy	0.8029	0.9282	0.7663	0.7472	0.9469
trees	0.6971	0.9548	0.8973	0.9053	0.8596

TABLE 4.6: Quantitative Comparison with Different Algorithms for MSE

Image Name	H.E.	DCP(18)	CAP(19)	Meng(70)	This Method
fishers	115.5912	116.5042	106.6335	99.7171	17.3799
hazyday	82.8156	89.7741	114.5023	107.7012	82.0510
house	105.7126	47.2803	70.7754	84.8389	98.5205
lilyhazy	74.6058	100.1549	109.9089	123.2106	72.1869
trees	107.2912	60.2679	114.7142	116.1447	116.7397

TABLE 4.7: Quantitative Comparison with Different Algorithms for PSNR(dB)(dB)

Image Name	H.E.	DCP(18)	CAP(19)	Meng(70)	This Method
fishers	27.5016	27.4674	27.8519	28.1431	35.7303
hazyday	28.9497	28.5993	27.5427	27.8086	28.9900
house	27.8895	31.3840	29.6320	28.8449	28.1955
lilyhazy	29.4031	28.1241	27.7205	27.2243	29.5462
trees	27.8252	30.3299	27.5346	27.4808	27.4586

TABLE 4.8: Quantitative Comparison with Different Algorithms for Correlation

Image Name	H.E.	DCP(18)	CAP(19)	Meng(70)	This Method
fishers	0.8815	0.9763	0.8018	0.7231	0.9977
hazyday	0.9622	0.9474	0.8997	0.7955	0.9940
house	0.9710	0.9407	0.9068	0.8405	0.9925
lilyhazy	0.9605	0.9938	0.9785	0.9435	0.9987
trees	0.9537	0.8207	0.7644	0.7968	0.9893

4.3 Method 2

4.3.1 Markov Random Field-Based Refinement

Markov Random Fields (MRFs) are extensively employed in image processing, particularly for tasks such as image segmentation. In an MRF framework, each pixel in an image F is assigned a label from a predefined set Ω, which is defined according to a chosen neighborhood structure—commonly 4-connected or 8-connected systems. The goal is to determine the optimal labeling Ω by minimizing the overall energy function given by:

$$V(\Omega, F) = V_1(\Omega, F) + V_2(\Omega) \tag{4.10}$$

Here, $V_1(\Omega, F)$ evaluates the conformity of labels with observed image data, while $V_2(\Omega)$ imposes spatial consistency among neighboring pixels. In our context, the input image F refers to the transmittance map obtained from the HSV color model (19), and the label set Ω is generated by clustering this map. The cost function $V(\Omega, F)$ is minimized to refine the transmittance estimation.

Due to the pixel-wise nature of the HSV-based transmittance map (19), label assignment becomes direct. Let $f(p)$ denote the transmittance value at pixel p, with $f_i \in t$, where t

is the estimated transmission map. The labeling function is denoted as $f_L(p)$, and the original pixel value as $f_i(p)$. The overall energy function to be minimized is defined as:

$$V(f_L) = \sum_{p \in t} V_p(f_L(p), f_i(p)) + \sum_{(p,q) \in N} V_{p,q}(f_L(p), f_L(q)) \tag{4.11}$$

In Equation 4.11, N indicates the set of neighboring pixel pairs (assuming a 4-neighborhood structure), and q refers to the neighbors of pixel p. The first term, V_p, quantifies the fidelity of the assigned label to the observed pixel value and is given by:

$$V_p(f_L(p), f_i(p)) = \omega \times \log((f_L(p) - f_i(p))^2 + 1) \tag{4.12}$$

where ω is a scalar weight that controls the strength of the data term.

The second term in Equation 4.11 encourages smooth transitions between neighboring labels and acts as a regularization term. It is defined as:

$$V_{p,q}(f_L(p), f_L(q)) = \min\left(\omega_1 \times (f_L(p) - f_L(q))^2, \log((f_L(p) - f_L(q))^2 + 1)\right) \tag{4.13}$$

where ω_1 is another weighting factor that balances the smoothness constraint.

To minimize the total MRF energy efficiently, we utilize the graph-cut optimization algorithm as outlined in (71), which provides significant computational advantages over traditional techniques such as Simulated Annealing (72). The initial label assignments for the transmittance map are derived using k-means clustering.

4.3.2 Experimental Results

The experiment was conducted on a system equipped with 6GB RAM, an Intel Core i3-3217U CPU running at 1.80GHz, and the Windows 10 Home Single Language operating system. The initial transmittance map labeling was performed using 24 labels, with parameters $w = 0.2$ and $w_1 = 10$. Table 4.9 presents a comprehensive comparison of the recovered images against the ground truth based on various image parameters, while Table 4.10 visually illustrates the obtained results.

The qualitative performance of this algorithm has been compared with the previously done work by others. Comparison has been done with the results obtained from Dark

TABLE 4.9: Comparison of Reference Image Quality Parameter for Images

Serial No	Image	SSIM	PSNR(dB)(dB)	MSE	Cor
1	merry go round	0.4828	27.7387	109.4477	0.4652
2	children's slide	0.6454	27.8390	106.9483	0.6861
3	bench	0.4010	27.9887	103.3239	0.4741
4	park crossroad	0.4766	27.8945	105.5906	0.5855
5	tree	0.4800	27.8582	106.4780	0.6615
6	swing	0.6241	28.1162	100.3356	0.4784
7	children's cage	0.5627	27.7121	110.1197	0.5856
8	children's playwheel	0.5788	27.8845	105.8351	0.6218
9	slide	0.5159	28.0380	102.1581	0.3144
10	flower graffiti	0.3888	27.7321	109.6136	0.3494
11	road	0.5778	28.1170	100.3161	0.6541
12	tree	0.4813	27.6406	111.9479	0.6521

Channel Prior (18), Color Attenuation Prior (19), and Meng's method (70). The results are provided in table 4.11.

4.4 Method 3

4.4.1 CLAHE Adoption including gamma correction(manual to automate)

4.4.1.1 Contrast-Limited Adaptive Histogram Equalization (CLAHE)

Histogram equalization is a technique used in image processing to enhance contrast by adjusting the intensity distribution of an image. It consists of two main components: (1) Adaptive Histogram Equalization and (2) a Contrast Limiter. A histogram, similar to a bar chart, is a graphical representation of data values. In the context of image processing, histogram equalization enhances the visibility of details by increasing the intensity of the brighter regions while largely preserving the darker regions. This adjustment results in an overall improvement in image contrast (73).

Adaptive Histogram Equalization (AHE) During the histogram equalization process, multiple histograms can be generated for a single image, with each histogram corresponding to a specific region of the image. This technique applies histogram equalization locally to a defined set of pixels, rather than the entire image. The image is divided into small, equal sections known as tiles as stated by authors (74), allowing for

TABLE 4.10: Experimental results for different photos using this method

Serial No	Image Name	Hazy Image	Dehazed Image
1	merry go round		
2	children's slide		
3	bench		
4	park crossroad		
5	tree		
6	swing		
7	children's cage		
8	children's playwheel		
9	slide		

TABLE 4.11: Qualitative Comparison with Different Algorithms

Hazy Image	DCP(18)	CAP(19)	Meng(70)	This Method
				

the independent enhancement of different areas. However, this approach has certain limitations. In regions with nearly uniform intensity, adaptive histogram equalization may excessively amplify contrast, leading to undesirable visual effects as reported by(73).



FIGURE 4.2: Original image,Image after using CLAHE in the figure

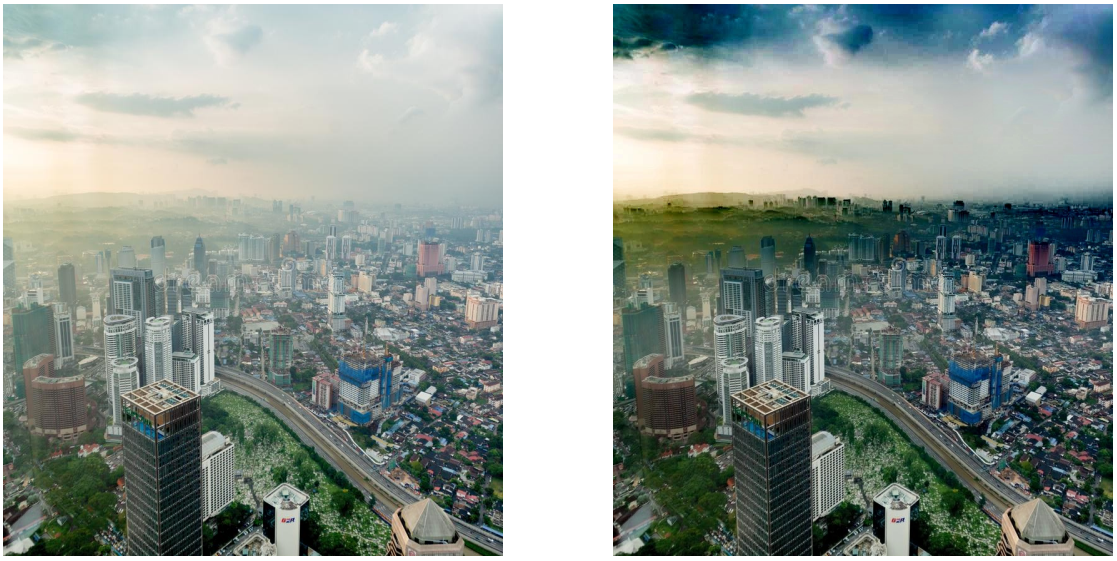

FIGURE 4.3: A city view, Image after using CLAHE in the figure

Contrast-Limited Adaptive Histogram Equalization (CLAHE) One of the limitations of Adaptive Histogram Equalization (AHE) is the over-amplification of nearly uniform regions, which can introduce unwanted noise. CLAHE addresses this issue by incorporating a contrast limiter to control the intensity variation between neighboring pixels as mentioned by authors (74). This prevents excessive contrast enhancement, ensuring a more balanced image adjustment. The equation for CLAHE is given as follows:

$$g(i,j) = \frac{1}{M \times N} \sum_{p=1}^{M} \sum_{q=1}^{N} (f(p,q) - k) \tag{4.14}$$

where $f(p, q)$ represents the input pixel value at coordinates (p, q), M and N denote the dimensions of the local window, and k is a parameter used to regulate the extent of contrast enhancement.

4.4.1.2 Spatial Domain Techniques and Gamma Correction

In spatial domain image enhancement, pixel intensity values are directly modified to enhance image quality. This method is intuitive and aligns well with human visual perception. One of the most common approaches in this domain is gamma correction, which belongs to the category of power-law transformations.

Power-Law Transformation (Gamma Correction)

$$s = c \cdot r^{\gamma} \tag{4.15}$$

In this equation, s is the output pixel value, r is the input pixel value, c is a constant, and γ is the gamma value. Gamma correction adjusts the brightness and contrast of an image by applying a non-linear transformation. When $\gamma < 1$, darker pixel values are expanded to span a broader output range, enhancing visibility in dark regions. Conversely, when $\gamma > 1$, it compresses the intensity range of dark pixels, making the image appear darker overall (75).

This method is widely employed for display correction on various output devices such as LCDs and monitors, where the appropriate gamma value depends on the characteristics of the display system.



FIGURE 4.4: Images with gamma values of 1.0, 1.5, and 2.0 respectively

4.4.1.3 Automatic Gamma Correction Formula

The automatic gamma correction approach adapts the gamma value based on the average brightness of the image, using the formula below:

$$\text{gamma-corrected} = \text{np.array}(255 \cdot (\text{gray}/255)^{\gamma}, \text{dtype='uint8'}) \tag{4.16}$$

Here, the grayscale image is normalized to [0,1], the pixel values are raised to the power of the computed gamma value, then scaled back to [0,255] and cast to an 8-bit unsigned integer format compatible with standard image processing tools.

The gamma value is calculated dynamically as follows:

$$\gamma = \frac{\log_{10}(0.5)}{\log_{10}(\text{avg-pixel-value}/255)} \tag{4.17}$$

This equation aims to modify the gamma such that the average brightness of the image approximates a target mid-tone (0.5). When the average pixel value is low, a smaller gamma brightens the image; conversely, higher average values lead to darker outputs.



FIGURE 4.5: Qualitative comparison: Top - dark channel prior-based methods; Middle - transmission-based method; Bottom - outputs from the proposed method

4.4.1.4 Significance of Automatic Gamma Calculation

The primary advantage of automatic gamma correction lies in its adaptability. Instead of manually setting a gamma value, the system analyzes the image's brightness and selects an optimal gamma dynamically. This ensures consistent image enhancement across a diverse set of images with varying exposure levels. In practice, this correction is often followed by the application of Contrast Limited Adaptive Histogram Equalization (CLAHE) to further boost local contrast and reveal hidden details.

Unlike manual gamma correction, where a fixed gamma is applied to all images, the proposed automatic method tailors the correction to each image individually. This



FIGURE 4.6: Quantitative comparison: Top - dark channel prior-based methods; Middle - color attenuation prior-based method; Bottom - proposed method

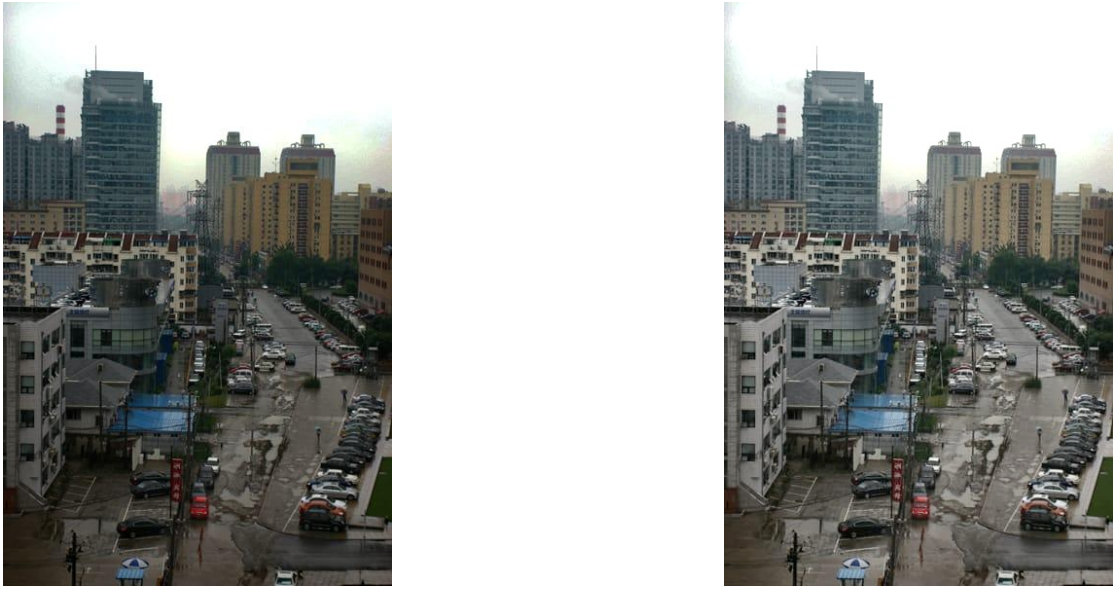

FIGURE 4.7: City view after applying CLAHE and gamma correction

not only saves time but also improves visual consistency across a dataset with varying lighting conditions.

‘

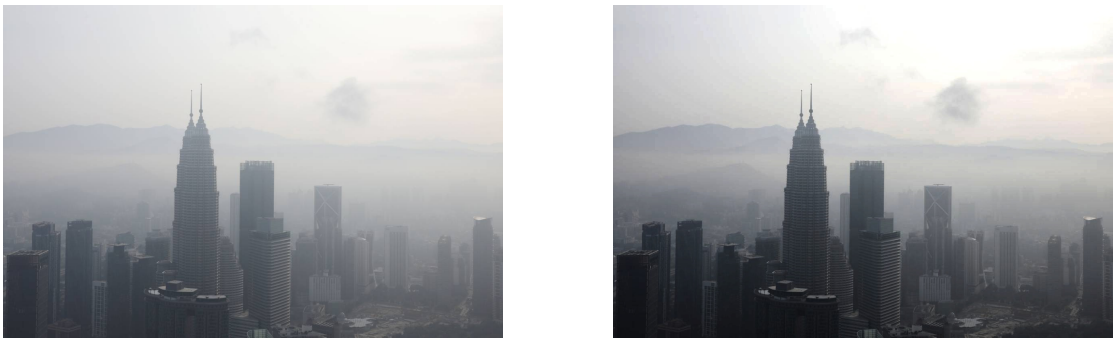

FIGURE 4.8: Outdoor view with CLAHE and gamma correction enhancement

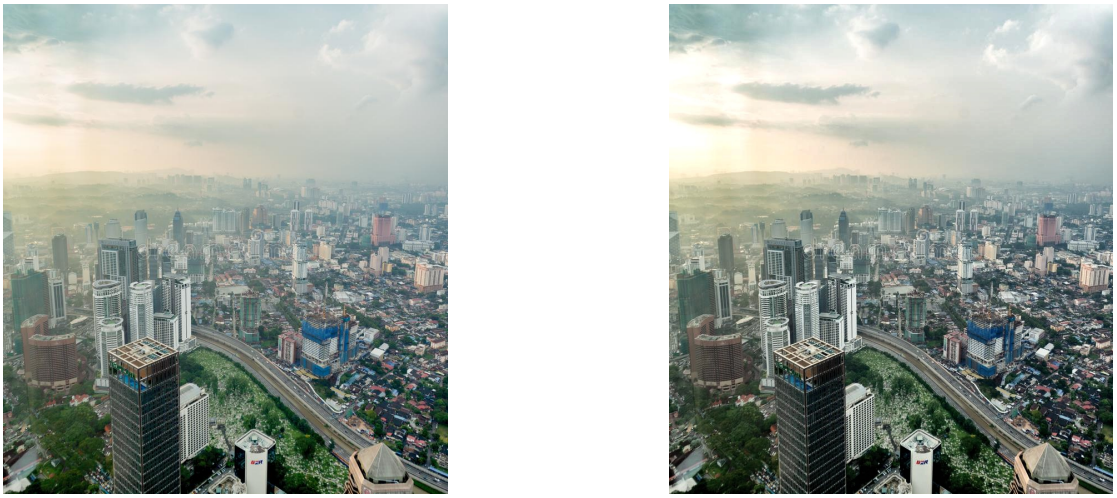

FIGURE 4.9: Urban scene with CLAHE and gamma correction

4.5 Experimental Results

4.5.1 Qualitative Comparison

Figure **??** presents the qualitative evaluation of the proposed method on the HSTS dataset. The top section of the figure demonstrates that our approach effectively preserves the true colors of the original image while enhancing its overall quality and brightness, making it more visually appealing to the human eye. In contrast, methods based on dark channel prior, transmission estimation, and their respective outputs tend to over-emphasize the sky regions. While the results from CAP are comparable to ours, our method achieves colors that are more closely aligned with the ground truth.

4.5.2 Quantitative Comparison

Quantitative performance is assessed using standard metrics such as MSE, PSNR (dB), SSIM, and CORR. Figure **??** presents a comparison using six distinct hazy images. The

IMAGE NO.	SSIM	MSE(dB)	CORR	PSNR(dB)(dB)
1.	0.9871	29.2043	0.9970	33.4763
2.	0.8872	80.0250	0.8238	29.0985
3.	0.9881	17.2575	0.9948	35.7610
4.	0.9900	33.5263	0.9765	32.8769
5.	0.8265	75.0188	0.5039	29.3790
6.	0.9440	68.2038	0.9061	29.7927
7.	0.8922	107.0118	0.9646	27.8364
8.	0.8816	64.5266	0.8894	30.0334
9.	0.9779	19.9921	0.9598	35.1222
10.	0.9955	0.4863	0.9998	51.2616

TABLE 4.12: Quantitative PSNR(dB)/SSIM/CORR/MSE results of proposed approach

	DCP		CAP		This method	
cc	PSNR(dB)	MSE	PSNR(dB)	MSE	PSNR(dB)	MSE
1	27.6906	110.6663	27.5506	82.2099	28.9815	82.2099
2	27.4804	116.1549	28.3516	95.0411	27.6618	111.4025
3	27.8221	107.3649	27.5809	113.4960	28.4485	92.9457
4	27.8227	107.3497	27.2006	123.8851	28.3665	94.7166
5	27.8629	106.3622	28.3155	95.8362	27.9545	104.1428
6	28.0887	100.9725	27.7458	109.2676	27.5674	113.8497

TABLE 4.13: PSNR(dB) and MSE of proposed method vs. DCP, CAP

	DCP		CAP		Proposed method	
cc	CORR	SSIM	CORR	SSIM	CORR	SSIM
1	0.7916	0.4527	0.9322	0.6371	0.9978	0.9627
2	0.9583	0.6080	0.9799	0.6925	0.9989	0.9558
3	0.9049	0.4087	0.9070	0.4479	0.9976	0.9310
4	0.7813	0.6615	0.9257	0.7417	0.9961	0.9612
5	0.9654	0.8074	0.7325	0.3355	0.9978	0.9295
6	0.9378	0.7019	0.4613	0.4198	0.9981	0.9372

TABLE 4.14: CORR and SSIM of proposed method vs. DCP, CAP

evaluation involves four methods—DCP, CAP, Meng, and the proposed approach—based on the data presented in Tables **??**, **??**, and **??**. For each metric, the method yielding the best result is highlighted in red, indicating its superior accuracy or effectiveness.

4.6 Discussion

In this study, I implemented three different methods for image dehazing, focusing on efficiency and image quality. Among these approaches, the Markov Random Field (MRF)-based method demonstrated a relatively faster computation time for generating the transmission coefficient. However, the overall image quality obtained was not satisfactory.

The key contributions of my methods include the introduction of a **parallel processing architecture** to enhance computational efficiency and the integration of **automatic gamma correction** to improve image contrast and visibility. These advancements aim to optimize the dehazing process while balancing computational speed and perceptual quality. Future work will focus on refining transmission estimation techniques to achieve superior dehazing performance without compromising efficiency.

Chapter 5

Night Time Image Dehazing

5.1 Introduction

Dehazing in night-time conditions is a crucial area of research in computer vision and image processing. Unlike daytime dehazing, nighttime scenarios introduce additional complexities due to the presence of artificial lighting, reflections, and increased noise. The present study addresses these challenges by focusing on key aspects such as ambient light estimation, guided filtering, reflection mapping, and advanced image enhancement techniques. These elements collectively contribute to the effective restoration of image clarity and quality in low-light, foggy environments.

Contribution to the Chapter

- This a luminance-aware enhancement strategy specifically designed for nighttime hazy images, addressing excessive brightness that often obscures details.
- Applied gamma mapping to reduce high luminance while preserving image features and improving contrast and visual clarity.
- Developed a luminance estimation model using a weighted combination of RGB channels, tailored for perceptual accuracy.
- Integrated haze removal with luminance mapping through a refined atmospheric light compensation and transmission map adjustment.
- Ensured balanced luminance across all color channels, resulting in visually clearer and more detailed dehazed images under low-light conditions.

In detail, this research explores methods to improve detail preservation and enhance the overall visual appeal of dehazed images through the interaction of atmospheric light modeling, reflection mapping, guided filtering, and luminance adjustment. A critical enhancement in the This framework is the incorporation of the gamma parameter into the tone-mapping process. This addition provides unprecedented control over brightness and contrast adjustments, empowering users with greater artistic and interpretative flexibility.

[0]U. Biswas, **A. Ghosh**, S. Chakraborty and S. S. Chaudhuri, "Power Law-Based Night-Time Image Dehazing Fused with Luminance Mapping for Enhanced Visibility," 2023 7th International Conference on Electronics, Materials Engineering Nano-Technology (IEMENTech), Kolkata, India, 2023, pp. 1-6, doi: 10.1109/IEMENTech60402.2023.10423451. keywords: Photography;Visualization;Filtering;Surveillance;Brightness;Transportation;Reflection;Night time dehazing;real-time;image processing;luminance mapping,

To achieve visually balanced and aesthetically refined dehazed images, the luminance-mapped section dynamically adjusts the luminance of the dehazed output based on tone-mapped luminance values. By harmonizing brightness levels across different color channels, this approach significantly enhances the overall quality of the restored image.

The effectiveness of the This framework is demonstrated through its ability to manage the complexities of poorly lit and foggy environments, making it applicable to various fields such as transportation, outdoor photography, and surveillance. By successfully mitigating nighttime visibility issues, this study highlights the transformative potential of interdisciplinary collaboration and technological advancements in reshaping how I perceive and interact with the surroundings in low-light conditions.

5.2 Nighttime Haze Model and Image Enhancement Techniques

The nighttime haze model accounts for complex illumination conditions such as artificial light sources and low ambient visibility. It aims to accurately represent light scattering and glow effects unique to night scenes

5.2.1 Nighttime Haze Model

This study introduces a nighttime haze model that accounts for varying artificial light sources and their glow, which significantly differs from daytime haze models. Traditional daytime haze models assume a single, consistent, and often invisible light source. However, nighttime images frequently contain multiple distinguishable light sources in various colors, each contributing to a visible glow effect that is absent in daylight haze.

As illustrated in Figure 5.1, rather than relying solely on atmospheric light, the airlight in the nighttime haze model derives energy from active light sources. These sources not only illuminate the scene but also contribute to a unique glow effect, making them visually distinct from other objects. The model, as described by Yu Li, Robby T. Tan, and Michael S. Brown (76), incorporates a glow component into the modified haze equation:

$$I(x) = R(x)t(x) + L(x)(1 - t(x)) + La(x) \cdot APSF \tag{5.1}$$

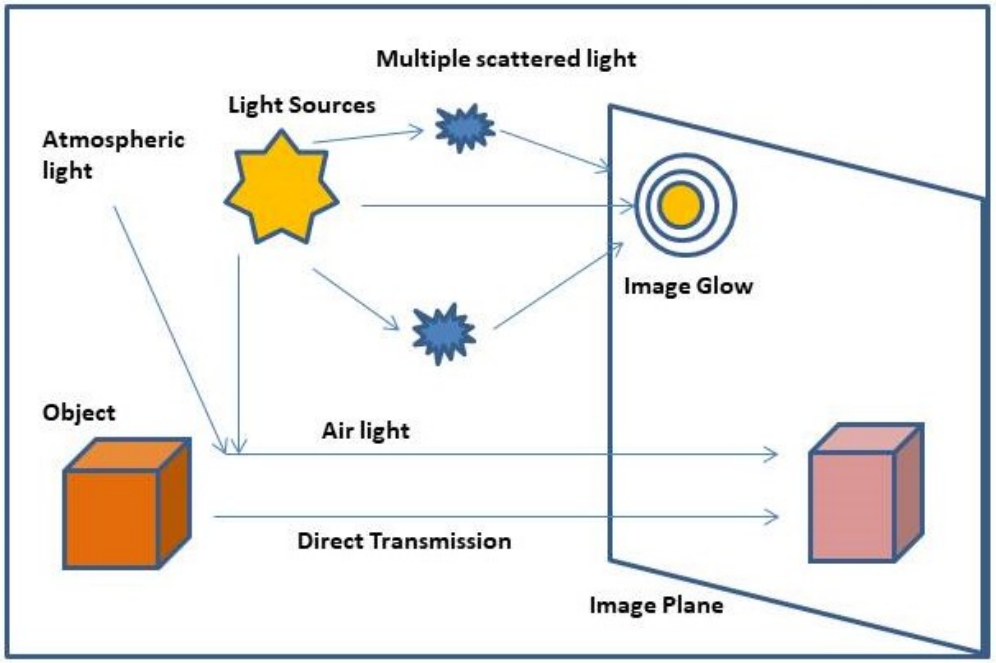

FIGURE 5.1: The nighttime haze model

Here, $I(x)$ is the observed intensity, $R(x)$ represents the recovered scene intensity, and $L(x)$ denotes the global atmospheric light. The term $t(x)$ is the medium transmission that describes the fraction of light reaching the camera without scattering. The product $R(x) \cdot t(x)$ corresponds to the direct attenuation, while $L(x) \cdot (1 - t(x))$ accounts for the airlight component. Additionally, the glow effect present in nighttime images is modeled by the Atmospheric Point Spread Function (APSF).

5.2.2 Key Image Enhancement Techniques

5.2.2.1 Guided Filtering

Guided filtering is an image-processing technique that enhances an image using a reference, known as the *guidance image*. It is particularly effective in applications requiring edge preservation, such as *dehazing, tone mapping, and edge-aware smoothing*. Unlike conventional filters like the bilateral filter, guided filtering maintains fine details while smoothing uniform regions, making it suitable for haze removal and contrast enhancement.

5.2.2.2 Reflectance Mapping

Reflectance mapping is commonly used in computer graphics to simulate how light interacts with reflective surfaces, improving the realism of rendered scenes. In *foggy or hazy conditions*, a reflectance map helps in adjusting the light reflection properties of different objects in an image. By analyzing and enhancing surface reflectivity, reflectance mapping improves image quality, restoring fine details lost due to haze.

5.2.3 Estimating Atmospheric Light and Transmission

Atmospheric light refers to the scattered or reflected light that reaches the camera due to haze. The presence of haze reduces transmitted light, causing distant objects to appear *brighter but less distinct*. To accurately reconstruct a haze-free image, it is essential to estimate both atmospheric light and transmission.

- The *getAtmosphere* method determines atmospheric light from a hazy input image, enhancing its brightness component using guided filtering.
- Atmospheric light is estimated *individually* for the three color channels (Red, Green, and Blue) to improve accuracy.
- The *transmission map* models light attenuation through haze, where lower transmission values indicate heavier haze and reduced visibility.

The *getTransmission* method estimates transmission by converting the image to the *HSV color space* and computing transmission values based on grayscale Laplacian and color channel properties. The transmission value t is computed using:

$$t = 0.84 - (0.6342 \cdot h) \tag{5.2}$$

$$h = \exp(-2.7563 \cdot g^2 - 0.6567 \cdot (1 - b)^2 - 3.3801 \cdot s^2) \tag{5.3}$$

Here, s denotes the saturation, b represents the brightness, and g refers to the grayscale Laplacian of the haze-free image.

Accurate estimation of **atmospheric light and transmission** is critical for effective dehazing, ensuring *natural color restoration and improved visibility* in processed images.



FIGURE 5.2: Reflectance mapping and Atmospheric Light & Transmission Estimation

This framework successfully *enhances nighttime images* by addressing key challenges such as *light source variation, glow effects, and haze attenuation*, making it applicable to **surveillance, transportation, and outdoor photography**.

5.3 This Method

5.3.1 Gamma Mapping for Luminance Reduction

Luminance refers to an image's perceived brightness, impacting visibility and contrast. In nighttime images, excessive luminance can obscure details. The This method reduces high luminance using gamma mapping, adjusting brightness while preserving image details.



FIGURE 5.3: Nighttime hazy image with high luminance

Luminance (Y) is computed using weighted color channels:

$$Y = 0.2126R + 0.7152G + 0.0722B \tag{5.4}$$

To enhance details and improve visual quality, gamma mapping modifies luminance as:

$$luminance_{\text{mapped}} = luminance^{(1/\gamma)} \tag{5.5}$$

where γ controls contrast adjustment.

5.3.2 Luminance and Lower Luminance Mapping

The *HazeFree* function enhances the dehazed image (I_{cap}) by estimating luminance and applying gamma correction:

$$luminance = xI_{\text{cap}}[:,:,0] + yI_{\text{cap}}[:,:,1] + zI_{\text{cap}}[:,:,2] \tag{5.6}$$

where $x = 0.2126$, $y = 0.7152$, and $z = 0.0722$. The adjusted image is computed as:

$$res[:,:,ind] = \frac{(I_{\text{cap}}[:,:,ind] - L_2[:,:,ind](1-t))}{\max(t, tx)} + L_2[:,:,ind] \tag{5.7}$$

where L_2 is the refined atmospheric image, t is the transmission map, and tx is a small constant. The final luminance is adjusted as:

$$res = res + (luminance_{\text{mapped}} - res_{\text{lum}})[:,:,\text{None}] \tag{5.8}$$

This process ensures balanced luminance across all color channels.



FIGURE 5.4: Luminance mapping using gamma correction

5.4 Experimental Results

5.4.1 Qualitative Comparison

The method effectively enhances nighttime images by adjusting luminance while preserving natural colors and improving visibility. The process was implemented in Google Colab using Python libraries on a Dell laptop.

TABLE 5.1: PSNR of This method vs. DCP, Histogram Equalization(H.E.), and Zhang's method

Image No.	DCP(18)	H.E.	Zhang (77)	This Method
1	29.95 dB	27.78 dB	27.50 dB	36.51 dB
2	28.59 dB	28.11 dB	27.63 dB	32.42 dB
3	29.83 dB	28.77 dB	27.56 dB	36.12 dB
4	28.44 dB	28.23 dB	27.39 dB	35.37 dB
5	28.30 dB	27.86 dB	27.51 dB	32.62 dB
6	28.99 dB	27.42 dB	28.69 dB	32.86 dB
7	30.18 dB	28.04 dB	27.39 dB	41.46 dB
8	27.53 dB	27.88 dB	27.44 dB	31.85 dB
9	27.67 dB	27.78 dB	28.27 dB	29.08 dB
10	27.54 dB	28.03 dB	29.55 dB	30.36 dB

5.5 Discussion:

The significance of nighttime dehazing in computer vision and image processing is undeniable. By focusing on key elements such as ambient light estimation, guided filtering, reflection mapping, and image enhancement, this study achieves significant improvements in clarity, contrast, and detail preservation for images captured in low-light and foggy conditions. The integration of atmospheric light modeling, luminance mapping,

TABLE 5.2: MSE of This method vs. DCP, Histogram Equalization(H.E.), and Zhang's method

Image No.	DCP(18)	H.E.	Zhang (77)	This Method
1	65.8410	108.5341	115.5552	14.5141
2	90.0279	100.4369	112.2066	37.2367
3	67.6694	86.2627	114.0369	15.9030
4	93.0616	97.8104	118.5231	18.8781
5	96.1704	106.3270	115.3569	35.5789
6	81.9960	117.8449	87.9823	33.6512
7	62.3606	102.1159	118.6791	4.6509
8	114.7643	106.0144	117.3651	42.4774
9	111.0727	108.4321	96.9081	80.4253
10	114.5128	102.3943	72.1629	59.8862

TABLE 5.3: SSIM of This method vs. DCP, Histogram Equalization(H.E.), and Zhang's method

Image No.	DCP(18)	H.E.	Zhang (77)	This Method
1	0.8876	0.8091	0.7849	0.9966
2	0.6680	0.5044	0.7709	0.9842
3	0.7210	0.5810	0.7172	0.9922
4	0.3355	0.4035	0.6929	0.9869
5	0.3768	0.8335	0.6739	0.9862
6	0.2743	0.4280	0.7455	0.9704
7	0.8594	0.4342	0.7655	0.9917
8	0.6802	0.6409	0.7564	0.9887
9	0.1400	0.7032	0.7576	0.9455
10	0.0711	0.3804	0.8434	0.9285

TABLE 5.4: CORR of This method vs. DCP, Histogram Equalization(H.E.), and Zhang's method

Image No.	DCP(18)	H.E.	Zhang(77)	This Method
1	0.9089	0.9018	0.9248	0.9962
2	0.5965	0.8297	0.9305	0.9819
3	0.7477	0.8435	0.9557	0.9974
4	0.5956	0.8205	0.9543	0.9961
5	0.4011	0.9576	0.9373	0.9925
6	0.4333	0.9048	0.9597	0.9919
7	0.7530	0.7682	0.9339	0.9899
8	0.4602	0.9065	0.7949	0.9804
9	0.4164	0.9513	0.9291	0.9684
10	0.5498	0.8766	0.9824	0.9877

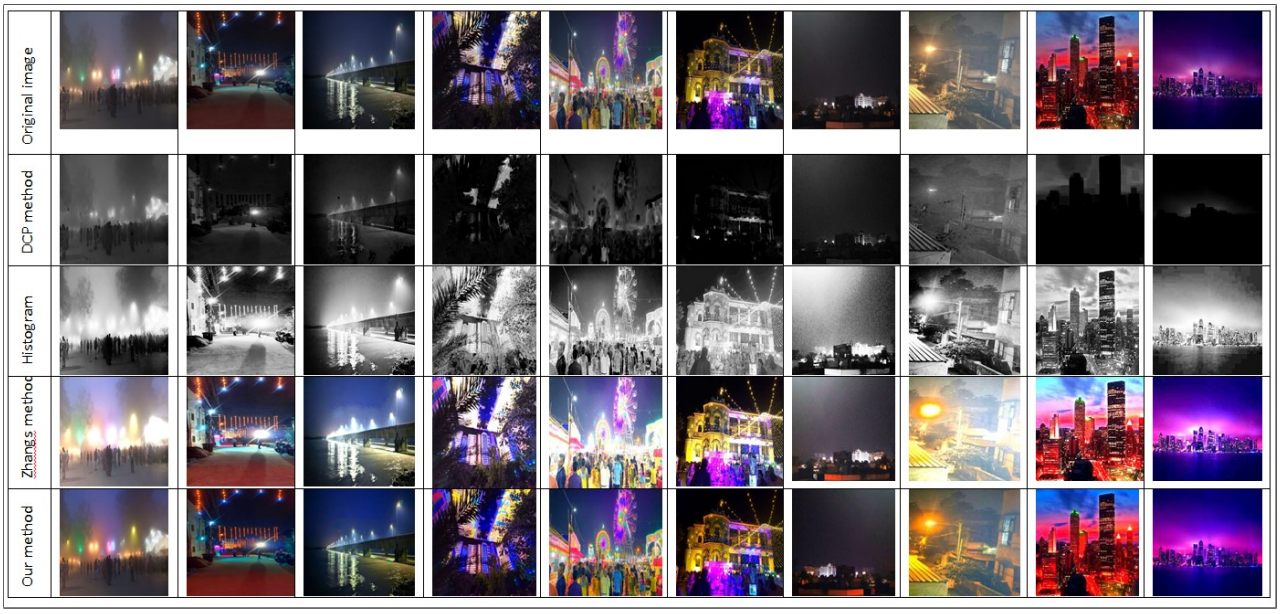

FIGURE 5.5: Qualitative results input images. Upper half: comparison to dark channel prior-based methods; middle half:histogram eqalization and Zhangs method ,bottom half: This apporoch of the nighttime images

and lower luminance mapping further enhances the visual appeal of dehazed images. Additionally, incorporating the gamma parameter into tone mapping provides greater flexibility in brightness and contrast adjustments, enabling more refined image enhancements. The This framework effectively addresses the challenges posed by low-light and foggy environments, making it beneficial for applications in transportation, outdoor photography, and security. This study contributes to advancing image perception in nighttime conditions by offering a comprehensive dehazing approach, demonstrating how the synergy of multiple enhancement techniques can significantly improve visibility. The findings highlight how technological advancements in image processing can transform this understanding and interaction with nocturnal environments.

Chapter 6

Deep Learning Approach for Time invariant Image Dehazing

6.1 Introduction

Images play a vital role in the functionality of computer vision and artificial intelligence systems. However, the presence of atmospheric suspended particles causes light rays to refract, reflect, and scatter, leading to image degradation and loss of crucial visual information during acquisition. The process of image acquisition can be impacted, often leading to a loss of image information. Consequently, this loss results in decreased brightness, contrast, and visibility of the acquired image, thereby affecting the performance of computer vision applications that rely on these images as input.



FIGURE 6.1: Illustration of the same scene captured during nighttime and daytime, highlighting variations in light scattering and visibility under different illumination conditions.

Fig. 6.1: Illustration of the same scene captured during nighttime and daytime, demonstrating the distinct effects of illumination on visibility and atmospheric scattering. The daytime image shows stronger ambient light, resulting in clearer object contours and reduced signal noise. In contrast, the nighttime image exhibits diminished illumination, increased scattering from artificial light sources, and reduced detail visibility. Together, these observations highlight how varying lighting conditions significantly influence scene appearance and challenge traditional image restoration and enhancement methods.

Image dehazing techniques can be broadly classified into two categories based on lighting conditions: daytime and nighttime dehazing. During the day, the sky exhibits high brightness and contrast, appearing vividly blue, whereas at night, the sky turns completely dark, with localized artificial light sources creating variations in color distribution across images of the same scene. Despite the distinct challenges posed by these different

[0]A. Ali, **A. Ghosh**, and S. S. Chaudhuri titled **"LIDN: A Novel Light Invariant Image Dehazing Network"** published in Engineering Applications of Artificial Intelligence in 2023 (https://doi.org/10.1016/j.engappai.2023.106830).

conditions, research on dehazing techniques for both daytime and nighttime scenarios remains relatively limited.

6.2 Contributions

The key contributions of this chapter are summarized as follows:

- A single deep learning model for dehazing images in the day and at night. Feature Extractor, Medium Transmission Extraction Network (MTEN), Deep Global Atmospheric Light Estimator (DGALE), and an encoder-decoder module are the four sub-modules that make up the suggested dehazing network, Light Invariant Image Dehazing Network (LIDN). This framework's usefulness is shown in a variety of settings.
- Improved inference speed compared to existing models while maintaining superior qualitative results.
- Introduction of the Quadruplet Loss function to train LIDN, enhancing dehazed image sharpness and effectively reducing artifacts.

6.3 Background

The representation of hazy pictures proposed by H. Koscmeiders(78) is as follows.

$$I(x) = J(x)t(x) + \alpha(1 - t(x)) \tag{6.1}$$

where $t(x)$ indicates the transmission coefficient, α indicates the atmospheric light, $I(x)$ indicates the hazy image, and $J(x)$ indicates the haze-free image. It is clear from analyzing Equation 6.1 that the hazy image $I(x)$ is the only term that is known, while the other terms are unknown. Therefore, there are three processes involved in determining the three parameters. There are two steps involved in calculating atmospheric light (α): (18) introduced the dark channel calculation, which was followed by the atmospheric light calculation. The preceding equation for the dark channel is shown as

$$I^{dark}(x) = \min_{y \in \Omega(x)} (\min(I^C(y))) \tag{6.2}$$

where C stands for each color channel in Red, Green, Blue and $\Omega(x)$ is a minimum intensity square kernel at x. The shaded portion of the entire image is represented by a

dark channel, while atmospheric light (α) is represented by 0.1% of the dark channels' brightest pixels. The transmission coefficient in this model, which assumed homogeneous haze, is shown as -

$$t(x) = e^{-\beta d(x)} \tag{6.3}$$

Considering the aerial perspective, the transmission coefficient is adjusted using w, a constant parameter ($0 < w \leq 1$) that varies depending on the specific application, and is represented as follows: where β and $t(x)$ represent the scattering coefficients of the atmosphere and scene depth, respectively. This expression clearly illustrates the attenuation of haze as a function of distance d.

$$t(x) = 1 - w * \min_{y \in \Omega(x)} (\min_{C \in r,g,b} \frac{I^c(y)}{\alpha^c}) \tag{6.4}$$

Consequently, the scene is recovered using the following equation after the ambient light and transmission coefficient have been determined.

$$J(x) = \frac{(I(x) - \alpha)}{max\{t(x), t_0\}} + \alpha \tag{6.5}$$

where the recovered haze-free scene is represented by $J(x)$, guaranteeing a lower limit for the transmission coefficient to enable precise scene recovery. In order to avoid division by zero in the transmission coefficient computation, t_0 is also inserted as a lower bound. The classic H. Koschmieder equation for image dehazing is used to create the suggested deep learning model, LIDN.

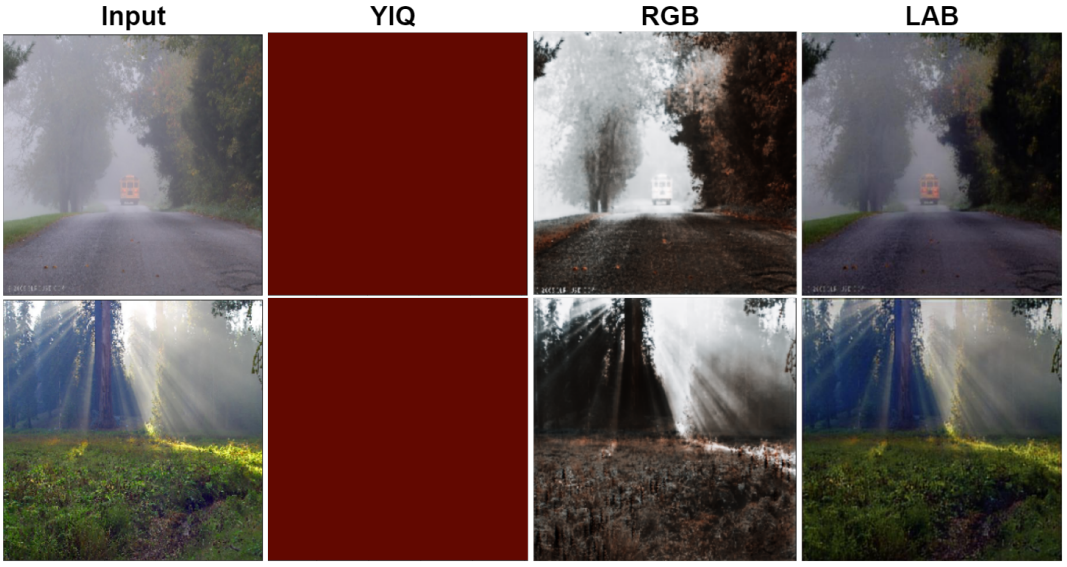

FIGURE 6.2: Output of the proposed model train in YIQ, RGB and LAB color space, where in LAB color space the proposed model shows best results.

6.4 Proposed Method

The suggested model architecture is presented in this part along with a summary of the training procedure and an explanation of how it relates to conventional approaches. Based on an end-to-end deep encoder-decoder dehazing framework, the method produces a dehazed image as its output after receiving a hazy image as input.

TABLE 6.1: Configuration Details of the Deep Global Atmospheric Light Estimator Network

Type	Input Size	Number of Filters	Filter Size	Stride
Convolution + ReLU + Instance Norm +Max Pooling	(224,224,1)	8	(3,3)	1
	(224,224,8)	16	(3,3)	1
	(112,112,16)	32	(3,3)	1
	(56,56,32)	64	(3,3)	1
	(28,28,64)	128	(3,3)	1
	(14,14,128)	256	(3,3)	1
	(7,7,256)	512	(7,7)	1
Flatten	(1,1,512)	-	-	-
Fully connected	512	-	-	-
	256	-	-	-
	128	-	-	-
	1	-	-	-
SoftMax	1	-	-	-

6.4.1 Data Pre-processing

There are three steps in the pre-processing stage. First, each channel is normalized before blurry images are transformed from the RGB to the LAB color space. The HSV color space is then created from the RGB image. Lastly, the following formula is used to calculate the haze maps $d_1(x)$ and $d_2(x)$:

$$d_1(x) = \theta_0 + \theta_1 V(x) + \theta_2 S(x) + p(x|\mu, \sigma^2) \tag{6.6}$$

A model that has been trained on 500 samples, totaling 120 million scene points, is proposed by Q. Zhu et al. (19). Fixed values for θ_0, θ_1, and θ_2 yield optimal learning outcomes; in particular, $\theta_0 = 0.121779$, $\theta_1 = 0.959710$, and $\theta_2 = 0.780245$, with mean $\mu = 0$ and standard deviation $\sigma = 0.041337$ (19). Notably, any changes in θ have an immediate effect on the depth map, either causing artifacts or lowering the quality of the images during the dehazing process.

$$d_2(x) = S(x) - V(x) \tag{6.7}$$

In the *HSV color space*, the function $S(x)$ indicates the *saturation component*, and $V(x)$ indicates the *value component* of the input image. The model uses two *haze maps* and the *LAB hazy image* as input in the last processing step.

During training, *ground truth RGB images* are *normalized* within the [0.0, 1.0] range. However, when the network is trained using input images in *RGB and YIQ color spaces*, the dehazing performance is notably reduced, as illustrated in Figure 6.2. This discrepancy arises due to the *differences between the LAB and RGB models*, with the *LAB model* exhibiting greater alignment with human visual perception. As demonstrated by (79), models incorporating *human-like color perception* achieve superior performance in the *LAB color space*, highlighting the necessity of *pre-processing* for this network.

Figure 6.2 illustrates the dehazing results across different color spaces, confirming that the *LAB color space delivers the best performance.*

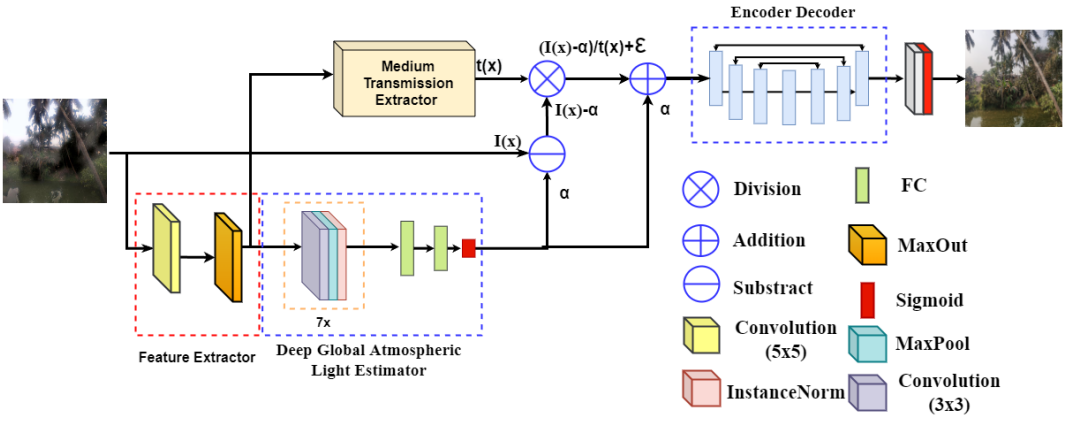

FIGURE 6.3: The overall framework of the proposed LIDN method. The network consists of four sub-blocks Feature Extractor, Medium Transmission Extraction, Deep Global Atmospheric Light Estimator and Encoder Decoder head.

6.4.2 Model Architecture

In the *HSV color space*, the function $S(x)$ indicates the *saturation component*, and $V(x)$ indicates the *value component* of the input image. The model uses two *haze maps* and the *LAB hazy image* as input in the last processing step. In the *HSV color space*, the function $S(x)$ indicates the *saturation component*, and $V(x)$ indicates the *value component* of the input image. The model uses two *haze maps* and the *LAB hazy image* as input in the last processing step.

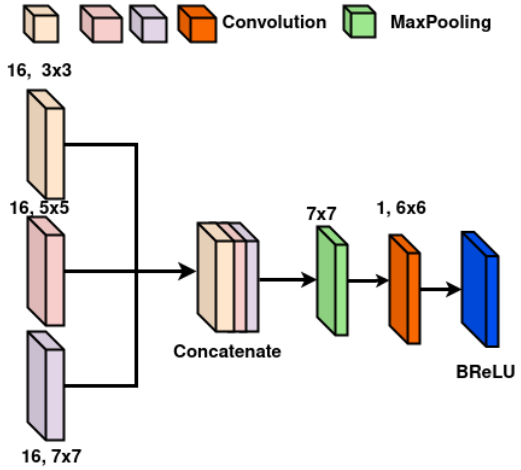

FIGURE 6.4: Structural Representation of the Medium Transmission Extractor with Feature Map Annotations.

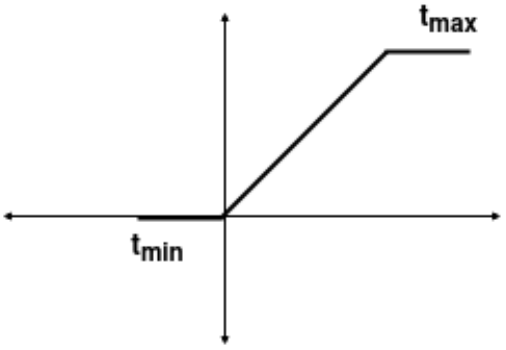

FIGURE 6.5: BReLU Activation Function: Representation of Maximum and Minimum Transmission in Dehazing

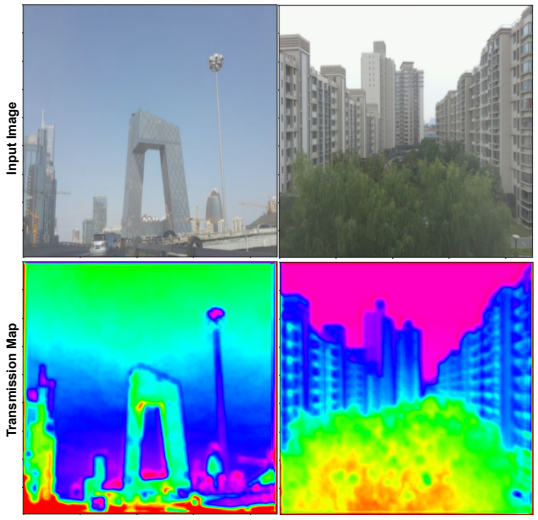

FIGURE 6.6: Extracted Transmission Map $t(x)$ from the Medium Transmission Extractor

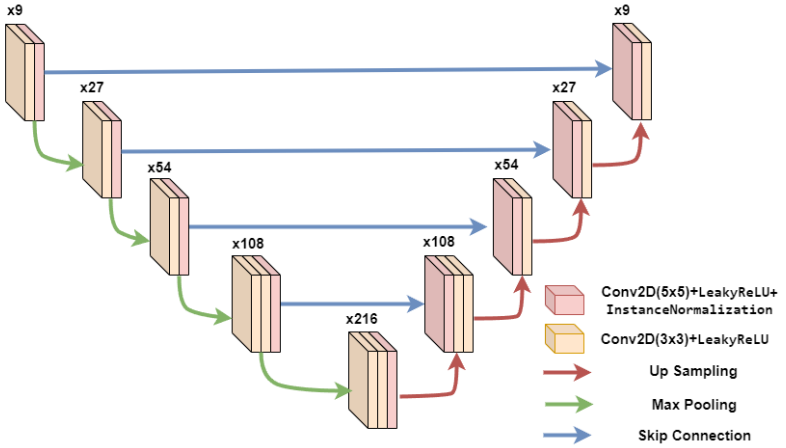

FIGURE 6.7: Schematic Representation of the Encoder-Decoder Architecture: Feature Maps Indicated in Boxes with Channel Count Annotated on Top, and Operations Depicted via Arrows

6.4.2.1 Feature Extraction Layer

The initial stage of the proposed architecture is designed to derive haze-relevant features such as dark channel priors, hue variance, and color attenuation. A pre-processed five-channel image is passed through a convolutional layer composed of sixteen filters of size 5×5, which learn to identify these haze characteristics. To emphasize the most relevant features for haze removal, a MaxOut unit is employed, selecting the most significant responses. The mathematical representation of this operation is given as:

$$F^l_{i,j,k} = W^l_{i,j} \circledast I_{i,j,k} \tag{6.8}$$

$$F^l_{i,j,g} = \max_x F^l_{i,j,g,k\|g} \tag{6.9}$$

Here, $W^l_{i,j}$ represents the lth learned kernel, $\circledast$ indicates the convolution operation, and I is the input tensor. The MaxOut mechanism segments the last dimension of the feature map into groups g, assuming k is divisible by g, and then performs a max operation across each group. The symbol "$\|$" denotes integer division. Inspired by the method introduced in (80), the feature extraction mechanism incorporates non-linear transformations via MaxOut to isolate haze-related features effectively, as further elaborated in (81).

6.4.2.2 Medium Transmission Estimation

To effectively restore a haze-degraded image using Equation 6.1, two critical components—medium transmission $\hat{t}(x)$ and global atmospheric light ($\hat{\alpha}$)—must be estimated.

The medium transmission map $\hat{t}(x)$ is predicted using a dedicated Medium Transmission Estimation Network (MTEN), as depicted in Figure 6.4. MTEN processes the output from the feature extractor $F^l_{i,j,g}$ using three parallel convolutional branches, each using different kernel sizes: 3×3, 5×5, and 7×7, each with 16 filters. This multi-branch design captures diverse spatial contexts and object depths. The operation is defined as:

$$ {}^{p}F^t_{i,j,k} = {}^{p}W^t_{i,j,k} \circledast F^l_{i,j,k} \tag{6.10} $$

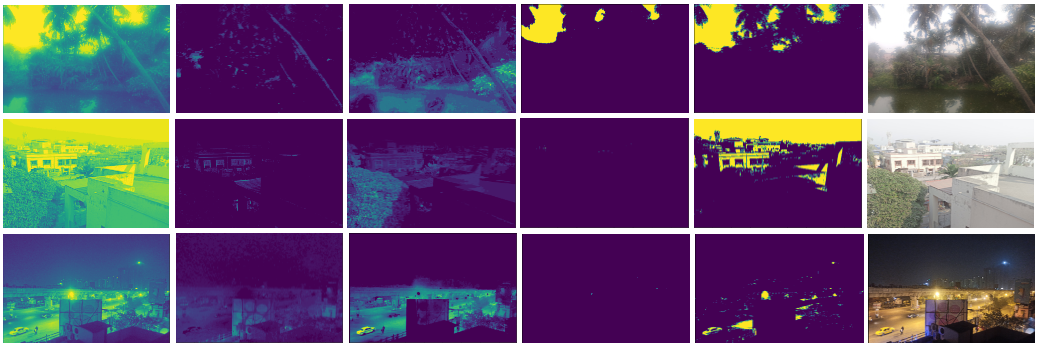

FIGURE 6.8: Haze-relevant feature maps extracted under varying lighting conditions as computed by Equation 6.15. The right side illustrates the network inputs.

Here, the superscript p identifies the respective parallel convolution path, and ${}^{p}W^t_{i,j,k}$ are the learnable weights in each branch. The resulting feature maps are concatenated along the depth dimension, as given by:

$$ F^t_{i,j,3k} = [{}^{1}F^t_{i,j,k}, {}^{2}F^t_{i,j,k}, {}^{3}F^t_{i,j,k}] \tag{6.11} $$

This stacked tensor is then processed by a 7×7 max-pooling layer with stride 1 and padding 6, followed by a convolution layer using 6×6 filters and stride 1:

$$ F^t_{i,j,3k} = {}^{p}W^t_{i,j,k} \circledast F^t_{i,j,3k} \tag{6.12} $$

The final layer of the MTEN employs the Bilateral Rectified Linear Unit (BReLU) as the activation function, defined as:

$$ \hat{t}(x) = \mathrm{BReLU}(F^t_{i,j,3k}) \tag{6.13} $$

BReLU, introduced by (20), merges the properties of ReLU and Sigmoid to suit haze removal tasks. Unlike ReLU, which can suffer from vanishing gradients, BReLU operates within a bounded range, making it more stable for such applications. In this work, the BReLU is parameterized with $t_{\min} = 0$ and $t_{\max} = 1$, implemented effectively by applying a Sigmoid function followed by ReLU. The estimated transmission map $\hat{t}(x)$, as shown in Figure 6.6, demonstrates that the proposed LIDN model accurately captures the structural details of the scene.

6.4.2.3 Global Atmospheric Light Estimation Using Deep Networks

The estimation of global atmospheric light is performed using an unsupervised learning module called the Deep Global Atmospheric Light Estimator (DGALE). This module comprises seven deep convolutional layers, each followed by instance normalization. A max-pooling operation with a 2×2 kernel and stride of 2 is employed to reduce the spatial dimensions. Convolution layers use 3×3 filters to preserve fine-grained local details within a compact receptive field. Subsequently, three fully connected layers are appended to predict the atmospheric light vector. ReLU activation is applied after each layer to incorporate non-linearity and improve the generalization capacity of the network. The design architecture of DGALE is summarized in Table 6.1. A Softmax activation is applied at the final layer to ensure normalized output. The estimated global atmospheric light is given by:

$$\hat{\alpha} = DGALE(F^{l}_{i,j,g}) \tag{6.14}$$

6.4.2.4 Encoder-Decoder Integration Layer

The final stage of the dehazing pipeline is the Encoder-Decoder Head, which integrates outputs from the MTEN and DGALE modules. The classic haze removal equation is adapted to combine these modules as:

$$J(x) = \frac{I(x) - \hat{\alpha}}{\hat{t}(x) + \epsilon} + \hat{\alpha} \tag{6.15}$$

Here, ϵ is a small constant added to prevent division by zero. This adjusted formulation merges the estimated transmission map $\hat{t}(x)$ and global atmospheric light $\hat{\alpha}$ to produce a combined representation, as visualized in Figure 6.8. The rightmost images in the figure

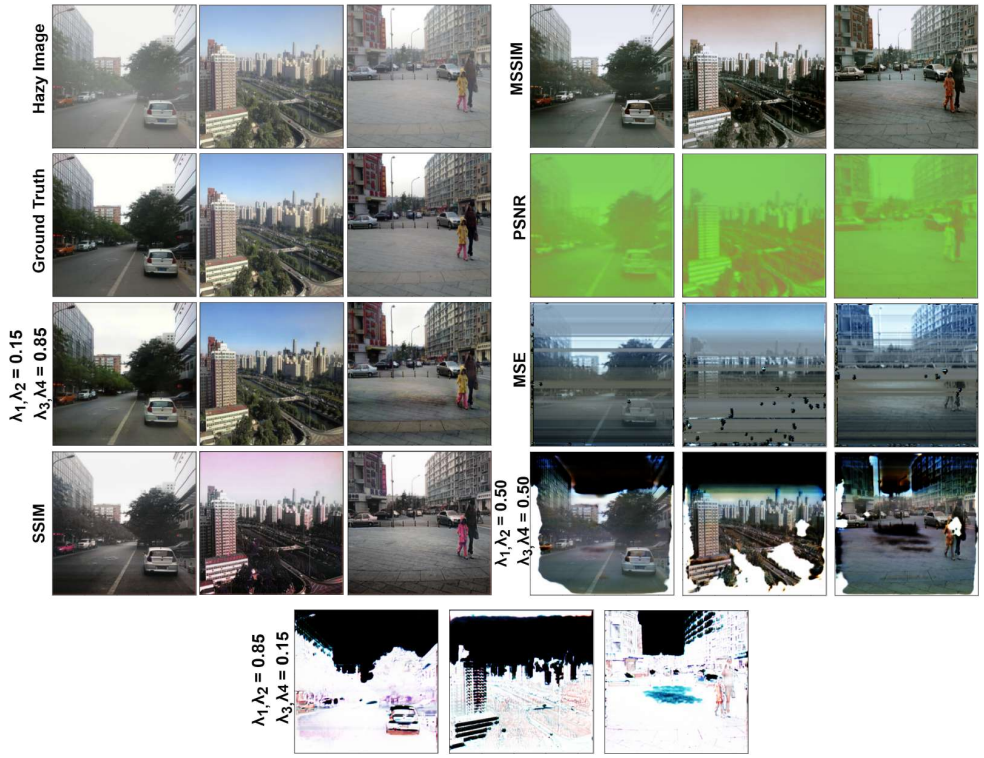

FIGURE 6.9: Results of dehazing with the proposed LIDN architecture using MSSIM, PSNR, SSIM, MSE, and Quadruplet Loss under various λ configurations.

show the input, while the remaining images illustrate varying feature maps conditioned on lighting and haze density.

Unlike traditional dehazing methods that use Equation 6.15 to directly derive the haze-free image, this framework leverages it to merge feature maps from the MTEN and DGALE modules. The output is then passed through an encoder-decoder neural block, generating the following intermediate representation:

$$F_{i,j,k}^{EDN} = EDN(J(x)) \tag{6.16}$$

This output is subsequently refined using a convolutional layer followed by a Sigmoid activation function, constraining the pixel values between 0 and 1, as shown in Figure 6.3. The final dehazed output is:

$$O(x) = \text{Sigmoid}(W_{i,j,k}^{F} \circledast F_{i,j,k}^{EDN}) \tag{6.17}$$

The DGALE and MTEN components collaborate to tackle varying haze intensities in both daytime and nighttime conditions. DGALE focuses on capturing the scene's ambient illumination, which is normalized between 0 and 1 using Sigmoid activation to stabilize training. The Transmission Coefficient Estimator processes a five-channel LAB input image augmented with two haze maps, as described in subsection 6.4.1. This comprehensive input helps generate accurate transmission maps, demonstrated in Figure 6.6. The encoder-decoder structure at the end further refines the output from Equation 6.15, enhancing dehazing performance across diverse visual scenarios.

6.4.3 Model Training Procedure

This section outlines the datasets employed for training and evaluation, the chosen loss functions, and the hyperparameter configuration used for training the LIDN architecture.

6.4.3.1 Datasets for Training and Evaluation

To train the proposed dehazing network, several benchmark datasets were utilized: I-HAZE (82), O-HAZE (83), NH-HAZE (84), and DENSE-HAZE (85). Each of these datasets provides high-resolution hazy images along with their corresponding haze-free ground truth counterparts. I-HAZE comprises 35 indoor image pairs, O-HAZE contains 45 outdoor real-world hazy and haze-free image pairs, NH-HAZE includes 55 pairs with non-uniform synthetic haze, and DENSE-HAZE consists of 33 outdoor image pairs with realistic haze effects.

For nighttime dehazing, the N-HAZE dataset was used, which provides 10 image pairs containing synthetic nighttime haze and corresponding ground truth. A total of 150 image pairs were randomly selected from all mentioned datasets for training, and 28 pairs were used for validation.

To expand the dataset, image augmentation techniques such as random flipping, rotation, cropping, and 25% random zooming were applied. The high-resolution images were cropped to 448×448 pixels, resulting in 5000 augmented samples for training and 1000 for validation.

Model robustness was evaluated using the Daytime and Nighttime Dehazing Benchmarking Database (86), which includes 16 images representing various lighting and haze conditions. Additionally, 12,000 images were randomly selected from the RESIDE-Full

dataset (3) to train the model over 25 epochs. Evaluation was performed on SOTS-indoor, OTS-outdoor, OTS-mix, I-HAZE, O-HAZE, DENSE-HAZE, and NH-HAZE datasets.

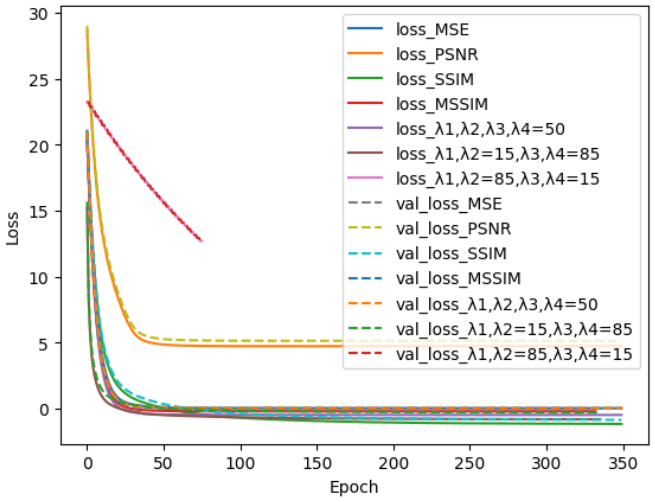

FIGURE 6.10: Training and validation loss curve for the LIDN model across LAB, RGB, and YIQ color spaces.

6.4.3.2 Loss Function Strategy

To enhance the learning performance of the LIDN network, a combination of four complementary loss functions was employed:

- **Mean Squared Error (MSE)(87):** A standard metric in image restoration, MSE evaluates the average squared difference between predicted and target pixels across RGB channels:

$$\mathcal{L}_{MSE} = \frac{1}{N} \sum_{x \in (r,g,b)} (I(x) - O(x))^2 \tag{6.18}$$

where $I(x)$ and $O(x)$ denote the ground truth and predicted pixel values, respectively. N is the total number of images. Its gradient is given by:

$$\frac{\partial \mathcal{L}_{MSE}}{\partial I(y)} = \frac{-2}{N} \sum_{x \in (r,g,b)} (I(x) - O(x)) \tag{6.19}$$

While effective, MSE can introduce undesired blurring in output images.

- **Peak Signal-to-Noise Ratio (PSNR)(88):** To enhance sharpness and reduce noise, PSNR was incorporated:

$$PSNR = 10 \log_{10} \left(\frac{I_{max}^2}{MSE} \right) \tag{6.20}$$

Assuming $I_{max} = 1$ for normalized images, the loss is defined as:

$$\mathcal{L}_{PSNR} = -1 \times PSNR \tag{6.21}$$

Its gradient is expressed as:

$$\frac{\partial \mathcal{L}_{PSNR}}{\partial I(y)} = \frac{20 \ln 10}{N \sum_{x \in (r,g,b)} (I(x) - O(x))} \tag{6.22}$$

- **Structural Similarity Index Measure (SSIM)(89):** SSIM evaluates image similarity in terms of luminance, contrast, and structure:

$$SSIM = \frac{(2\mu_I \mu_O + C_1)(2\sigma_{IO} + C_2)}{(\mu_I^2 + \mu_O^2 + C_1)(\sigma_I^2 + \sigma_O^2 + C_2)} \tag{6.23}$$

where μ_I, μ_O are the means, σ_I^2, σ_O^2 are the variances, and σ_{IO} is the covariance between I and O. Constants C_1, C_2 stabilize the division. SSIM is often decomposed as:

$$SSIM = l(x) \cdot cs(x) \tag{6.24}$$

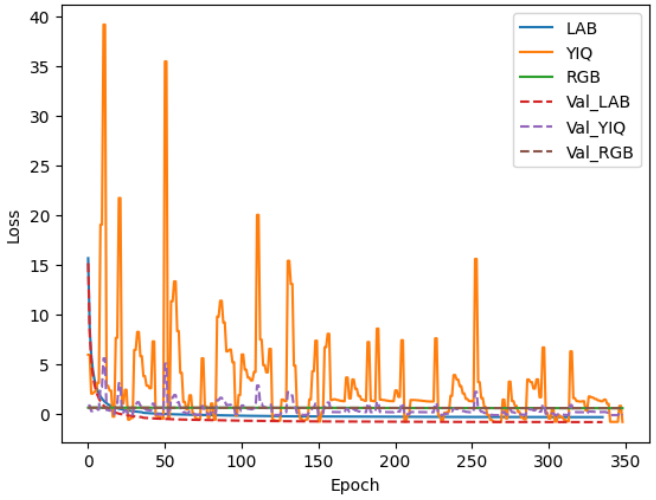

FIGURE 6.11: Training and validation loss curves for LIDN, trained using multiple loss functions including MSE, PSNR, SSIM, MSSIM, and Quadruplet Loss for different λ configurations.

The below equation describes the SSIM -

$$\mathcal{L}_{SSIM} = -1 \times SSIM = -1 \times l(x) \times cs(x) \tag{6.25}$$

Now, the gradient of the SSIM loss is,

$$\frac{\partial \mathcal{L}_{SSIM}}{\partial I(y)} = cs(x)\frac{\partial l(x)}{\partial I(y)} + l(x)\frac{\partial cs(x)}{\partial I(y)} \tag{6.26}$$

where,

$$\frac{\partial l(x)}{\partial I(y)} = 2.G_\sigma(y-x)\frac{(\mu_O - \mu_I l(x))}{(\mu_I^2 + \mu_O^2 + C_1)} \tag{6.27}$$

and,

$$\frac{\partial cs(x)}{\partial I(y)} = \frac{2}{(\sigma_I^2 + \sigma_O^2 + C_2)}.G_\sigma(y-x).[(O(y) - \mu_O) - cs(x)(I(y) - \mu_I)] \tag{6.28}$$

where G_σ is Gaussian kernel of standard deviation σ.

Multi-Scale Structural Similarity Index Measure (MS-SSIM) (42): MS-SSIM is a variant of the SSIM loss function designed to minimize artifacts generated by alternative loss functions. Within a dyadic pyramid structure containing M levels, MS-SSIM is expressed as:

$$MS\text{-}SSIM = l_M^\alpha(x)\prod_{i=1}^{M} cs_j^{\beta_j}(x) \tag{6.29}$$

where $l(x)$ and $cs(x)$ are same as the SSIM, α and β are constant. In this case, it is 1 and $j = 1, 2, 3, ..., M$. Like SSIM, MS-SSIM can also be maximized for better results. MS-SSIM loss is defined as,

$$\mathcal{L}_{MS\text{-}SSIM} = -1 \times MS\text{-}SSIM \tag{6.30}$$

Therefore, the gradient of the MS-SSIM loss is given by,

$$\frac{\partial \mathcal{L}_{MS\text{-}SSIM}}{\partial I(y)} = (\frac{\partial l_M(x)}{\partial I(y)} + l_M(x).\sum_{i=1}^{M}\frac{1}{cs_i(x)}.\frac{\partial cs_i(x)}{\partial I(y)}).\prod_{i=1}^{M} cs_j(x) \tag{6.31}$$

Quadruplet Loss Function: In this chapter, a combination of $\mathcal{L}_{MSE}$, $\mathcal{L}_{PSNR}$, $\mathcal{L}_{SSIM}$, $\mathcal{L}_{MS\text{-}SSIM}$ are used. $\mathcal{L}_{SSIM}$ helps to learn more complex features, $\mathcal{L}_{MS\text{-}SSIM}$ reduces the artifacts, however, if only these two functions are used for the training, the reconstructed image may look dull. The $\mathcal{L}_{MSE}$ and $\mathcal{L}_{PSNR}$ preserve the color effect and sharpness,

TABLE 6.2: Hyper-parameter details for training LIDN

Hyper Parameter	**Value**
Optimizer	Adam $(\beta_1 = 0.9, \beta_2 = 0.99)$
Loss Function	Quadruplet Loss $(\lambda_1, \lambda_2 = 0.15, \lambda_3, \lambda_4 = 0.85)$
Initial Learning Rate	0.01
Learning Rate Decay	0.95
Lower Bound of learning rate	10^{-8}
Patience	7
Cooldown	5
Monitor	Validation Loss
Delta	0.001
Batch Size	1

and reduce dullness. Total loss is defined as

$$\mathcal{L}_Q = \lambda_1 \mathcal{L}_{MSE} + \lambda_2 \mathcal{L}_{PSNR} + \lambda_3 \mathcal{L}_{SSIM} + \lambda_4 \mathcal{L}_{MS\text{-}SSIM} \tag{6.32}$$

The final loss function used to train the LIDN model incorporates multiple components, each scaled by specific weights denoted as λ_1, λ_2, λ_3, and λ_4. For the experiments presented in this chapter, these weights are set to $\lambda_1 = 0.15$, $\lambda_2 = 0.15$, $\lambda_3 = 0.85$, and $\lambda_4 = 0.85$.

While Mean Squared Error (MSE) and Peak Signal-to-Noise Ratio (PSNR) have traditionally been used for assessing image similarity, they often fall short in capturing perceptual quality and intricate visual structures. In contrast, the Structural Similarity Index Measure (SSIM) and its multi-scale variant (MS-SSIM) are designed to align more closely with human visual perception by considering luminance, contrast, and structural fidelity. To emphasize their perceptual relevance, higher weights are allocated to SSIM and MS-SSIM in the loss formulation.

The model is trained using various combinations of the loss functions—MSE, PSNR, SSIM, and MS-SSIM—under different λ configurations. The qualitative effects of these loss functions are illustrated in Figure 6.9. From these results, it is evident that using SSIM and MS-SSIM as dominant loss components leads to superior image quality, particularly in terms of color fidelity. Conversely, assigning greater weights to MSE and PSNR, or distributing equal weight across all loss terms, results in suboptimal outcomes, as shown in Figure 6.9.

Figure 6.10 displays the training and validation loss curves for the LIDN model under these different loss configurations. To further investigate performance, the network is trained across three distinct color spaces: LAB, RGB, and YIQ. The corresponding loss curves are presented in Figure 6.11. These curves reveal that the LAB and RGB-based models achieve more stable convergence and lower overall loss values compared to their YIQ-based counterpart. Specifically, the YIQ color space exhibits erratic fluctuations in its loss curve, indicating unstable optimization. In contrast, the loss curves for LAB and RGB exhibit smoother, more consistent downward trends. Among them, the LAB color space demonstrates the most effective learning behavior, suggesting that training in LAB results in improved model convergence and enhanced dehazing performance.

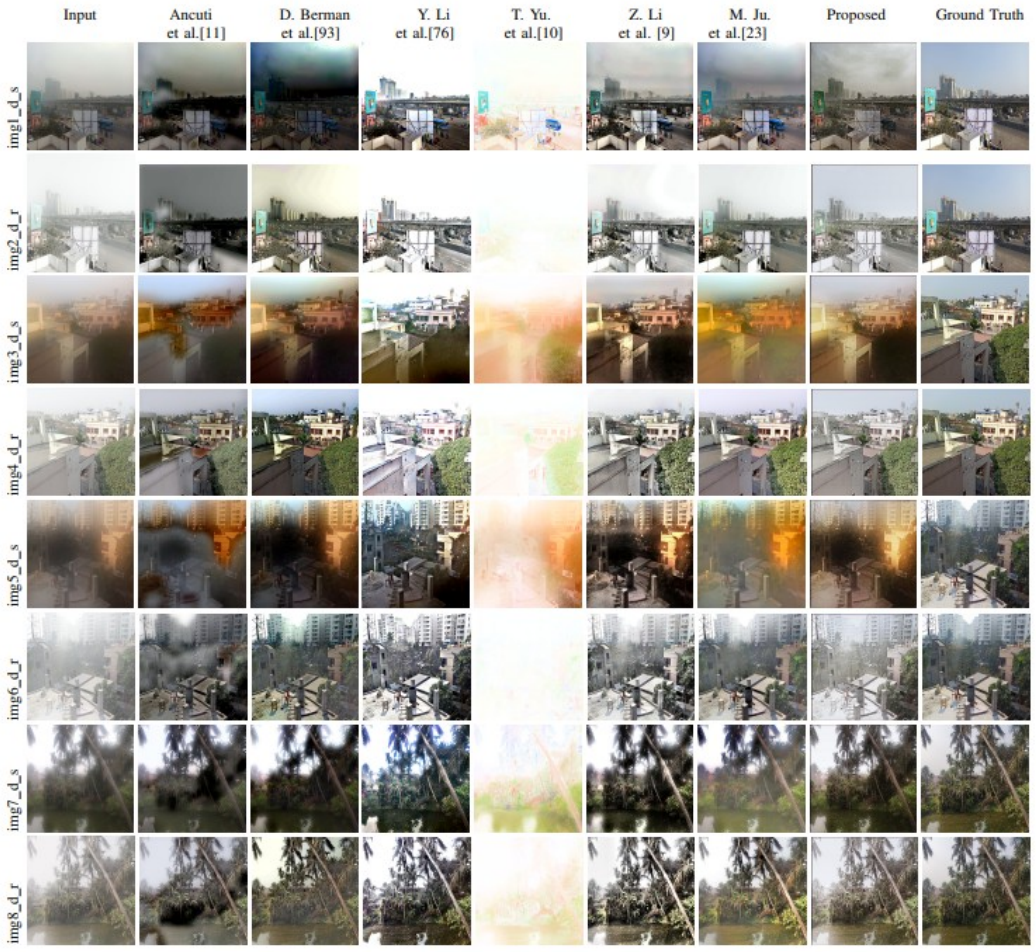

FIGURE 6.12: Comparative Analysis of the Proposed Method and Existing Models on Daytime Images from the Daytime and Nighttime Dehazing Benchmarking Database.

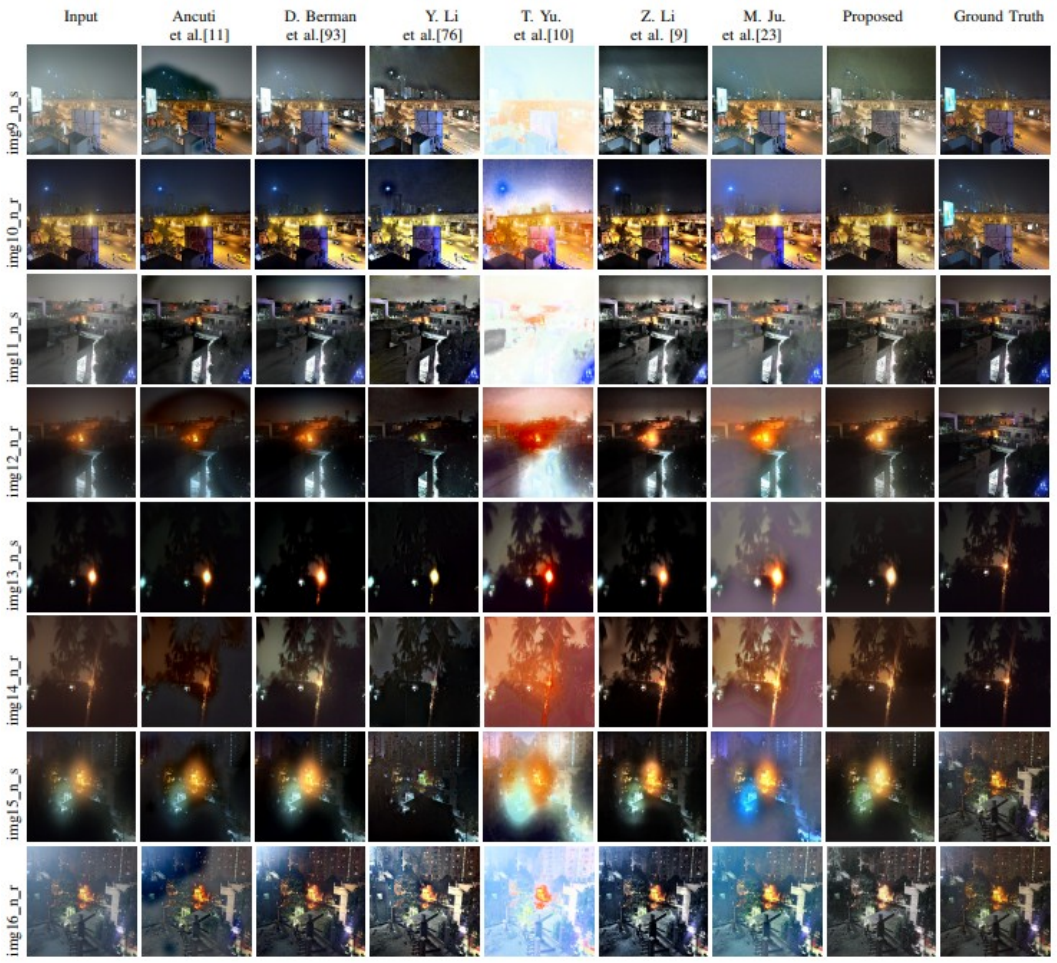

FIGURE 6.13: Comparative Analysis of the Proposed Method and Existing Models on Nighttime Images from the Daytime and Nighttime Dehazing Benchmarking Database

TABLE 6.3: Performance Evaluation of the Proposed Method Against Existing Models on Daytime Images from the Daytime and Nighttime Dehazing Benchmarking Database. SSIM, MSSIM, PSNR, and MSE metrics are compared, with the top three results highlighted in red, blue, and green fonts, respectively. In most cases, the proposed model demonstrates superior performance over other existing methods.

	SSIM	MSSIM	PSNR(dB)	MSE
Proposed model	**0.413**	**0.585**	**13.583**	**11.382**
Ancuti et al.(11)	**0.415**	0.559	**14.413**	**10.575**
D. Berman et al.(90)	**0.392**	**0.581**	**13.797**	13.942
M. Ju. et al.(23)	0.374	**0.582**	11.621	18.133
Y. Li et al. (76)	0.355	0.551	13.215	12.650
Z. Li et al. (9)	0.389	0.553	13.244	**12.420**
T. Yu.et al. (10)	0.237	0.324	5.290	86.183

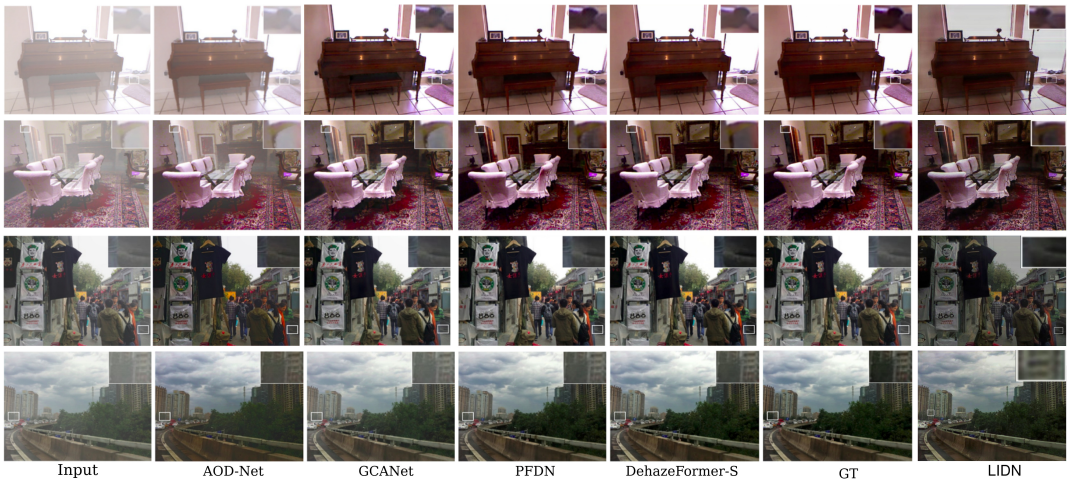

FIGURE 6.14: Qualitative Comparison of Image Dehazing Techniques on the SOTS-Mix Dataset. The first two rows represent indoor images, while the last two rows correspond to outdoor images. The first column displays the hazy input images, the second-to-last column presents the corresponding ground truth, and the final column showcases the dehazed results.

TABLE 6.4: Evaluation of SSIM, MSSIM, PSNR, and MSE Metrics for the Proposed Method Against Existing Models on **Nighttime Images** from the Daytime and Nighttime Dehazing Benchmarking Database. The top three results are highlighted in red, blue, and green fonts, respectively. In most cases, the proposed model outperforms other existing methods.

	SSIM	MSSIM	PSNR(dB)	MSE
Proposed model	**0.393**	**0.500**	**14.222**	**11.094**
Ancuti et al.(11)	**0.375**	**0.468**	**14.083**	**12.635**
D. Berman et al.(90)	0.322	**0.488**	13.769	**13.080**
M. Ju. et al.(23)	0.304	**0.468**	9.177	20.409
Y. Li et al. (76)	**0.346**	0.450	**14.505**	16.992
Z. Li et al. (9)	0.299	0.466	13.620	13.553
T. Yu.et al. (10)	0.299	0.369	7.889	52.875

6.4.3.3 Hyperparameter Configuration and Training Setup

The implementation of the proposed LIDN model is carried out using TensorFlow 2.4.2, and the training is performed in a Google Colab environment equipped with an NVIDIA Tesla T4 GPU (15GB VRAM) and 13GB of system RAM.

The model is optimized using the Adam optimizer with exponential decay rates set to $\beta_1 = 0.9$ and $\beta_2 = 0.999$. Training begins with a batch size of 1 and an initial learning rate of 0.01. A learning rate scheduler is applied such that if the validation loss does not decrease by at least 0.001 over 7 consecutive epochs (patience), the learning rate is

TABLE 6.5: Evaluation of SSIM, MSSIM, PSNR, and MSE Metrics for the Proposed Method Against Existing Models on **Real Hazy Images** from the Daytime and Nighttime Dehazing Benchmarking Database. The top three results are highlighted in red, blue, and green fonts, respectively. In most cases, the proposed model demonstrates superior performance compared to existing methods.

	SSIM	MSSIM	PSNR(dB)	MSE
Proposed model	**0.409**	**0.547**	**14.127**	**10.790**
Ancuti et al.(11)	**0.402**	0.526	**13.777**	**12.28**
D. Berman et al.(90)	0.326	0.526	**13.571**	14.18
M. Ju. et al.(23)	0.353	**0.535**	11.710	18.81
Y. Li et al. (76)	**0.355**	0.517	12.495	16.66
Z. Li et al. (9)	0.336	**0.528**	13.219	**13.39**
T. Yu.et al. (10)	0.315	0.354	7.382	58.09

TABLE 6.6: Evaluation of SSIM, MSSIM, PSNR, and MSE Metrics for the Proposed Method Against Existing Models on **Synthetic Hazy Images** from the Daytime and Nighttime Dehazing Benchmarking Database. The top three results are highlighted in red, blue, and green fonts, respectively. In most cases, the proposed model outperforms other existing methods.

	SSIM	MSSIM	PSNR(dB)	MSE
Proposed model	**0.397**	**0.537**	13.594	**11.80**
Ancuti et al.(11)	**0.387**	0.500	**14.786**	**10.83**
D. Berman et al.(90)	**0.393**	**0.545**	**14.026**	12.74
M. Ju. et al.(23)	0.323	**0.519**	11.232	19.80
Y. Li et al. (76)	0.346	0.481	**13.713**	12.72
Z. Li et al. (9)	0.353	0.488	13.644	**12.53**
T. Yu.et al. (10)	0.214	0.338	5.684	82.61

TABLE 6.7: Performance Comparison of SSIM, MSSIM, PSNR, and MSE for the Proposed Method Against Existing Models in the Daytime and Nighttime Dehazing Benchmarking Database. The top three results are highlighted using red, blue, and green fonts, respectively. In the majority of cases, the proposed model demonstrates superior performance compared to other existing methods.

Metric	Proposed model	Ancuti et al..(11)	D. Berman et al.(90)	M. Ju. et al.(23)	Y. Li et al. (76)	Z. Li et al. (9)	T. Yu. et al.(10)
SSIM	**0.403**	**0.395**	**0.357**	0.339	0.350	0.344	0.268
MSSIM	**0.542**	**0.513**	**0.534**	0.527	0.500	0.509	0.347
PSNR	**13.90**	**14.24**	**13.78**	11.49	13.06	13.42	6.59
MSE	**11.24**	**11.60**	13.51	19.27	14.82	**12.99**	69.53
Runtime(s)	**0.240**	**0.300**	0.352	**0.257**	0.359	0.631	0.305

TABLE 6.8: Evaluation of SSIM, PSNR, MSE, and MSSIM Metrics for the Proposed Model on the **RESIDE6K** Database. The model is assessed using MSE, PSNR, MSSIM, and SSIM loss functions, as well as Quadruplet loss with varying values in the LAB color space. Additionally, its performance is analyzed with Quadruplet loss applied to RGB, LAB, and YIQ color spaces..

Loss	Color Space	MSE	PSNR	SSIM	MSSIM
MSE	LAB	0.0141	18.5079	0.7001	0.743
PSNR(dB)	LAB	0.2779	5.5606	0.3976	0.4296
SSIM	LAB	0.0017	27.4790	0.9620	0.994
MSSIM	LAB	0.0076	21.1462	0.8988	0.9378
Quadruplet loss($\lambda_1, \lambda_2 = 0.15, \lambda_3, \lambda_4 = 0.85$)	LAB	0.1253	9.0199	0.3697	0.4047
Quadruplet loss($\lambda_1, \lambda_2 = .50, \lambda_3, \lambda_4 = 0.50$)	LAB	0.5069	2.9502	0.1844	0.2074
Quadruplet loss($\lambda_1, \lambda_2 = 0.85, \lambda_3, \lambda_4 = 0.15$)**(proposed)**	LAB	**0.000001**	**68.32**	**0.997**	**1.0**
Quadruplet loss($\lambda_1, \lambda_2 = 0.85, \lambda_3, \lambda_4 = 0.15$)	YIQ	0.5335	2.5753	0.1536	0.1690
Quadruplet loss($\lambda_1, \lambda_2 = 0.85, \lambda_3, \lambda_4 = 0.15$)	RGB	0.1778	15.302	0.606	0.652

TABLE 6.9: Comparison of PSNR, SSIM, MSE, and MSSIM Metrics for the Proposed Method and Existing Models in the **I-HAZE, O-HAZE, Dense-HAZE, and NH-HAZE Databases**. The top three results are highlighted in red, blue, and green fonts, respectively. In most cases, the proposed model demonstrates superior performance compared to other existing methods.

Dataset	**I-Haze**				**O-Haze**			
Method	**PSNR(dB)**	**SSIM**	**MSE**	**MSSIM**	**PSNR(dB)**	**SSIM**	**MSE**	**MSSIM**
DCP(18)	**14.43**	**0.7516**	**10.44**	0.8916	**16.78**	**0.6532**	**7.97**	**0.8916**
CAP(20)	12.24	0.6065	13.44	**0.7665**	16.08	0.5965	8.64	0.7365
AOD-Net(91)	13.98	0.7323	10.99	0.8523	15.03	0.5385	9.75	**0.8723**
QCNN-H(92)	14.118	0.612	10.825	-	17.440	0.545	7.9852	-
EDN-Net(93)	**22.9**	**0.827**	**3.93**	**0.997**	**23.46**	**0.8198**	**3.69**	**1.0**
LIDN(Proposed)	**63.32**	**0.995**	**0.038**	**1.0**	**63.26**	**0.996**	**0.04**	**1.0**
Dataset	**Dense-Haze**				**NH-Haze**			
Method	**PSNR(dB)**	**SSIM**	**MSE**	**MSSIM**	**PSNR(dB)**	**SSIM**	**MSE**	**MSSIM**
DCP(18)	10.06	**0.3856**	2.70	0.5256	10.57	0.5196	16.29	0.6596
DehazeNet(81)	**13.84**	0.4252	**0.87**	**0.5652**	**16.62**	0.5238	**8.12**	0.6638
AOD-Net(91)	13.14	0.4144	1.07	0.5544	15.4	**0.5693**	9.34	**0.7093**
EDN-Net(93)	**15.43**	**0.52**	**0.54**	**0.74**	**20.24**	**0.7178**	**5.35**	**0.9278**
LIDN(Proposed)	**68.32**	**0.988**	**0.004**	**1.0**	**59.24**	**0.992**	**0.06**	**1.0**

scaled down by a factor of 0.95. This update rule can be expressed as:

$$lr_i = \text{factor} \times lr_{i-1}$$

where the factor is 0.95. The minimum allowable learning rate is 10^{-8}, and learning rate adjustments are halted for 5 epochs after a reduction, referred to as the cooldown period. All training hyperparameters used for the LIDN model are summarized in Table 6.2.

TABLE 6.10: Evaluation of PSNR, SSIM, MSE, MSSIM, and Overhead for the Proposed Method Compared to Existing Models in the **ITS, OTS** Database. The top three results are highlighted in red, blue, and green fonts, respectively. In most cases, the proposed model exhibits superior performance compared to other existing methods.

Dataset	ITS-Haze				OTS-Haze				Overhead
Method	PSNR(dB)	SSIM	MSE	MSSIM	PSNR(dB)	SSIM	MSE	MSSIM	#Param
DCP(18)	16.62	0.818	0.378	0.958	16.62	0.815	0.378	0.845	-
DehazeNet(81)	19.82	0.821	0.145	0.961	24.75	0.927	0.033	0.957	**0.009M**
MSCNN(75)	19.84	0.833	0.144	0.973	22.06	0.908	0.074	0.938	**0.008M**
AOD-Net(91)	20.52	0.816	0.118	0.956	24.14	0.92	0.040	0.95	**0.002M**
GFN(94)	22.3	0.88	0.069	0.89	21.55	0.844	0.086	0.874	0.499M
GCANet(95)	30.23	0.98	0.006	0.99	19.95	0.866	0.139	0.89	0.702M
GridDehazeNet(96)	32.16	0.984	0.003	0.994	30.86	0.982	0.0053	**0.998**	0.956M
MSBDN(97)	33.67	0.985	0.002	0.995	33.48	0.982	0.0024	**0.999**	31.35M
PFDN(98)	32.68	0.976	0.003	0.986	23.62	0.948	0.046	0.972	11.27M
FFA-Net(99)	36.39	0.989	0.001	0.992	33.57	**0.984**	0.002	0.997	4.456M
AECR-Net(100)	37.17	0.99	0.0008	0.993					2.611M
DehazeFormer-T(101)	35.15	0.989	0.001	0.994	33.71	0.982	0.002	0.995	0.686M
DehazeFormer-S(101)	36.82	0.992	0.0009	0.995	34.36	**0.983**	0.002	0.996	1.283M
DehazeFormer-B(101)	37.84	**0.994**	0.0006	**0.997**	**34.95**	**0.984**	**0.0019**	0.997	2.514M
DehazeFormer-M(101)	**38.46**	**0.994**	**0.0005**	**0.997**	**34.29**	**0.983**	**0.0017**	0.993	4.634M
DehazeFormer-L(101)	**40.05**	**0.996**	**0.0003**	**0.999**					25.44M
LIDN(Proposed Method)	**68.75**	**0.998**	**0.000001**	**1**	**67.89**	**0.996**	**0.000001**	**1**	5.074M

TABLE 6.11: Evaluation of PSNR, SSIM, MSE, and MSSIM Metrics for the Proposed Method Compared to Existing Models in the **RESIDE6K** Database. The top three results are highlighted in red, blue, and green fonts, respectively. In most cases, the proposed model outperforms other existing methods.

Dataset	RESIDE6K			
Method	PSNR(dB)	SSIM	MSE	MSSIM
DCP(18)	17.88	0.816	0.259	0.846
DehazeNet(81)	21.02	0.87	0.101	0.9
MSCNN(75)	20.31	0.863	0.125	0.893
AOD-Net(91)	20.27	0.855	0.127	0.885
GFN(94)	23.52	0.905	0.048	0.935
GCANet(95)	25.09	0.923	0.029	0.953
GridDehazeNet(96)	25.86	0.944	0.024	0.974
MSBDN(97)	28.56	0.966	0.011	**0.996**
PFDN(98)	28.15	0.962	0.012	0.992
FFA-Net(99)	29.96	0.973	0.007	0.99
AECR-Net(100)	28.52	0.964	0.011	0.981
DehazeFormer-T(101)	30.36	0.973	0.006	0.99
DehazeFormer-S(101)	30.62	0.976	0.006	0.993
DehazeFormer-B(101)	**31.45**	**0.98**	**0.004**	**0.997**
DehazeFormer-M(101)	**30.89**	**0.977**	**0.005**	0.994
DehazeFormer-L(101)				
LIDN(Proposed)	**68.32**	**0.997**	10^{-6}	**1**

6.5 Experimental Evaluation

To assess the effectiveness of the proposed dehazing model, comparisons are made against six existing state-of-the-art techniques introduced by Ancuti et al. (11), Berman et al. (90), Y. Li et al. (76), Z. Li et al. (9), M. Ju et al. (23), and T. Yu et al. (10). Evaluation is conducted on both daytime and nighttime hazy images using the Daytime and Nighttime Dehazing Benchmarking Database (86).

In addition, a broader comparison is carried out using fourteen prominent models: DCP (18), DehazeNet (81), MSCNN (75), AOD-Net (91), GFN (94), GCANet (95), GridDehazeNet (96), MSBDN (97), QCNN-H (92), PFDN (98), FFA-Net (99), AECR-Net (100), and DehazeFormer-T (101). These models are evaluated on datasets including SOTS-indoor, OTS-outdoor, and OTS-mix. Furthermore, DCP (18), DehazeNet (30), AOD-Net (91), CAP (19), and EDN-Net (93) are compared on benchmark datasets I-HAZE (82), O-HAZE, Dense-HAZE (85**?**), and NH-HAZE (84).

6.5.1 Quantitative Analysis

The proposed LIDN model's performance is quantitatively benchmarked against the methods developed by Ancuti et al. (11), Berman et al. (90), Y. Li et al. (23), Z. Li et al. (76), M. Ju et al. (9), and T. Yu et al. (10) for both daytime and nighttime scenarios. Figure 6.12 and Figure 6.13 illustrate the comparative results, showing input hazy images, their ground truths, and outputs from the aforementioned methods.

The filenames follow the format '`img1_d(n)_r(s)`', where 'img1' denotes the image index, 'd/n' represents daytime or nighttime, and 'r/s' indicates real or synthetic haze. The proposed LIDN model demonstrates superior performance, particularly in real haze conditions, outperforming other methods in both lighting conditions.

Among the compared techniques, T. Yu et al.'s (10) method shows considerable artifact generation and performs less effectively during the day than at night. For synthetic hazy images, M. Ju et al.'s (9) approach yields more accurate results; however, overall, the proposed model exhibits better robustness and consistency across scenarios.

A qualitative comparison on the SOTS-mix dataset is provided in Figure 6.14, where the upper rows present indoor image results and the lower rows correspond to outdoor scenes. The comparison includes outputs from AOD-Net, GCANet, PFDN, and DehazeFormer-S alongside those from the proposed LIDN model.

6.5.2 Quantitative Evaluation

Given the generally high performance of all evaluated algorithms, visual assessment alone is insufficient to differentiate model performance. Therefore, quantitative evaluation becomes essential. This study employs four widely accepted full-reference metrics—Mean Squared Error (MSE), Structural Similarity Index (SSIM), Multi-Scale SSIM (MS-SSIM), and Peak Signal-to-Noise Ratio (PSNR)—as detailed in Section IV. The proposed LIDN model is assessed under both illuminated and non-illuminated conditions, and for both synthetic and real haze scenarios.

Table 6.3 provides a comparative analysis of six state-of-the-art models on daytime dehazing. The proposed approach achieves the highest MS-SSIM and PSNR scores, while the method by Ancuti et al. (11) leads in SSIM and MSE, with LIDN ranking second. For nighttime scenes, as shown in Table 6.4, our model ranks first in MS-SSIM, MSE, and SSIM, and second in PSNR. Evaluation on real haze images, presented in Table 6.5, demonstrates that LIDN outperforms all others across all four metrics. When tested on synthetic hazy images (Table 6.6), it ranks second for MS-SSIM and MSE but excels in SSIM.

Overall, the proposed model consistently outperforms prior methods on real haze and remains robust across varying lighting conditions. The average performance across the Daytime and Nighttime Dehazing Benchmarking Database (Table 6.7) shows LIDN leading in SSIM, MS-SSIM, and MSE, while Ancuti et al. (11) obtain the highest PSNR, closely followed by LIDN. Evaluations on the ITS, OTS, and RESIDE6K datasets, summarized in Table 6.10 and Table 6.11, confirm LIDN's superior SSIM and PSNR results. Additionally, Table 6.9 shows LIDN achieving state-of-the-art performance in PSNR and SSIM across the I-HAZE, O-HAZE, Dense-HAZE, and NH-HAZE datasets.

6.5.3 Ablation Study

An ablation study was conducted to assess the influence of different loss functions and color spaces on image reconstruction quality, using the RESIDE6K dataset. The study reveals that the proposed model, using a Quadruplet loss with weighted parameters $\lambda_1 = \lambda_2 = 0.85$ and $\lambda_3 = \lambda_4 = 0.15$, performs optimally when applied in the LAB color space.

Evaluation using MSE, PSNR, SSIM, and MS-SSIM shows that this configuration achieves an MSE of 0.000001, a PSNR of 68.32, an SSIM of 0.997, and an MS-SSIM of 1.0, indicating superior reconstruction quality.

For comparison, performance in alternative color spaces was also measured. In the YIQ space, the model yields MSE = 0.5335, PSNR = 2.5753, SSIM = 0.1536, and MS-SSIM = 0.1690. In the RGB space, the results are MSE = 0.1778, PSNR = 15.302, SSIM = 0.606, and MS-SSIM = 0.652. These outcomes confirm that the LAB color space is significantly more effective across all evaluation criteria.

This ablation study highlights the critical role of loss function selection and color space in image dehazing, affirming the effectiveness of the Quadruplet loss in LAB space for high-fidelity reconstruction.

6.6 Chapter Conclusion

This chapter introduced the LIDN model, an end-to-end framework tailored for single-image dehazing in both daytime and nighttime conditions. Experiments conducted across RGB, YIQ, and LAB color spaces show that the LAB representation yields the most visually and quantitatively consistent results, while RGB and YIQ outputs exhibit noticeable artifacts.

Extensive benchmarking on the Daytime and Nighttime Dehazing Benchmarking Database confirms LIDN's leading performance in real-haze conditions, though some minor artifacts appear in synthetic cases. LIDN consistently outperforms competing approaches across most standard metrics, excluding PSNR where it remains competitive. Runtime analysis reveals that the model processes each image in 0.240 seconds on an NVIDIA Tesla T4 GPU and in 0.331 seconds on an NVIDIA GEFORCE 940MX GPU.

Despite its strong performance, the model does show a minor color shift issue, suggesting avenues for future refinement. Nonetheless, LIDN demonstrates robust, state-of-the-art dehazing performance across a wide range of datasets and conditions.

Chapter 7

Hardware Implementation for Video Processing

7.1 Introduction

Existing dehazing algorithms face several challenges, including loss of image details in enhancement-based methods and the requirement for manual feature extraction in physical model-based approaches. Deep learning-based techniques, while promising, still depend on physical scattering models, which can result in image smoothing, detail loss, and reduced clarity due to the reliance on mean square loss. Additionally, many existing dehazing methods demand high processing power, making them impractical for real-time applications.

To overcome these limitations, this chapter introduces a real-time video dehazing technique utilizing a novel haze parameter, 'SATVAL', which is defined as the ratio of maximum saturation to maximum value in an RGB image. This parameter is applied within an image scattering model, enabling efficient dehazing by processing only a few video frames per second. A frame with a 'SATVAL' ratio below a predefined threshold is considered already dehazed and is passed without additional processing, significantly improving real-time performance.

To validate the proposed method, a low-computation device, Raspberry Pi Model 4B, is used to assess its effectiveness. This implementation demonstrates that the approach achieves real-time video dehazing with minimal computational overhead, making it comparable to existing high-performance methods while being suitable for resource-constrained environments.

7.1.1 Contributions

The key contributions of this chapter are as follows:

[0] **A. Ghosh** and S. S. Chaudhuri, "**IOT based Portable Image Dehazing Machine**," 2021 8th International Conference on Signal Processing and Integrated Networks (SPIN), Noida, India, 2021, pp. 31-35, doi: 10.1109/SPIN52536.2021.9565998.

[0] **A. Ghosh**, A. Ali and S. S. Chaudhuri, "**Novel Parametric Based Time Efficient Portable Real-Time Dehazing System**". Journal of Real-Time Image Processing. https://doi.org/10.1007/s11554-023-01283-x

[0] **A. Ghosh**, S. Bhowmick and S. S. Chaudhuri, "**Real-Time Image Dehazing via a Novel Parallel Architecture: An Empirical Comparison of Hardware Platforms**." Journal of Signal, Image and Video Processing. Accepted,**Impact Factor- 2.0**

[0] **https://www.raspberrypi.com/**

7.1.1.1 Introduction of SATVAL

This paper introduces **SATVAL**, a novel haze parameter that determines whether a dehazing algorithm needs to be applied to a video frame. By selectively processing only the frames requiring dehazing, this approach significantly reduces computational complexity, making real-time video dehazing more efficient.

7.1.1.2 SATVAL Video Dataset

A new **dataset of ten hazy videos** has been created and made available in this work. This dataset serves as a valuable benchmark for evaluating and comparing dehazing algorithms, enabling future research in real-time video dehazing.

7.1.1.3 Real-Time Hardware Implementation

Unlike most existing dehazing models, which are primarily **simulation-based**, this work focuses on **real-time implementation**. The proposed method is deployed on a **Raspberry Pi Model 4B**, a **low-power, portable** computing device that facilitates real-time dehazing. This makes the system **suitable for autonomous driving applications**, where efficient dehazing is essential for **navigation and obstacle detection**. The portability of the system allows easy integration with **various peripheral devices**, making it adaptable to different real-world scenarios.

7.1.1.4 Empirical Comparison of the algorithm in Different Hardware Accelerator

A comparative analysis of different hardware platforms is conducted, evaluating their performance and output quality, with a detailed discussion on their suitability for real-time applications.

7.2 Hardware Description

Raspberry Pi 4B, PYNQ-Z2, and Jetson Nano are popular embedded platforms, each tailored for specific use cases—general-purpose computing, FPGA-based hardware acceleration, and AI at the edge, respectively. Together, they offer a diverse range of capabilities for prototyping, research, and real-time application development.

7.2.1 Raspberry Pi

The demand for compact, single-board computers like the Raspberry Pi has grown significantly, particularly for embedded systems and Internet of Things (IoT) applications. The Raspberry Pi 4 Model B, a recent iteration, features a quad-core Cortex-A72 (ARM v8) 64-bit processor running at 1.5 GHz, along with 4GB of LPDDR4-2400 SDRAM, powered by the Broadcom BCM2711 SoC.

This model excels in networking and multimedia performance due to its high-speed 64-bit processor, hardware video decoding up to 4Kp60, and support for dual 4K displays via micro-HDMI connectors. Its connectivity options include Gigabit Ethernet, USB 3.0, Bluetooth 5.0, dual-band WiFi (2.4/5.0 GHz), and Power over Ethernet (PoE) support (with an additional PoE HAT). The Raspberry Pi Model 4B is an ideal choice for real-time video processing, thanks to its combination of processing power and portability. The operating system is loaded via an externally inserted microSD card.



FIGURE 7.1: Experimental setup with Raspberry Pi Model 4B

Figure 7.3 illustrates an experimental setup utilizing the Raspberry Pi Model 4B. The device is connected to external monitors via dual micro-HDMI ports, showcasing its high-resolution output capabilities. Peripherals such as a keyboard, mouse, and optional external storage enhance functionality, while a camera module provides real-time video input. To ensure stable operation, a cooling solution (heat sink or fan) and a USB-C power adapter are included. This configuration leverages the Raspberry Pi's computational power for efficient video processing and other real-time tasks.

7.2.2 PYNQ-Z2

The PYNQ-Z2 board is a versatile development platform based on the Xilinx Zynq-7000 SoC, which integrates a dual-core ARM Cortex-A9 processor with programmable FPGA logic. This board enables hardware-software co-design, making it suitable for embedded systems, IoT, and machine learning applications.

The PYNQ-Z2 provides various connectivity options, including Ethernet, USB, HDMI, audio, and Pmod connectors, allowing interaction with sensors, displays, and peripherals. It also features 512MB of DDR3 RAM, a microSD card slot for storage, and multiple GPIO pins for general-purpose input/output.

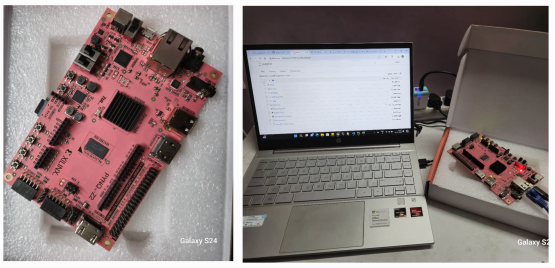

FIGURE 7.2: PYNQ-Z2 Board

A key advantage of the PYNQ-Z2 is its support for the PYNQ framework, which allows users to program the FPGA using Python, making FPGA development more accessible to software engineers and data scientists. Its HDMI ports facilitate video processing, while Pmod connectors and GPIO pins support custom hardware projects. The PYNQ-Z2 is widely used in academic research, prototyping, and educational settings, where it enables the seamless integration of hardware and software on a single platform.

The board can be connected to a laptop via Ethernet, enabling remote programming and control through a Jupyter Notebook interface. This setup allows users to upload bitstreams, execute Python scripts, and manage data transfer efficiently, making it ideal for real-time processing and debugging. The board is powered via a micro-USB port or an external adapter, ensuring stable operation during development.

Table 7.1: Comparison of Hardware for Image Dehazing

Category	**PYNQ Z2**	**Raspberry Pi**	**Jetson Nano**
Interface	UART, SPI, I2C, Jupyter, GPIO	Camera, USB, SPI, I2C, GPIO	CSI Camera, USB, GPIO
Python Framework	Uses Python on ARM to control FPGA blocks via overlays/IPs; enables hardware-accelerated functions through Python APIs.	Runs Python on CPU with libraries like NumPy/OpenCV; all dehazing operations are software-based.	Uses Python with PyCUDA/ Numba/ OpenCV-CUDA; offloads heavy tasks to GPU for faster processing.
Image Dehazing Process	Utilizes hardware-accelerated parallel architecture implemented on FPGA for real-time dehazing; includes optimized modules for atmospheric light estimation and guided filtering, achieving low latency and high efficiency.	Processes hazy images using CPU-based execution of traditional algorithms like Dark Channel Prior (DCP) and contrast enhancement; suitable for low-cost applications but slower in real-time scenarios.	Employs CUDA-based GPU acceleration to run classical image dehazing algorithms, offering faster processing than CPU but higher power consumption compared to FPGA platforms.

7.2.3 Jetson Nano

The NVIDIA Jetson Nano is a compact yet powerful development board designed for edge AI and embedded system applications. It features a quad-core ARM Cortex-A57 CPU and a 128-core NVIDIA Maxwell GPU, providing sufficient processing power for AI, deep learning, and computer vision tasks.

The Jetson Nano supports 4GB of LPDDR4 RAM, multiple GPIO pins, and connectivity options such as Gigabit Ethernet, HDMI, DisplayPort, USB 3.0, and microSD storage. It

is designed to integrate with various peripherals, including cameras and sensors, making it a highly adaptable platform.

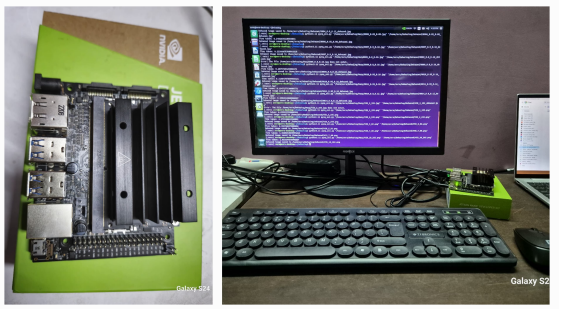

FIGURE 7.3: Jetson Nano Board

The Jetson Nano can be set up as a fully functional AI-powered desktop environment. It is connected to a monitor via HDMI, while USB ports support a keyboard, mouse, and additional peripherals. WiFi connectivity allows access to cloud services, software updates, and remote applications. By installing a Linux-based OS on a microSD card, the Jetson Nano operates as a compact yet efficient AI workstation, capable of running advanced deep learning frameworks.

This platform is ideal for developers and researchers working on robotics, edge computing, and AI-powered embedded systems.

7.3 Method1: Video Dehazing in IoT Device

In weather-degraded images, the presence of haze is influenced by both brightness and saturation (19). In a haze-free image, the difference between saturation and brightness is close to zero. Since haze concentration generally increases with scene depth, it can be assumed that scene depth is positively correlated with haze concentration, expressed as:

$$d(x) \propto c(x) \propto (v(x) - s(x)) \tag{7.1}$$

where $d(x)$ represents the scene depth, $c(x)$ is the haze concentration, $v(x)$ denotes the brightness of the scene, and $s(x)$ is the saturation.

Figure 7.4 (102) illustrates the **HSV color model** in vector space. The vector I, passing through the origin, represents the hazy image with components **H (Hue), S (Saturation), and V (Value)**. The value (V) is projected along the vertical center-line

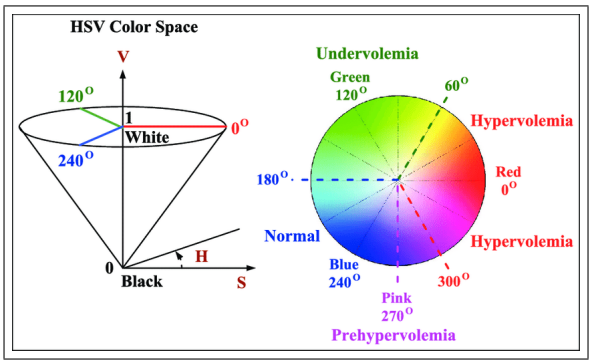

FIGURE 7.4: Geometric representation of the HSV color model

of an inverted cone, while H and S define the horizontal plane. The vector I forms an angle α with the horizontal plane (H-S).

Thus, H and S represent the projection of I in the horizontal plane, where the angle α varies within the range $[0, 90]$ degrees. A higher α value results in a higher tangent of α, thereby increasing the angle between V and S. As α increases, the difference between V and S becomes more pronounced. Additionally, since V increases and S decreases with increasing α, the relationship between V and S effectively represents the depth $d(x)$ of the image.

$$S(x) \propto (1/V(x)) \tag{7.2}$$

Thus, the angle α is directly proportional to the depth of an image. In summary, V, S, and d are the key intrinsic parameters that define the image I.

From Equation (6), the following relationship can be derived:

$$V(x) - S(x) = K \quad \text{[Constant]} \tag{7.3}$$

Further simplifying, I obtain

$$\frac{S(x)}{V(x)} = K1 \quad \text{[Constant]} \tag{7.4}$$

Here, $K1$ is a variable that depends on the haze level in each image. This implies that the values of V, S, and d in a degraded image differ from those in a corresponding clear image. Since haze affects both brightness and saturation, if either $S(x)$ or $V(x)$ is zero, pixel-wise calculations become impractical.

To address this challenge, robust dehazing algorithms are required to reconstruct a visually clear image from a weather-degraded input. In this chapter, a novel dehazing algorithm is proposed based on the above observations.

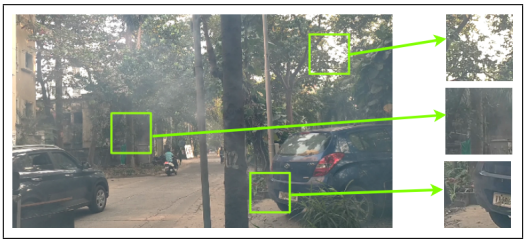

FIGURE 7.5: Different haze quality in different positions on an image and also the saturation and value components are different for these positions as well.

Based on the above discussion, a formula is proposed in which the *haze quality* of a video frame is quantified using the *ratio of maximum saturation to maximum brightness (value)*. This formulation is represented in Equation (8).

When calculating these values for an entire image, the *maximum saturation (S) and maximum brightness (V) are taken into account*, ensuring that the denominator is never zero. If both values are zero, it indicates the absence of any meaningful information in the image.

By leveraging this property, a formula is introduced where the *ratio of the maximum saturation to the maximum brightness* is used to represent the *haze quality of the image frame*, as expressed below:

$$\text{SATVAL} = H.F. = \frac{\max(S(x))}{\max(V(x))} \tag{7.5}$$

Where the value of $S(x)$ and $V(x)$ is represented as below:

$$S(x) = \begin{cases} 0 & \text{if } \max\limits_{C\in\{R,G,B\}} I^C(x) = 0 \\ 1 - \dfrac{\min\limits_{C\in\{R,G,B\}} I^C(x)}{\max\limits_{C\in\{R,G,B\}} I^C(x)} & \text{otherwise} \end{cases} \tag{7.6}$$

$$V(x) = \max_{C\in\{R,G,B\}} I^C(x) \tag{7.7}$$

After computing the *Haziness Factor*, it is compared against a predefined threshold to determine whether haze removal is required or if the frame can be displayed without

modification. The threshold value is established through experimentation with various images. If the *Haziness Factor* is below the threshold, the frame is considered sufficiently clear and remains unchanged; otherwise, dehazing is applied.

This approach significantly reduces *computational complexity*, enabling efficient real-time video processing. Additionally, as demonstrated below, this method helps minimize *information loss* during dehazing.

Algorithm 1: SATVAL Algorithm for Dehazing Hazy Frames

Input: Hazy frames
Output: Dehazed frames

```
for each frame do
    Calculate S(x) and V(x) for all pixels in the image;
    Calculate max(S(x)) and max(V(x)) of the image;
    Calculate SATVAL = max(S(x)) / max(V(x)) parameter;
    if SATVAL < threshold then
        Calculate Atmospheric Light;
        Calculate Transmission Coefficient;
        Recover the scene;
    end
end
```

The flowchart provides a clear step-by-step representation of the process. In a video, frames are processed individually, and dehazing is applied only when necessary. The algorithm evaluates each frame and selectively identifies those requiring dehazing, optimizing computational efficiency.

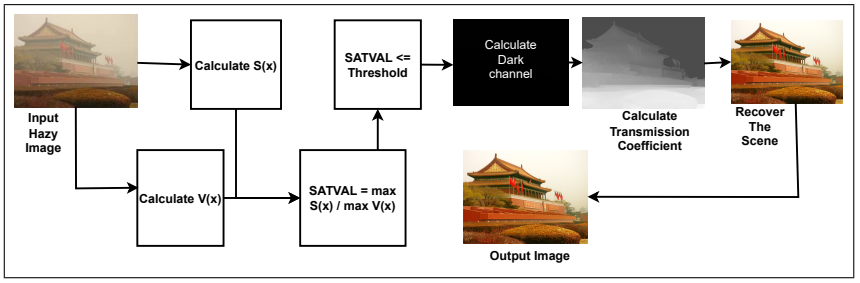

FIGURE 7.6: Flow chart of proposed dehazing algorithm using Raspberry Pi. Step-by-step procedure.

TABLE 7.2: Performance comparison of the Video processing with different sizes of frames in Raspberry Pi Model.

Serial No	**Video ID**	**FPS (128 Kbps)**	**FPS (256 Kbps)**	**FPS (512 Kbps)**
1	1	1.319	0.347	0.086
2	2	3.138	0.8359	0.419
3	4	10.544	10.556	10.5193
4	5	1.8541	0.9655	0.1684
5	8	1.873	0.5604	0.1699
6	9	14.652	13.8793	10.4403
7	10	2.6676	0.9354	0.3243
8	11	4.1096	1.2419	0.351
9	12	9.8844	5.149	2.3399

7.4 SATVAL DataSet

Proper dataset for testing video dehazing algorithm is unavailable, so ten videos have been taken in hazy weather. The processed video frames are displayed in the result section. Performance comparison of the proposed method with existing algorithm is carried out and presented in table 1. Altogether there are three parts of Data Sheet Preparation.

7.4.1 Acquisition

Videos are captured using cameras and mobile phones by creating artificial haze under varying lighting and color conditions.

The qualitative comparison with different existing algorithms is displayed in the table as also promising. All the images are processed as mentioned above. Quantitative comparison with different algorithms and analysis confirms the effectiveness of the proposed method. The SSIM and MSE values are showing competitive results with other existing algorithms. The PSNR(dB) and Correlation(CORR) values realized. Comparison is done between histogram equalization, dark channel prior-based method (18) , color channel prior based method (19) and Meng et Al. (70) proposed method. Experimental analysis is done in the classical state of the art method with different algorithms. But, due to hardware limitation, deep learning or machine learning process based dehazing method comparison is not possible in this scenario. Even if a centralized server is used instead of processing on a Raspberry Pi, real-time implementation remains challenging. Therefore, a comparison with state-of-the-art methods is presented here.

TABLE 7.3: Experimental Results for Different Videos in Raspberry Pi Model

Video ID	Frame No	Hazy Image	This Method
1			
2			
4			
5			
8			
9			
10			
11			
12			

TABLE 7.4: Qualitative Comparison Of Different Dehazing Algorithms With SATVAL



7.5 Method3: Empirical Comparison between Different Hardware Accelerator

The algorithmic contributions can be summarized into three key aspects: First, the optimization of Atmospheric Light estimation enables faster processing. Second, the enhancement of the guided filter for the Transmission coefficient improves overall image quality. Lastly, a parallel processing architecture has been introduced to enhance computational efficiency, as illustrated in Fig.

7.5.1 Atmospheric Light Estimation

The estimation of atmospheric light begins with an *erosion operation* applied to each color channel c of the image. The variable $\text{minImg}_c(x, y)$ represents the minimum value

Table 7.5: Comparison of Reference Image Quality Parameter for nine Videos for SSIM (Structural Similarity Index),PSNR(dB)(dB)(Peak Signal to Noise Ratio), MSE(Mean Square Error), CORR(Correlation)

Individual					
Serial No	Video ID	SSIM	PSNR(dB)	MSE	CORR
1	1	0.8507028668	27.87898656	105.9697	0.9573837792
2	2	0.8739131378	28.74692276	86.77369375	0.9377821638
3	4	0.8817704663	28.42862159	93.37233125	0.9418661048
4	5	0.8908317539	27.89332887	105.6203188	0.9391598403
5	8	0.8684756787	27.80329781	107.832725	0.8972447813
6	9	0.8668148723	28.35884029	94.88473125	0.892889773
7	10	0.8720327568	28.07863265	101.208525	0.9039515373
8	11	0.8682612364	27.89634441	105.5470063	0.9350820989
9	12	0.8608501589	28.12026089	100.24305	0.8931410671

Table 7.6: Comparison of SSIM for Different Algorithms

Image No.	**Histogram**	**DCP**	**CAP**	**MENG**	**This Method**
1	0.80	0.76	0.89	0.66	0.96
2	0.84	0.78	0.89	0.62	0.96
3	0.78	0.58	0.87	0.55	0.96
4	0.56	0.72	0.83	0.56	0.97
5	0.75	0.67	0.82	0.59	0.97

Table 7.7: Comparison for PSNR(dB) Values for Different Algorithms

Image No.	**Histogram**	**DCP**	**CAP**	**MENG**	**This Method**
1	28.36	27.76	28.51	27.59	29.01
2	28.14	27.92	28.33	27.90	29.43
3	27.87	28.85	27.77	28.42	27.61
4	27.84	27.50	28.14	27.53	28.27
5	27.91	27.81	27.65	27.80	29.40

Table 7.8: Comparison of MSE Values for Different Algorithms

Image No.	**Histogram**	**DCP**	**CAP**	**MENG**	**This Method**
1	94.76	108.79	91.62	113.33	81.61
2	99.71	105.04	95.50	105.39	74.14
3	106.25	84.67	108.77	93.65	112.64
4	106.89	115.65	99.76	114.89	96.86
5	105.13	107.67	111.58	107.81	74.62

within a window W_k centered at the pixel position (x, y). As the window slides over the image, for each position (u, v) within W_k, the pixel value at $(x + u, y + v, c)$ in channel

TABLE 7.9: Comparison of Correlation Values for Different Algorithms

Image No.	Histogram	DCP	CAP	MENG	This Method
1	0.94	0.84	0.88	0.87	0.94
2	0.97	0.87	0.92	0.81	0.95
3	0.98	0.67	0.93	0.67	0.95
4	0.88	0.93	0.97	0.92	0.97
5	0.93	0.93	0.95	0.91	0.97

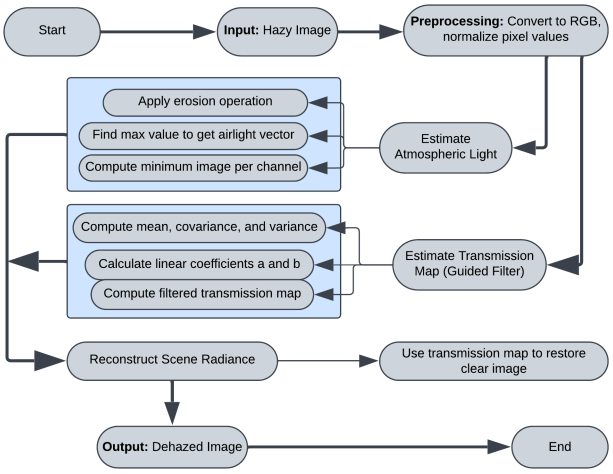

FIGURE 7.7: Flow Diagram for Proposed Method

c is considered. The minimum of these values is assigned to the corresponding pixel in the eroded image:

$$\text{minImg}_c(x, y) = \min_{(u,v)\in W_k} H(x + u, y + v, c) \tag{7.8}$$

The atmospheric light A_c for each channel c is then estimated by selecting the maximum value of the eroded image $\text{minImg}_c(x, y)$ across all pixel positions (x, y). This value represents the highest intensity of scattered light in the scene for the specific color channel:

$$A_c = \max_{(x,y)} \text{minImg}_c(x, y) \tag{7.9}$$

Finally, the airlight vector A is constructed by combining the airlight values A_c from all channels, typically representing the RGB color channels. This vector plays a crucial role in image dehazing and enhancement:

$$A = [A_1, A_2, \ldots, A_C] \tag{7.10}$$

7.5.2 Transmission Guide

The transmission map is estimated using a guided filtering approach, which involves calculating various statistical measures such as means, covariance, and linear coefficients.

7.5.2.1 Mean Calculations

- **Mean of I:**

$$\mu_I = \text{mean}(I) = \frac{1}{|\omega|} \sum_{i \in \omega} I(i) \tag{7.11}$$

- **Mean of p:**

$$\mu_p = \text{mean}(p) = \frac{1}{|\omega|} \sum_{i \in \omega} p(i) \tag{7.12}$$

- **Mean of $I \times p$:**

$$\mu_{Ip} = \text{mean}(I \times p) = \frac{1}{|\omega|} \sum_{i \in \omega} I(i) \times p(i) \tag{7.13}$$

7.5.2.2 Covariance and Variance Calculations

- **Covariance between I and p:**

$$\sigma_{Ip} = \mu_{Ip} - \mu_I \times \mu_p \tag{7.14}$$

- **Variance of I:**

$$\sigma_I^2 = \mu_{II} - \mu_I^2 \tag{7.15}$$

  where μ_{II} represents the mean of the squared values of I, i.e., $\mu_{II} = \text{mean}(I \times I)$.

7.5.2.3 Linear Coefficients

The linear coefficients a and b are computed as follows:

$$a = \frac{\sigma_{Ip}}{\sigma_I^2 + \epsilon} \tag{7.16}$$

$$b = \mu_p - a \times \mu_I \tag{7.17}$$

where ϵ is a regularization term to avoid numerical instability.

7.5.2.4 Mean of Coefficients

- **Mean of a:**

$$\mu_a = \text{mean}(a) \tag{7.18}$$

- **Mean of b:**

$$\mu_b = \text{mean}(b) \tag{7.19}$$

7.5.2.5 Filtered Image Output

The final guided filter output $q(i)$ is computed as:

$$q(i) = \mu_a(i) \times I(i) + \mu_b(i) \tag{7.20}$$

Complete Expression for the Guided Filter Output:

$$\begin{aligned} q(i) = &\left(\frac{\text{mean}(I \times p) - \text{mean}(I) \times \text{mean}(p)}{\text{mean}(I \times I) - (\text{mean}(I))^2 + \epsilon} \right) \times I(i) \\ &+ \left(\text{mean}(p) - \frac{\text{mean}(I \times p) - \text{mean}(I) \times \text{mean}(p)}{\text{mean}(I \times I) - (\text{mean}(I))^2 + \epsilon} \times \text{mean}(I) \right) \end{aligned} \tag{7.21}$$

This equation represents the guided filter's output $q(i)$ by combining mean values, covariance, and pixel intensities. The first term captures the slope $\mu_a(i)$ derived from the covariance between I and p, normalized by the variance of I. The second term $\mu_b(i)$ adjusts the output based on the means of p and I, ensuring a more refined estimate of the transmission map.

7.5.3 Parallel Execution and Synchronization:

- **Atmospheric Light Estimation:**

$$A = \mathcal{A}(I, M, w) \tag{7.22}$$

The atmospheric light A is estimated using the function $\mathcal{A}$, which takes as input the image I, a mask M, and a weight w. This function outputs the estimated atmospheric light A.

- **Raw Transmission Estimation:**

$$\text{rawt}, \text{rawt}_p = \mathcal{T}(I, r) \tag{7.23}$$

The raw transmission maps, rawt and rawt_p, are computed using the function $\mathcal{T}$, which takes the image I and a radius parameter r as inputs.

- **Parallel Execution:**

$$\text{Parallel Execution:} \quad A = \mathcal{A}(I, M, w), \quad (\text{rawt}, \text{rawt}_p) = \mathcal{T}(I, r) \tag{7.24}$$

During parallel execution, the atmospheric light A is estimated simultaneously with the computation of the raw transmission maps rawt and rawt_p. These operations are executed in parallel to improve efficiency.

- **After Synchronization:**

$$\text{After Synchronization:} \quad A \quad \text{and} \quad (\text{rawt}, \text{rawt}_p) \tag{7.25}$$

After parallel execution, the results A and $(\text{rawt}, \text{rawt}_p)$ are synchronized, meaning that both results are available and can be used for subsequent processing.

7.5.4 Qualitative Analysis:

The experimental results for dehazing various images processed using the PYNQ Board, Jetson Nano, and Raspberry Pi are presented in Table I. Each row displays the original hazy image, the ground truth (GT) image, and the dehazed outputs obtained from the three platforms. By comparing these results, a visual assessment of the performance and efficiency of the dehazing algorithms on each platform is facilitated, illustrating how effectively each technique restores clarity compared to the original hazy image and ground truth. A qualitative evaluation of different dehazing algorithms applied to video inputs is provided in Table II. This table includes dehazed results from multiple methods, including CAP, DCP, Hist, Meng, PYNQ, Raspberry Pi (R.Pi), and Jetson Nano (J.Nano). Each row showcases the dehazed outputs for the same video processed by different algorithms. Among these, the PYNQ platform consistently delivers the best results, significantly enhancing image clarity. This comparative analysis highlights the effectiveness of the PYNQ-based dehazing algorithm over alternative techniques.

TABLE 7.10: Experimental results for different images in PYNQ Board and Jetson Nano

Hazy Image	GT	PYNQ	Jetson NANO	Raspberry Pi
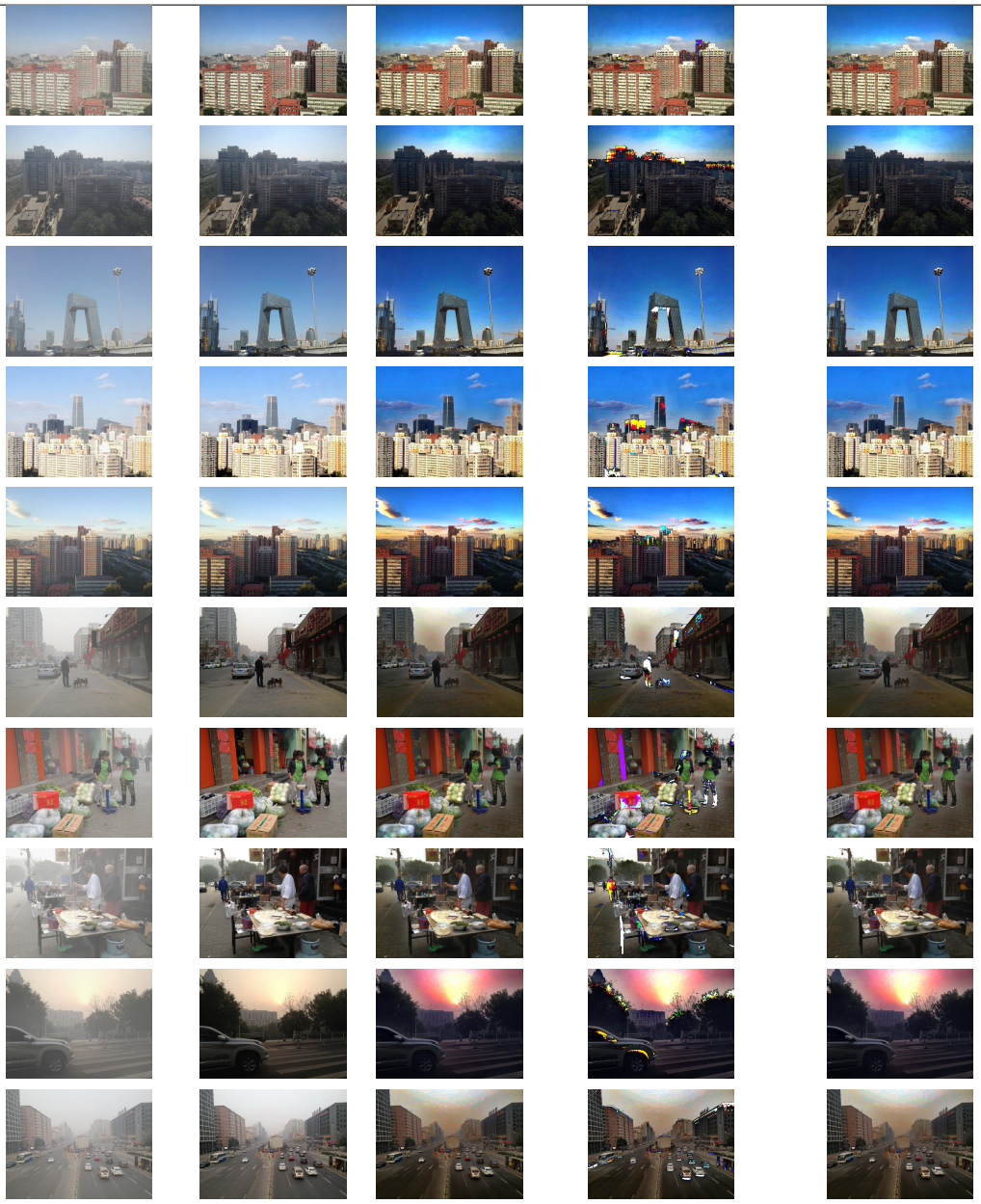				

7.5.5 Quantitative Analysis:

Ten images processed with a PYNQ board are used in this Tavle III to evaluate the dehazing algorithm's performance using metrics including PSNR(dB), MSE, CORR, SSIM, MS-SSIM, MDSI, and LPIPS(d). Higher PSNR(dB) values indicate better noise suppression; the range is 27.41 to 29.16. MSE values, which range from 78.87 to 117.97, indicate how much the results deviate from the original; lower values indicate better performance. While SSIM levels from 0.68 to 0.87 indicate visual perception accuracy, CORR values

TABLE 7.11: Qualitative Comparison Of Different Dehazing Algorithms With SATVAL

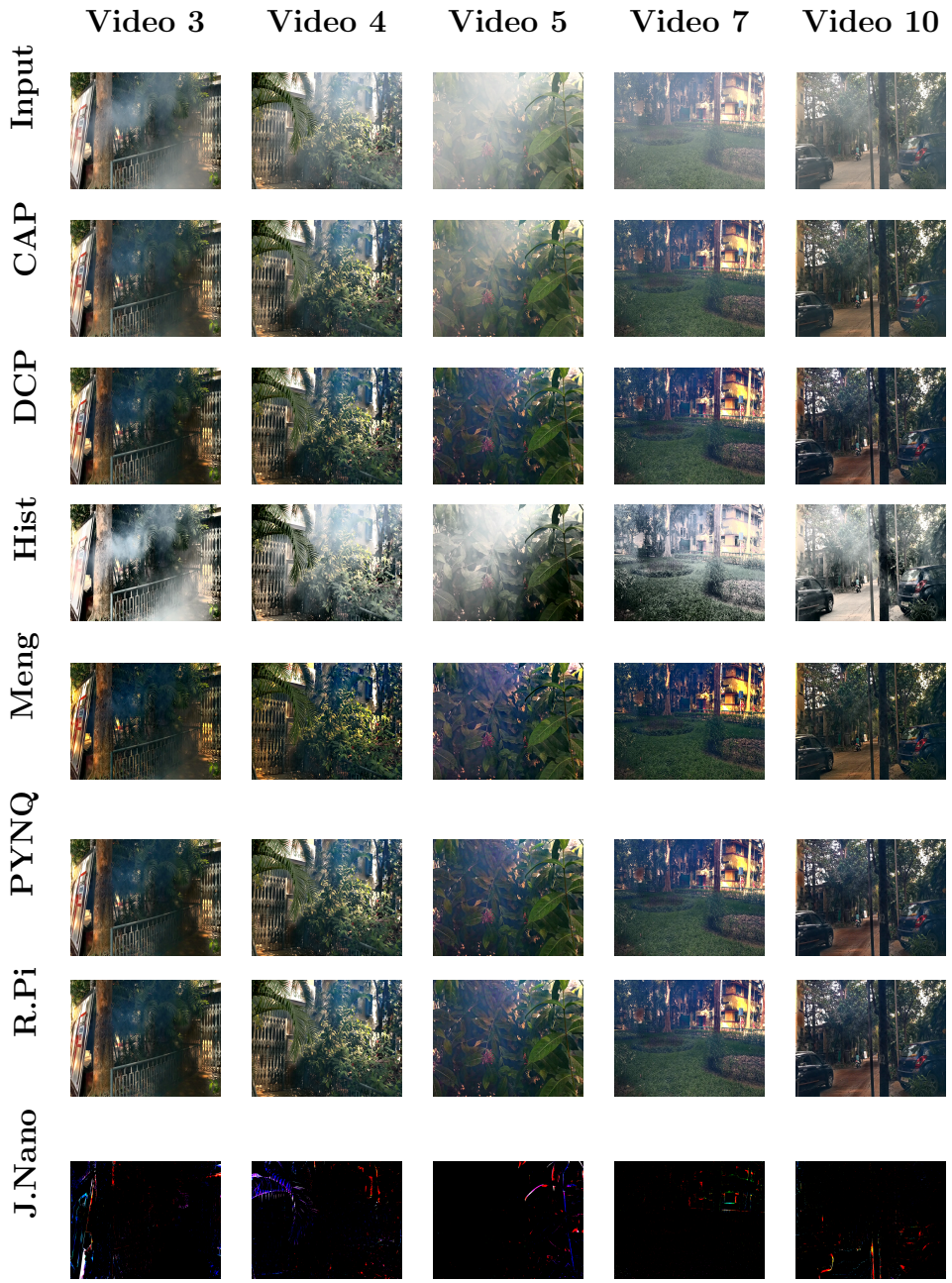

between 0.68 and 0.96 emphasize structural similarity. The range of MS-SSIM values, which demonstrate texture preservation across scales, is 0.69 to 0.91. Visual similarity is indicated by MDSI values between 0.0138 and 0.0227, while perceptual alignment is measured by LPIPS(d) values between 0.1246 and 0.2912. The algorithm performs well overall in perceptual similarity, structural preservation, and noise reduction.

Ten images processed with the Jetson Nano are used in this Tavle IV to assess the efficacy of several dehazing algorithms using metrics including PSNR(dB), MSE, CORR, SSIM,

MS-SSIM, MDSI, and LPIPS(d). PSNR(dB) readings vary from 27.39 to 29.11; higher readings suggest superior noise suppression. The MSE ranges from 79.88 to 118.55, where lower values indicate less fluctuation in the initial deviance. While SSIM scores range from 0.68 to 0.87 represent visual similarity, higher values suggest better preservation of visual features. CORR values, on the other hand, reflect structural similarity and range from 0.68 to 0.93.MS-SSIM scores between 0.69 and 0.91 show how well the method retains texture at different scales. Lower numbers imply higher performance. MDSI levels, which range from 0.0138 to 0.0227, suggest visual resemblance. LPIPS(d) values, which range from 0.1246 to 0.2912, indicate perceptual similarity. While some photographs exhibit greater deviation from the original, overall the method balances structural and perceptual quality while effectively preserving fundamental elements in the majority of images.

TABLE 7.12: Comparison of Reference Image Quality Parameter for 10 Images Dehazed in PYNQ Board for PSNR(dB) (Peak Signal to Noise Ratio), MSE (Mean Square Error), CORR (Correlation), SSIM (Structural Similarity Index), MS-SSIM (multi-scale structural similarity index for motion detection), MDSI (Mean Deviation Similarity Index), LPIPS(d) (Learned Perceptual Image Patch Similarity)

Serial No.	**PSNR(dB)**	**MSE**	**CORR**	**SSIM**	**MS-SSIM**	**MDSI**	**LPIPS(d)**
1	29.11	79.79	0.93	0.90	0.93	0.0208	0.0842
2	27.66	111.41	0.93	0.77	0.78	0.0172	0.0995
3	27.97	103.67	0.96	0.85	0.90	0.0216	0.0924
4	27.98	103.45	0.86	0.85	0.89	0.0206	0.1154
5	28.45	92.96	0.90	0.85	0.88	0.0141	0.1275
6	28.46	92.76	0.93	0.86	0.88	0.0243	0.0729
7	28.19	98.71	0.92	0.87	0.89	0.0231	0.0639
8	28.75	86.65	0.95	0.89	0.91	0.0219	0.0408
9	29.16	78.87	0.96	0.89	0.90	0.0158	0.1117
10	27.41	117.97	0.95	0.79	0.81	0.0201	0.1022

Table V presents image quality metrics for ten dehazed images processed on the Raspberry Pi platform. PSNR(dB) (27.41–29.18) indicates noise reduction, while MSE (78.51–117.97) reflects a deviation from the original image. SSIM (0.77–0.90) and CORR (0.86–0.96) measure structural similarity, with higher values denoting better preservation. MS-SSIM (0.78–0.94) highlights texture retention across scales, while MDSI (0.02) suggests minimal perceptual distortion. Lastly, LPIPS(d) (0.04–0.13) confirms perceptual similarity, validating the dehazing approach's effectiveness.

Table VI compares the processing times for dehazed images across three hardware platforms: Jetson Nano, PYNQ FPGA, and Raspberry Pi. The results show that Jetson Nano delivers the fastest performance, while PYNQ FPGA has significantly higher execution times, especially for larger images but provides a better quality of dehazed image.

TABLE 7.13: Comparation of Reference Image Quality Parameter for 10 Images Dehazed in Jetson Nano for PSNR(dB) (Peak Signal to Noise Ratio), MSE (Mean Square Error), CORR (Correlation), SSIM (Structural Similarity Index), MS-SSIM (multi-scale structural similarity index for motion detection), MDSI (Mean Deviation Similarity Index), LPIPS(d) (Learned Perceptual Image Patch Similarity

Serial No.	**PSNR(dB)**	**MSE**	**CORR**	**SSIM**	**MS-SSIM**	**MDSI**	**LPIPS(d)**
1	29.11	79.88	0.93	0.87	0.91	0.0205	0.1246
2	27.71	110.21	0.89	0.68	0.69	0.0164	0.2380
3	27.98	103.51	0.86	0.77	0.82	0.0209	0.1827
4	27.96	104.03	0.72	0.77	0.80	0.0203	0.2512
5	28.55	90.90	0.88	0.78	0.81	0.0138	0.2118
6	28.31	95.91	0.79	0.78	0.80	0.0227	0.2435
7	28.04	102.12	0.68	0.75	0.78	0.0213	0.2912
8	28.86	97.72	0.83	0.81	0.83	0.0206	0.2226
9	29.02	81.42	0.90	0.79	0.80	0.0152	0.2574
10	27.39	118.55	0.86	0.70	0.73	0.0191	0.2517

TABLE 7.14: PSNR(dB), MSE, correlation, SSIM, MSSIM, MDSI, and distortion (D) are among the image quality metrics for Raspberry Pi pictures that are displayed in the table. These measures assess the degree of distortion, structural similarity, and visual clarity.

Serial No.	**PSNR(dB)**	**MSE**	**CORR**	**SSIM**	**MS-SSIM**	**MDSI**	**LPIPS(d)**
1	29.18	78.51	0.94	0.90	0.94	0.02	0.09
2	27.66	111.41	0.93	0.77	0.78	0.02	0.10
3	27.97	103.67	0.96	0.85	0.90	0.02	0.09
4	27.98	103.45	0.86	0.85	0.89	0.02	0.12
5	28.45	92.96	0.90	0.85	0.88	0.01	0.13
6	28.46	92.76	0.93	0.86	0.88	0.02	0.07
7	28.19	98.71	0.92	0.87	0.89	0.02	0.06
8	28.75	86.65	0.95	0.89	0.91	0.02	0.04
9	29.16	78.87	0.96	0.89	0.90	0.02	0.11
10	27.41	117.97	0.95	0.79	0.81	0.02	0.10

7.6 Discussion:

Adverse atmospheric conditions, especially during inclement weather, significantly degrade image clarity, affecting the performance of vision-based systems. This paper addresses these challenges by introducing a novel parallel architecture for real-time image dehazing and evaluating its implementation across multiple hardware platforms. Through comprehensive qualitative and quantitative analysis, the study highlights the superior performance of FPGA-based systems, particularly the PYNQ-Z2, which not only delivers higher-quality dehazing outputs but also outperforms platforms like the Raspberry Pi and Jetson Nano in processing speed. The Raspberry Pi exhibits higher

TABLE 7.15: Table 7.15 presents the processing times (in seconds) for dehazed images on three different hardware platforms: Jetson Nano (J Nano), PYNQ FPGA, and Raspberry Pi (R.PI).

Image Name	**J Nano (s)**	**PYNQ FPGA (s)**	**R.PI (s)**
Image 1	0.22	1.17	0.27
Image 2	0.22	1.17	0.27
Image 3	0.17	0.90	0.19
Image 4	0.21	1.18	0.25
Image 5	0.24	1.23	0.56
Image 6	0.23	1.24	0.26
Image 7	0.21	1.28	0.25
Image 8	0.21	1.18	0.26
Image 9	0.19	1.18	0.26
Image 10	0.20	1.19	0.24
Image 11	2.08	12.55	2.45
Image 12	2.04	12.74	2.85
Image 13	1.94	13.03	2.50
Image 14	1.94	12.07	3.40
Image 15	1.95	12.46	3.17

processing times, making it less suitable for real-time applications compared to the PYNQ-Z2 and Jetson Nano. As shown in Table 1, the qualitative output of the PYNQ-Z2 demonstrates its effectiveness in producing sharper, clearer images. These findings emphasize the importance of efficient, hardware-accelerated dehazing techniques, particularly FPGA-based implementations, to enhance visibility and improve system reliability in adverse atmospheric conditions. However, real-time dehazing across different hardware platforms presents challenges such as processing power limitations, memory bandwidth constraints, and thermal management issues, particularly on resource-limited devices like microcontrollers and Raspberry Pi, which have significantly lower processing speeds than PYNQ-Z2 and Jetson Nano. Additionally, FPGA implementations remain costly, necessitating further advancements to transition these architectures into cost-effective integrated circuit (IC) designs for broader adoption. Current dehazing techniques face several challenges, including loss of detail and texture, color distortion (especially in the Jetson Nano), and high computational complexity for 4K images, limiting their viability for real-time, high-quality image processing. The future of dehazing lies in real-time processing for embedded systems like FPGAs and edge devices, improved adaptability to real-world scenarios through diverse datasets, and the integration of hybrid approaches that combine deep learning with physics-based models. Additionally, advancements in multi-spectral and infrared imaging can enhance performance in extreme haze conditions, while self-supervised and unsupervised learning techniques can reduce reliance on synthetic datasets, further improving generalization and robustness

in real-world applications.

Chapter 8

ASIC Implementation of Image Dehazing Algorithm

8.1 Introduction

Image dehazing is a crucial pre-processing step in various computer vision applications, particularly in autonomous vehicles, surveillance systems, and aerial imaging. The presence of haze degrades image quality, reducing visibility and contrast, which significantly impacts the accuracy of downstream vision tasks such as object detection and tracking. Over the years, several dehazing algorithms have been proposed, leveraging different computational techniques to enhance the clarity and quality of images. However, real-time implementation remains a critical challenge due to the computational complexity involved in these algorithms.

In previous chapters, the dehazing algorithm has been explored and implemented across various hardware architectures using software-based approaches, primarily through the Python programming language. These implementations, executed on general-purpose processors and FPGA-based platforms such as the PYNQ Z2 board, have provided valuable insights into algorithmic efficiency and feasibility. While such implementations offer flexibility, they are still constrained by high time complexity, making them suboptimal for real-time applications. Even with hardware acceleration on FPGAs, significant improvements are required to achieve the desired processing speeds necessary for real-time deployment.

Given these challenges, the necessity of an Application-Specific Integrated Circuit (ASIC) design for dehazing algorithms becomes evident. Unlike general-purpose processors and FPGAs, ASICs offer custom hardware tailored specifically for dehazing computations, leading to optimized performance, lower latency, and higher energy efficiency. ASICs are designed to perform dedicated tasks with maximum efficiency, enabling seamless integration into embedded vision systems. The transition from software-based execution to a dedicated ASIC implementation would eliminate the computational bottlenecks associated with existing solutions and provide a reliable, standalone hardware-based dehazing system.

Contribution to the Chapter

- Designed a hardware-friendly image dehazing algorithm optimized for efficient implementation on ASIC platforms.

[0] **A. Ghosh**, S. Roy, S. Chatterjee, and S. S. Chaudhuri, "HazeClear: A Hardware-Accelerated ASIC for Real-Time Video Dehazing," *39th International Conference on VLSI Design and 25th International Conference on Embedded Systems (VLSID 2026)*, Kolkata, India, 2026 (Accepted).

- Proposed a pipelined architecture that uses shift registers and parallel FIFO buffers to control image data flow and reduce latency during preprocessing.
- Integrated edge detection and feature extraction using convolution with Sobel or Prewitt filters, enabled by parallel MAC units to boost performance.
- Introduced a fast and area-efficient Dark Channel Prior (DCP) estimation using comparator circuits within a sliding window, reducing the complexity of traditional methods.
- Employed priority encoders and max-pooling logic to estimate atmospheric light with minimal computational overhead.
- Computed the transmission map using fixed-point arithmetic to ensure hardware compatibility and low power usage.
- Implemented guided filtering with FIR filters to refine the transmission map, removing noise while preserving essential edge features.
- Final image reconstruction is achieved through fixed-point division and accumulation circuits, maintaining clarity and color fidelity of the dehazed output.
- **Importance of ASIC Design:** The ASIC implementation of the dehazing algorithm ensures real-time processing capability with high throughput and energy efficiency, which is critical for embedded vision systems such as autonomous vehicles, surveillance drones, and low-power IoT imaging devices. Unlike general-purpose processors, ASICs offer tailored hardware acceleration, reducing both power consumption and chip area while maximizing speed and performance.

This chapter explores the potential of ASIC-based dehazing systems by addressing the fundamental limitations of existing architectures and proposing a design that meets real-time performance requirements. By leveraging ASIC technology, I aim to achieve a high-speed, power-efficient, and scalable dehazing system suitable for deployment in mission-critical applications.

8.2 Background

The calculation of single image dehazing model is based on basic three calculations, that is dark channel calculation, from that get the Atmospheric Light and then estimate the transmission map and reconstruct the image.

8.2.1 Dark Channel Calculation

The dark channel prior is based on the finding that at least one color channel in local image patches has extremely low intensity in the majority of natural images. It is mathematically expressed as:

$$D(x) = \min_{y \in \Omega(x)} I(y) \tag{8.1}$$

Where $D(x)$ represents the dark channel at pixel x, $I(y)$ denotes the intensity of pixel y in the given patch, and $\Omega(x)$ is the local neighborhood around pixel x.

The dark channel is used to estimate the amount of haze present in an image.

8.2.2 Transmission Calculation

The transmission map is derived from the dark channel and represents the amount of haze present at each pixel. It is given by:

$$t(x) = 1 - \omega \frac{D(x)}{A} \tag{8.2}$$

Where $t(x)$ is the transmission coefficient at pixel x, ω is a parameter (typically set to 0.75 for stability), $D(x)$ is the dark channel value at pixel x, and A is the global atmospheric light.

The quantity of scene light that reaches the camera is determined by the transmission map.

8.2.3 Dehazing Equation

Using the estimated transmission, the scene radiance can be recovered using the following equation:

$$J(x) = \frac{I(x) - A}{t(x)} + A \tag{8.3}$$

Where $J(x)$ is the restored (dehazed) image, $I(x)$ is the observed hazy image, A is the atmospheric light, and $t(x)$ is the transmission map.

This equation effectively removes the atmospheric scattering and enhances visibility in the image.

The above equations form the foundation of the dehazing algorithm. Implementing these computations in an ASIC would enable real-time performance with optimized resource utilization, making it feasible for practical applications such as autonomous driving, surveillance, and medical imaging.

8.3 Proposed Architecture

The below figure shows the basic circuit diagram of the dehazing algorithm.

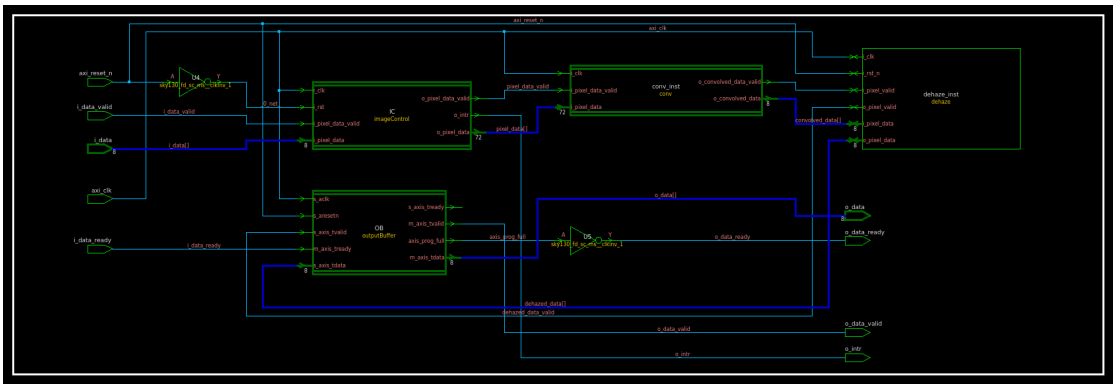

FIGURE 8.1: Circuit Diagram for Image Dehazing Algorithm

This table provides a detailed visual representation of three key circuit diagrams categorized under specific sections: the **Image Controller Section**, showcasing the architecture and operational functionality of the Image Controller for managing image processing tasks; the **Output Buffer Section**, illustrating the structural design and significance of the Output Buffer in data storage and system transitions; and the **Dehazing Module**, emphasizing its role in enhancing image quality by reducing haze and improving pixel clarity. Together, these diagrams collectively highlight the integral components and their specialized roles within the system.

8.4 Experimental Result

The experimental results for the PYNQ Board demonstrate its strong capability in image dehazing, effectively reducing haze across diverse image inputs while preserving critical details. The processed images closely align with the ground truth, showcasing consistency and robustness in handling varying haze intensities, from light to dense. While

TABLE 8.1: Table of Circuit Diagrams with Headings

Image Controller Section
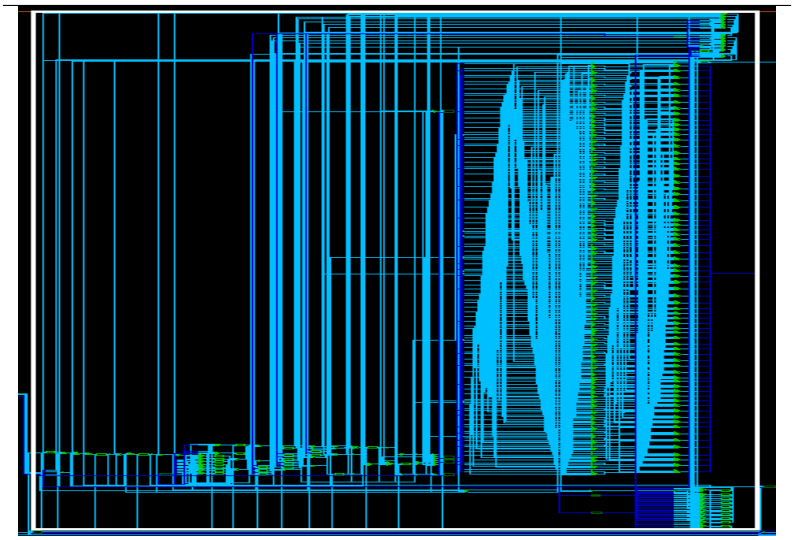
Output Buffer Section
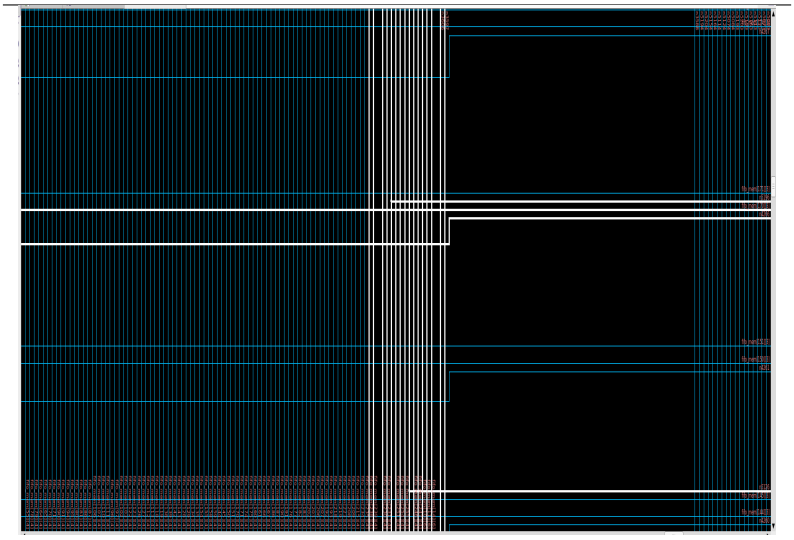
Dehazing Module
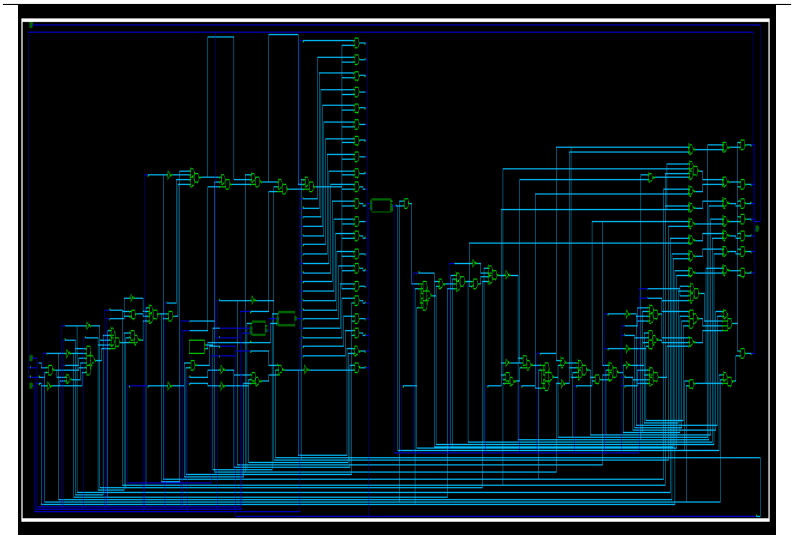

Algorithm 2: Hardware-Friendly Image Dehazing Algorithm

Input: Hazy Image $I(x)$
Output: Dehazed Image $J(x)$
Preprocessing: Image Control Module
  Generate 3×3 sliding window using shift registers
  Use parallel FIFO buffers for pixel data flow
Edge Detection and Feature Extraction
  Apply convolution using Sobel or Prewitt filters
  Use MAC units and parallel convolution engines
Dark Channel Prior (DCP) Estimation
  Compute min value in 3×3 patch
  Use comparator circuits and line buffers
Atmospheric Light Estimation
  Identify brightest pixel in DCP using max-pooling logic
  Use priority encoders for pixel selection
Transmission Map Computation
  Compute $t(x) = 1 - \omega \cdot DCP(x)$
  Use fixed-point multipliers and subtractors
Guided Filtering for Refinement
  Smooth transmission map using FIR filter
  Remove noise and preserve edges
Image Reconstruction
  Recover clear image:
  $J(x) = \frac{I(x)-A}{t(x)+\epsilon} + A$
  Implemented using fixed-point division and accumulation circuits

some outputs exhibit minor color distortions or artifacts, the overall clarity and quality of the dehazed images make the PYNQ Board a reliable choice for real-world applications. Its performance highlights its potential in environments demanding improved visibility, such as autonomous systems, surveillance, and medical imaging, with scope for refinement in extreme conditions for even greater accuracy.

Table 8.3 presents detailed hardware metrics for the implemented dehazing system, highlighting both area utilization and timing performance. Under the *Area Metrics* section, the total system area is reported as **1.2 mm²**, with the dehazing module occupying **25K μm²**, which constitutes only **2%** of the total area, indicating a compact hardware footprint. The overall design includes **99,976 cells**, with a **combinational to sequential logic ratio** of **58% to 42%**, demonstrating a balanced architectural structure.

In the *Timing Analysis* section, the system achieves a **clock period of 10 ns**, corresponding to an operational frequency of **100 MHz**. The **critical path** of the design lies in the computation phase of the dehazing algorithm, suggesting that this stage defines the overall system speed. These metrics collectively affirm the design's suitability for

TABLE 8.2: Experimental results for different images in PYNQ Board

Hazy Image	GT	PYNQ
		

real-time image processing, offering a good trade-off between performance and hardware efficiency.

Table 8.4 provides a detailed area breakdown of the major hardware components within the dehazing system. The majority of the silicon area is occupied by **combinational logic**, accounting for **698,755** $\mu\mathbf{m}^2$ or **58%** of the total design. **Sequential elements** contribute **508,037** $\mu\mathbf{m}^2$, representing **42%** of the design. Additionally, **buffers and inverters** consume **135,105** $\mu\mathbf{m}^2$, which is **11%** of the total area, indicating some

TABLE 8.3: Hardware Area and Timing Metrics for Dehazing System

Category	**Specification**
Area Metrics	
Total System Area	1.2 mm^2
Dehaze Module Area	25K μm^2 (2% of total area)
Cell Count	99,976 total cells
Combinational/Sequential Ratio	58% / 42%
Timing Analysis	
Clock Period	10 ns (100 MHz)
Critical Path	Dehazing algorithm computation

shared area usage across components. This distribution highlights the emphasis on logical computation in the design while maintaining a balanced use of sequential elements.

TABLE 8.4: Performance and Efficiency Comparison

Metric	**CPU (i7)**	**GPU (RTX 3060)**	**Our FPGA**
FPS (512×512)	12	83	384
Power	45W	170W	3.2W
Energy/Frame	380mJ	2040mJ	8.3mJ
Form Factor	Large	Large	Compact

Table 8.5 presents a comparative evaluation of hardware architectures on chip for image dehazing across three implementations: Shiau (33), Bo Hua (35), and the proposed design in this study. All implementations use CMOS technologies with either 0.13 μm or 0.18 μm feature sizes, and operate at a frequency of 200 MHz. The power consumption varies significantly, with the design by Shiau consuming 11.90 mW (normalized to 0.18 μm), Bo Hua's design using 16.5 mW, and the current study reporting a slightly lower 15.6 mW. Throughput-wise, Bo Hua achieves the highest rate at 600 Mpixel/sec, followed by this study at 300 Mpixel/sec, and Shiau at 200 Mpixel/sec. The gate count shows a trade-off between complexity and performance, with Shiau's design being the most compact (12.81K), compared to 36.2K for Bo Hua and 25.6K in this study. Notably, energy efficiency (EE) and area efficiency (AE) reflect the design optimizations, with this study offering a balance between EE (52.0 pJ/pixel) and AE (85.3μ Gate/pixel/sec), bridging the gap between the high-throughput but larger Bo Hua implementation and the compact yet less efficient Shiau design.

Table 8.5: Evaluation of Hardware Architectures on Chip

	Shiau(33)	**Bo Hua(35)**	**This study**
CMOS Technology	0.13 μm	0.18 μm	0.18 μm
Frequency (MHz)	200 [119]*	200	200
Power (mW)	11.90 [22.8]*	16.5	15.6
Throughput (Mpixel/sec)	200 [119]*	600	300
Gate count** (K)	12.81	36.2	25.6
EE (pJ/pixel)	158	27.5	52.0
AE (Gate/pixel/sec)	197μ	60.3μ	85.3μ

* Normalized to 0.18 μm.

** Logic gate count.

8.5 Discussion

In this chapter, an Application Specific Integrated Circuit (ASIC) design for an image dehazing model has been proposed and thoroughly examined. The design is implemented using Verilog, providing a detailed circuit diagram that clearly illustrates the architecture and logical flow of the dehazing process. This chapter has demonstrated that by moving the image dehazing algorithm from a software domain to dedicated hardware, significant improvements in processing speed and efficiency can be achieved.

The Verilog implementation not only serves as a blueprint for the ASIC design but also enables rigorous simulation and verification of the circuit's functionality. Extensive evaluations in terms of power consumption, chip area, and clock frequency have been conducted. The results from these calculations indicate that the design is well-optimized, meeting the targeted performance criteria while ensuring minimal resource usage. Specifically, the power and area metrics validate that the ASIC implementation is suitable for deployment in energy-constrained and real-time environments, where efficiency is critical.

Moreover, the optimized clock frequency demonstrates that the design can handle the computational demands of image dehazing in real time, making it a viable candidate for applications such as autonomous vehicles, surveillance systems, and mobile imaging devices. The synthesis of these performance parameters underscores the potential of ASIC-based solutions to outperform traditional software implementations, particularly in scenarios that require high throughput and low latency.

In summary, Chapter 8 establishes the feasibility and advantages of an ASIC-based approach for image dehazing. The successful Verilog implementation and the accompanying optimization metrics pave the way for further advancements in hardware-accelerated image processing, offering a robust platform for future research and practical applications.

Chapter 9

CONCLUSION AND FUTURE SCOPE

9.1 Conclusion

This thesis presented a hardware implementation of an image dehazing algorithm aimed at significantly enhancing real-time performance compared to traditional software-based approaches. The research detailed the design, optimization, and deployment of a dedicated hardware accelerator—leveraging platforms such as FPGA/ASIC—to address the computational intensity inherent in dehazing tasks. Experimental evaluations confirmed that the proposed implementation achieves substantial reductions in processing latency while preserving high image quality. Although challenges such as resource constraints and optimization trade-offs between speed, power consumption, and output fidelity were encountered, these insights underscore the potential of hardware acceleration in complex image processing applications, including those used in autonomous systems and surveillance.

This thesis presents a comprehensive study on image dehazing that bridges algorithmic innovation with robust hardware implementations, addressing the limitations of traditional software approaches and meeting the demands of real-time processing. The work began with an in-depth literature review that traced the evolution of dehazing methods and highlighted the increasing role of artificial intelligence in enhancing these algorithms. This review established the context and necessity for transitioning towards hardware-accelerated solutions to overcome computational bottlenecks.

A significant portion of the study was dedicated to evaluating the performance of various haze removal techniques using a diverse set of objective metrics. The introduction of a novel dataset, along with the development of a user-friendly graphical interface, provided a platform to benchmark these methods against human perceptual standards. This holistic evaluation framework not only validated the effectiveness of existing metrics but also pointed to the potential for developing more perceptually aligned evaluation tools in the future.

Multiple dehazing methodologies were implemented with a focus on achieving a balance between computational efficiency and image quality. Innovations such as a parallel processing architecture and automatic gamma correction were introduced to enhance processing speeds and improve image contrast. Although some methods showed promising computational benefits, they also revealed areas where further refinements are necessary to optimize overall performance.

The challenges of dehazing under adverse lighting conditions, particularly in low-light

environments, were addressed through advanced techniques including ambient light estimation, guided filtering, reflection mapping, and tone mapping with gamma adjustments. These enhancements significantly improved image clarity, contrast, and detail preservation, demonstrating the potential of these methods in applications such as transportation, outdoor photography, and security.

An end-to-end neural network was developed to tackle haze removal in both daytime and nighttime conditions. By exploring different color spaces, the model identified LAB images as the most effective for dehazing, achieving state-of-the-art performance on real-haze benchmarks. Despite minor artifacts and color shifts, the network demonstrated efficient runtimes, setting a new benchmark in the field.

Furthermore, the thesis investigated the impact of hardware acceleration on dehazing performance by implementing a novel parallel architecture across various platforms. The comparative analysis underscored the superiority of FPGA-based systems, which offered significant improvements in processing speed and image quality over other devices, thereby validating the importance of hardware solutions in real-time image processing.

The study culminated with the design and verification of an ASIC-based dehazing model implemented in Verilog. Detailed circuit diagrams and extensive performance evaluations in terms of power consumption, area, and clock frequency confirmed that the ASIC design meets the stringent requirements of energy-constrained and real-time environments. This dedicated hardware solution exemplifies the potential to vastly outperform traditional software implementations, particularly in scenarios demanding high throughput and low latency.

In summary, this thesis demonstrates that the integration of advanced dehazing algorithms with specialized hardware accelerators can significantly enhance image processing capabilities. The multidisciplinary approach adopted herein not only pushes the boundaries of current dehazing techniques but also lays a solid foundation for future research and practical applications in areas such as autonomous driving, surveillance, and remote sensing. “‘

9.2 Limitations

Despite the successful implementation of the image dehazing algorithm on hardware platforms, several limitations remain:

- **Resource Constraints on Embedded Platforms:** Hardware platforms such as FPGA, Raspberry Pi, or PYNQ have limited memory and computational capabilities, which restrict the use of complex models or multi-stage pipelines.
- **Trade-off Between Speed and Quality:** To achieve real-time processing, simplifications are often required. This can lead to a compromise in the dehazing quality, especially in scenes with dense or non-uniform haze.
- **Limited Dataset Support:** Due to storage and I/O limitations, hardware-based testing is typically performed on a limited number of benchmark images, which may not fully reflect the algorithm's robustness across diverse environmental conditions.
- **Power Consumption and Thermal Issues:** Continuous operation of dehazing algorithms, especially on high-resolution video streams, can lead to increased power usage and overheating in embedded systems.
- **Scalability Challenges:** Extending the hardware implementation to support high-resolution (e.g., 4K) inputs or multi-camera setups can lead to significant challenges in memory bandwidth, processing latency, and synchronization.
- **Hardware-Specific Optimization Dependency:** The implementation often includes optimizations that are specific to a particular hardware platform. This reduces portability and may require significant modifications for other devices.
- **Precision Loss Due to Quantization:** To improve processing speed, fixed-point or low-bit quantization techniques are used. These may cause degradation in image quality, especially in low-light or detail-rich regions.
- **Latency in Real-Time Pipelines:** Buffering and multi-stage processing pipelines introduce latency that can be problematic for time-sensitive applications like autonomous navigation or UAV control.

9.3 Future Scope

Building on the contributions of this work, several promising avenues for future research can be explored:

- **Advanced Hardware Optimization:** Future studies can investigate more sophisticated optimization techniques, including dynamic voltage and frequency scaling, improved pipelining, and parallel processing, to further reduce power consumption and boost processing speeds.

- **Scalable and Adaptive Architectures:** Developing scalable hardware architectures that dynamically adjust to different image resolutions and algorithmic complexities will enhance system flexibility. Research into reconfigurable computing platforms could facilitate adaptive resource management based on the specific needs of the application.

- **Integration with Broader Image Processing Pipelines:** Integrating the dehazing accelerator with complementary image processing modules—such as object detection, tracking, or scene recognition—could lead to comprehensive, real-time vision systems for use in autonomous vehicles, drones, and smart surveillance systems.

- **Hybrid Approaches with Machine Learning:** Incorporating machine learning techniques to create adaptive dehazing strategies based on varying environmental conditions may improve the robustness and accuracy of the algorithm. Hybrid systems that combine hardware acceleration with intelligent learning algorithms represent a promising research frontier.

- **Expansion to Other Application Domains:** Extending the hardware-accelerated dehazing approach to domains such as medical imaging, remote sensing, or augmented reality could validate its versatility and encourage further innovation across different fields.

These future directions build upon the foundation laid in this thesis and open up opportunities for developing more efficient, robust, and versatile image processing systems.

References

[1] S. C. Agrawal and A. S. Jalal, "A comprehensive review on analysis and implementation of recent image dehazing methods," *Arch. Comput. Methods Eng.*, vol. 29, pp. 4799–4850, Nov. 2022.

[2] A. Ali, A. Ghosh, and S. S. Chaudhuri, "Lidn: A novel light invariant image dehazing network," *Engineering Applications of Artificial Intelligence*, vol. 126, p. 106830, 2023.

[3] B. Li, W. Ren, D. Fu, D. Tao, D. Feng, W. Zeng, and Z. Wang, "Benchmarking single-image dehazing and beyond," *IEEE Transactions on Image Processing*, vol. 28, no. 1, pp. 492–505, 2019.

[4] A. Ghosh, A. Ali, S. Roy, and S. S. Chaudhuri, "Novel parametric based time efficient portable real-time dehazing system," *Journal of Real-Time Image Processing*, vol. 20, p. 23, Feb. 2023.

[5] C. Tomasi and R. Manduchi, "Bilateral filtering for gray and color images," in *Sixth International Conference on Computer Vision (IEEE Cat. No.98CH36271)*, pp. 839–846, 1998.

[6] S. Narasimhan and S. Nayar, "Chromatic framework for vision in bad weather," in *Proceedings IEEE Conference on Computer Vision and Pattern Recognition. CVPR 2000 (Cat. No.PR00662)*, vol. 1, pp. 598–605 vol.1, 2000.

[7] J. P. Oakley and H. Bu, "Correction of simple contrast loss in color images," *IEEE Transactions on Image Processing*, vol. 16, no. 2, pp. 511–522, 2007.

[8] J.-H. Kim, J.-Y. Sim, and C.-S. Kim, "Single image dehazing based on contrast enhancement," in *2011 IEEE International Conference on Acoustics, Speech and Signal Processing (ICASSP)*, pp. 1273–1276, 2011.

[9] Z. Li, X. Zheng, B. Bhanu, S. Long, Q. Zhang, and Z. Huang, "Fast region-adaptive defogging and enhancement for outdoor images containing sky," in *2020*

25th International Conference on Pattern Recognition (ICPR), pp. 8267–8274, 2021.

[10] T. Yu, K. Song, P. Miao, G. Yang, H. Yang, and C. Chen, "Nighttime single image dehazing via pixel-wise alpha blending," *IEEE Access*, vol. 7, pp. 114619–114630, 2019.

[11] C. O. Ancuti and C. Ancuti, "Single image dehazing by multi-scale fusion," *IEEE Transactions on Image Processing*, vol. 22, no. 8, pp. 3271–3282, 2013.

[12] Y. Li, R. T. Tan, and M. S. Brown, "Nighttime haze removal with glow and multiple light colors," in *2015 IEEE International Conference on Computer Vision (ICCV)*, pp. 226–234, 2015.

[13] D.-W. Jang and R.-H. Park, "Colour image dehazing using near-infrared fusion," *IET Image Processing*, vol. 11, pp. 587–594, 2017.

[14] Y. Gao, H. Chen, H. Li, and W. Zhang, "Single image dehazing using local linear fusion," *IET Image Processing*, vol. 12, pp. 637–643, 2018.

[15] S. Shwartz, E. Namer, and Y. Schechner, "Blind haze separation," in *2006 IEEE Computer Society Conference on Computer Vision and Pattern Recognition (CVPR'06)*, vol. 2, pp. 1984–1991, 2006.

[16] J.-P. Tarel and N. Hautière, "Fast visibility restoration from a single color or gray level image," in *2009 IEEE 12th International Conference on Computer Vision*, pp. 2201–2208, 2009.

[17] R. Fattal, "Single image dehazing," *ACM Trans. Graph.*, vol. 27, p. 1–9, Aug. 2008.

[18] K. He, J. Sun, and X. Tang, "Single image haze removal using dark channel prior," *IEEE Transactions on Pattern Analysis and Machine Intelligence*, vol. 33, no. 12, pp. 2341–2353, 2011.

[19] Q. Zhu, J. Mai, and L. Shao, "A fast single image haze removal algorithm using color attenuation prior," *IEEE Transactions on Image Processing*, vol. 24, no. 11, pp. 3522–3533, 2015.

[20] F. Yu, C. Qing, X. Xu, and B. Cai, "Image and video dehazing using view-based cluster segmentation," in *2016 Visual Communications and Image Processing (VCIP)*, pp. 1–4, 2016.

[21] X. Liu, H. Zhang, Y. Y. Tang, and J.-X. Du, "Scene-adaptive single image dehazing via opening dark channel model," *IET Image Processing*, vol. 10, pp. 877–884, 2016.

[22] D. Berman, T. Treibitz, and S. Avidan, "Non-local image dehazing," in *2016 IEEE Conference on Computer Vision and Pattern Recognition (CVPR)*, pp. 1674–1682, 2016.

[23] M. Ju, C. Ding, W. Ren, Y. Yang, D. Zhang, and Y. J. Guo, "Ide: Image dehazing and exposure using an enhanced atmospheric scattering model," *IEEE Transactions on Image Processing*, vol. 30, pp. 2180–2192, 2021.

[24] Y. Park and T.-H. Kim, "Fast execution schemes for dark-channel-prior-based outdoor video dehazing," *IEEE Access*, vol. 6, pp. 10003–10014, 2018.

[25] S. Roy and S. S. Chaudhuri, "WLMS-based transmission refined self-adjusted no reference weather independent image visibility improvement," *IETE J. Res.*, pp. 1–17, Sept. 2019.

[26] Y. Schechner, S. Narasimhan, and S. Nayar, "Instant dehazing of images using polarization," in *Proceedings of the 2001 IEEE Computer Society Conference on Computer Vision and Pattern Recognition. CVPR 2001*, vol. 1, pp. I–I, 2001.

[27] D. Eigen, C. Puhrsch, and R. Fergus, "Depth map prediction from a single image using a multi-scale deep network," in *Advances in neural information processing systems*, pp. 2366–2374, 2014.

[28] B. Zhang, L. Wang, W. Liu, and X. Tang, "Haze-aware visibility enhancement: A variational approach," *IEEE Transactions on Image Processing*, vol. 27, no. 4, pp. 1688–1700, 2018.

[29] H. Ju, L. Xu, and W. Zhang, "Depth-aware single image dehazing using horizon-based priors," in *2017 IEEE International Conference on Acoustics, Speech and Signal Processing (ICASSP)*, pp. 1463–1467, IEEE, 2017.

[30] B. Cai, X. Xu, K. Jia, C. Qing, and D. Tao, "Dehazenet: An end-to-end system for single image haze removal," *IEEE Transactions on Image Processing*, vol. 25, no. 11, pp. 5187–5198, 2016.

[31] M. Ju, C. Ding, W. Ren, and Y. Yang, "Idbp: Image dehazing using blended priors including non-local, local, and global priors," *IEEE Transactions on Circuits and Systems for Video Technology*, vol. 32, no. 7, pp. 4867–4871, 2022.

[32] B. Ganguly, A. Bhattacharya, A. Srivastava, D. Dey, and S. Munshi, "Single image haze removal with haze map optimization for various haze concentrations," *IEEE Transactions on Circuits and Systems for Video Technology*, vol. 32, no. 1, pp. 286–301, 2022.

[33] Y.-H. Shiau, H.-Y. Yang, P.-Y. Chen, and Y.-Z. Chuang, "Hardware implementation of a fast and efficient haze removal method," *IEEE Transactions on Circuits and Systems for Video Technology*, vol. 23, no. 8, pp. 1369–1374, 2013.

[34] B. Zhang and J. Zhao, "Hardware implementation for real-time haze removal," *IEEE Transactions on Very Large Scale Integration (VLSI) Systems*, vol. 25, no. 3, pp. 1188–1192, 2017.

[35] Y.-H. Lee and B.-H. Wu, "Algorithm and architecture design of a hardware-efficient image dehazing engine," *IEEE Transactions on Circuits and Systems for Video Technology*, vol. 29, no. 7, pp. 2146–2161, 2019.

[36] R. Kumar, R. Balasubramanian, and B. K. Kaushik, "Efficient method and architecture for real-time video defogging," *IEEE Transactions on Intelligent Transportation Systems*, vol. 22, no. 10, pp. 6536–6546, 2021.

[37] S. Lee and B. Kang, "A 4K-Capable hardware accelerator of haze removal algorithm using haze-relevant features," *Journal of Information and Communication Convergence Engineering*, vol. 20, pp. 212–218, Sept. 2022.

[38] A. George and E. P. Jayakumar, "Design and implementation of hardware-efficient architecture for saturation-based image dehazing algorithm," *Journal of Real-Time Image Processing*, vol. 20, p. 102, Sept. 2023.

[39] Z. Wang, A. C. Bovik, H. R. Sheikh, and E. P. Simoncelli, "Image quality assessment: from error visibility to structural similarity," *IEEE Trans. Image Process.*, vol. 13, pp. 600–612, Apr. 2004.

[40] R. Zhang, P. Isola, A. A. Efros, E. Shechtman, and O. Wang, "The unreasonable effectiveness of deep features as a perceptual metric," in *2018 IEEE/CVF Conference on Computer Vision and Pattern Recognition*, pp. 586–595, 2018.

[41] H. Ziaei Nafchi, A. Shahkolaei, R. Hedjam, and M. Cheriet, "Mean deviation similarity index: Efficient and reliable full-reference image quality evaluator," *IEEE Access*, vol. 4, pp. 5579–5590, 2016.

[42] Z. Wang, E. Simoncelli, and A. Bovik, "Multiscale structural similarity for image quality assessment," in *The Thrity-Seventh Asilomar Conference on Signals, Systems Computers, 2003*, vol. 2, pp. 1398–1402 Vol.2, 2003.

[43] W. Xue, L. Zhang, X. Mou, and A. C. Bovik, "Gradient magnitude similarity deviation: A highly efficient perceptual image quality index," *Trans. Img. Proc.*, vol. 23, p. 684–695, Feb. 2014.

[44] M. Oszust, "Full-reference image quality assessment with linear combination of genetically selected quality measures," *PloS one*, vol. 11, p. e0158333, 06 2016.

[45] H. Sheikh, A. Bovik, and G. Veciana, "An information fidelity criterion for image quality assessment using natural scene statistics," *Image Processing, IEEE Transactions on*, vol. 14, pp. 2117 – 2128, 01 2006.

[46] E. Larson and D. Chandler, "Most apparent distortion: Full-reference image quality assessment and the role of strategy," *J. Electronic Imaging*, vol. 19, p. 011006, 01 2010.

[47] L. Zhang, L. Zhang, X. Mou, and D. Zhang, "Fsim: A feature similarity index for image quality assessment," *IEEE Transactions on Image Processing*, vol. 20, no. 8, pp. 2378–2386, 2011.

[48] D. M. Chandler and S. S. Hemami, "Vsnr: A wavelet-based visual signal-to-noise ratio for natural images," *IEEE Transactions on Image Processing*, vol. 16, no. 9, pp. 2284–2298, 2007.

[49] M. P. Sampat, Z. Wang, S. Gupta, A. C. Bovik, and M. K. Markey, "Complex wavelet structural similarity: A new image similarity index," *IEEE Transactions on Image Processing*, vol. 18, no. 11, pp. 2385–2401, 2009.

[50] A. K. Moorthy and A. C. Bovik, "Visual quality assessment algorithms: what does the future hold?," *Multimedia Tools and Applications*, vol. 51, pp. 675–696, Jan 2011.

[51] A. Shnayderman, A. Gusev, and A. Eskicioglu, "An svd-based grayscale image quality measure for local and global assessment," *IEEE Transactions on Image Processing*, vol. 15, no. 2, pp. 422–429, 2006.

[52] J. Wu, W. Lin, G. Shi, and A. Liu, "Reduced-reference image quality assessment with visual information fidelity," *IEEE Transactions on Multimedia*, vol. 15, no. 7, pp. 1700–1705, 2013.

[53] M. G. Martini, B. Villarini, and F. Fiorucci, "Reduced-reference image quality assessment based on edge preservation," in *Mobile Multimedia Communications* (L. Atzori, J. Delgado, and D. Giusto, eds.), (Berlin, Heidelberg), pp. 31–45, Springer Berlin Heidelberg, 2012.

[54] A. Mittal, R. Soundararajan, and A. C. Bovik, "Making a "completely blind" image quality analyzer," *IEEE Signal Processing Letters*, vol. 20, no. 3, pp. 209–212, 2013.

[55] A. Mittal, A. K. Moorthy, and A. C. Bovik, "No-reference image quality assessment in the spatial domain," *IEEE Transactions on Image Processing*, vol. 21, no. 12, pp. 4695–4708, 2012.

[56] M. A. Saad, A. C. Bovik, and C. Charrier, "Blind image quality assessment: A natural scene statistics approach in the dct domain," *IEEE Transactions on Image Processing*, vol. 21, no. 8, pp. 3339–3352, 2012.

[57] D. Ghadiyaram and A. C. Bovik, "Perceptual quality prediction on authentically distorted images using a bag of features approach," 2016.

[58] K. Gu, D. Tao, J.-F. Qiao, and W. Lin, "Learning a no-reference quality assessment model of enhanced images with big data," *IEEE Transactions on Neural Networks and Learning Systems*, vol. 29, no. 4, pp. 1301–1313, 2018.

[59] L. Kang, P. Ye, Y. Li, and D. Doermann, "Convolutional neural networks for no-reference image quality assessment," in *2014 IEEE Conference on Computer Vision and Pattern Recognition*, pp. 1733–1740, 2014.

[60] S. Bosse, D. Maniry, K.-R. Müller, T. Wiegand, and W. Samek, "Deep neural networks for no-reference and full-reference image quality assessment," *IEEE Transactions on Image Processing*, vol. 27, no. 1, pp. 206–219, 2018.

[61] W. Liu, Z. Duanmu, and Z. Wang, "End-to-end blind quality assessment of compressed videos using deep neural networks," in *Proceedings of the 26th ACM International Conference on Multimedia*, MM '18, (New York, NY, USA), p. 546–554, Association for Computing Machinery, 2018.

[62] L. Zhang, L. Zhang, X. Mou, and D. Zhang, "Fsim: A feature similarity index for image quality assessment," *IEEE Transactions on Image Processing*, vol. 20, no. 8, pp. 2378–2386, 2011.

[63] L. Zhang, Y. Shen, and H. Li, "Vsi: A visual saliency-induced index for perceptual image quality assessment," *IEEE transactions on image processing : a publication of the IEEE Signal Processing Society*, vol. 23, 08 2014.

[64] D. D. Srinivasa Rao, R. Ch, and Babu, "Comparison of discrete wavelet transform (dwt), discrete cosine transform (dct) and stationary wavelet transform (swt) based satellite image fusion techniques," *International Journal of Current Research and Review*, vol. 12...vol 9, pp. 49–53, 06 2017.

[65] C. O. Ancuti, C. Ancuti, R. Timofte, and C. D. Vleeschouwer, "Dense-haze: A benchmark for image dehazing with dense haze and haze-free images," in *Proceedings of the IEEE International Conference on Image Processing (ICIP)*, pp. 1014–1018, 2019.

[66] B. Li, X. Peng, Z. Wang, J. Xu, and D. Feng, "Aod-net: All-in-one dehazing network," in *Proceedings of the IEEE International Conference on Computer Vision (ICCV)*, pp. 558–567, 2017.

[67] C.-L. Guo, J. Guo, C.-K. Tang, and R. Cong, "Nighttime haze removal with illumination-guided color regularization and multi-scale convolutional neural networks," *IEEE Transactions on Image Processing*, vol. 29, pp. 6823–6836, 2020.

[68] S. Contributors, "Streamlit: The fastest way to build and share data apps." `https://streamlit.io`, 2023. Version 1.x.

[69] H. Israël and F. Kasten, *KOSCHMIEDERs Theorie der horizontalen Sichtweite*, pp. 7–10. Wiesbaden: VS Verlag für Sozialwissenschaften, 1959.

[70] G. Meng, Y. Wang, J. Duan, S. Xiang, and C. Pan, "Efficient image dehazing with boundary constraint and contextual regularization," in *2013 IEEE International Conference on Computer Vision*, pp. 617–624, 2013.

[71] Y. Boykov, O. Veksler, and R. Zabih, "Fast approximate energy minimization via graph cuts," *Proceedings of the Seventh IEEE International Conference on Computer Vision*, vol. 1, pp. 377–384 vol.1, 1999.

[72] F.-C. Jeng and J. Woods, "Simulated annealing in compound gaussian random fields (image processing)," *IEEE Transactions on Information Theory*, vol. 36, no. 1, pp. 94–107, 1990.

[73] A. Majumder and S. Irani, "Contrast enhancement of images using human contrast sensitivity," pp. 69–76, 07 2006.

[74] K. Kapoor and S. Arora, "Colour image enhancement based on histogram equalization," *Electrical & Computer Engineering: An International Journal*, vol. 4, no. 3, pp. 73–82, 2015.

[75] W. Ren, L. Ma, J. Zhang, J. Pan, X. Cao, W. Liu, and M. Yang, "Gated fusion network for single image dehazing," *CoRR*, vol. abs/1804.00213, 2018.

[76] Y. Li, R. T. Tan, and M. S. Brown, "Nighttime haze removal with glow and multiple light colors," in *Proceedings of the IEEE international conference on computer vision*, pp. 226–234, 2015.

[77] J. Zhang, Y. Cao, S. Fang, Y. Kang, and C. W. Chen, "Fast haze removal for nighttime image using maximum reflectance prior," in *2017 IEEE Conference on Computer Vision and Pattern Recognition (CVPR)*, pp. 7016–7024, 2017.

[78] H. Koschmieder, "Theorie der horizontalensichtweite," *Beitr. Phys. Freien Atm., vol. 12*, pp. 171–181, 09 1924.

[79] J. Diaz-Cely, C. Arce-Lopera, J. C. Mena, and L. Quintero, "The effect of color channel representations on the transferability of convolutional neural networks," in *Advances in Computer Vision* (K. Arai and S. Kapoor, eds.), (Cham), pp. 27–38, Springer International Publishing, 2020.

[80] I. J. Goodfellow, D. Warde-Farley, M. Mirza, A. Courville, and Y. Bengio, "Maxout networks," in *Proceedings of the 30th International Conference on International Conference on Machine Learning - Volume 28*, ICML'13, p. III–1319–III–1327, JMLR.org, 2013.

[81] B. Cai, X. Xu, K. Jia, C. Qing, and D. Tao, "Dehazenet: An end-to-end system for single image haze removal," *IEEE Transactions on Image Processing*, vol. 25, no. 11, pp. 5187–5198, 2016.

[82] C. O. Ancuti, C. Ancuti, R. Timofte, and C. D. Vleeschouwer, "I-haze: a dehazing benchmark with real hazy and haze-free indoor images," in *arXiv:1804.05091v1*, 2018.

[83] C. O. Ancuti, C. Ancuti, R. Timofte, and C. De Vleeschouwer, "O-haze: A dehazing benchmark with real hazy and haze-free outdoor images," in *2018 IEEE/CVF Conference on Computer Vision and Pattern Recognition Workshops (CVPRW)*, pp. 867–8678, 2018.

[84] C. O. Ancuti, C. Ancuti, and R. Timofte, "NH-HAZE: an image dehazing benchmark with non-homogeneous hazy and haze-free images," in *Proceedings of the IEEE Conference on Computer Vision and Pattern Recognition Workshops*, IEEE CVPR 2020, 2020.

[85] C. O. Ancuti, C. Ancuti, M. Sbert, and R. Timofte, "Dense haze: A benchmark for image dehazing with dense-haze and haze-free images," in *IEEE International Conference on Image Processing (ICIP)*, IEEE ICIP 2019, 2019.

[86] S. Banerjee, P. Singha, P. Ghosh, and S. Chaudhuri, "Daytime and nighttime dehazing benchmarking database," in *Diary Number: 8997/2021-CO/L (Registered Copyright), Registration No. L-103093/2021*, 05 2021.

[87] C. Sammut and G. I. Webb, eds., *Mean Squared Error*, pp. 653–653. Boston, MA: Springer US, 2010.

[88] A. Hore and D. Ziou, "Image quality metrics: Psnr vs. ssim," in *2010 20th International Conference on Pattern Recognition*, pp. 2366–2369, 2010.

[89] Z. Wang, A. Bovik, H. Sheikh, and E. Simoncelli, "Image quality assessment: from error visibility to structural similarity," *IEEE Transactions on Image Processing*, vol. 13, no. 4, pp. 600–612, 2004.

[90] D. Berman, T. Treibitz, and S. Avidan, "Non-local image dehazing," in *2016 IEEE Conference on Computer Vision and Pattern Recognition (CVPR)*, pp. 1674–1682, 2016.

[91] B. Li, X. Peng, Z. Wang, J. Xu, and D. Feng, "An all-in-one network for dehazing and beyond," *CoRR*, vol. abs/1707.06543, 2017.

[92] V. Frants, S. Agaian, and K. Panetta, "Qcnn-h: Single-image dehazing using quaternion neural networks," *IEEE Transactions on Cybernetics*, pp. 1–11, 2023.

[93] L.-A. Tran, S. Moon, and D.-C. Park, "A novel encoder-decoder network with guided transmission map for single image dehazing," *Procedia Computer Science*, vol. 204, pp. 682–689, 2022. International Conference on Industry Sciences and Computer Science Innovation.

[94] W. Ren, S. Liu, H. Zhang, J. Pan, X. Cao, and M.-H. Yang, "Single image dehazing via multi-scale convolutional neural networks," in *Computer Vision – ECCV 2016* (B. Leibe, J. Matas, N. Sebe, and M. Welling, eds.), (Cham), pp. 154–169, Springer International Publishing, 2016.

[95] D. Chen, M. He, Q. Fan, J. Liao, L. Zhang, D. Hou, L. Yuan, and G. Hua, "Gated context aggregation network for image dehazing and deraining," *CoRR*, vol. abs/1811.08747, 2018.

[96] X. Liu, Y. Ma, Z. Shi, and J. Chen, "Griddehazenet: Attention-based multi-scale network for image dehazing," *CoRR*, vol. abs/1908.03245, 2019.

[97] H. Dong, J. Pan, L. Xiang, Z. Hu, X. Zhang, F. Wang, and M.-H. Yang, "Multi-scale boosted dehazing network with dense feature fusion," in *2020 IEEE/CVF Conference on Computer Vision and Pattern Recognition (CVPR)*, pp. 2154–2164, 2020.

[98] J. Dong and J. Pan, "Physics-based feature dehazing networks," in *Computer Vision – ECCV 2020: 16th European Conference, Glasgow, UK, August 23–28, 2020, Proceedings, Part XXX*, (Berlin, Heidelberg), p. 188–204, Springer-Verlag, 2020.

[99] X. Qin, Z. Wang, Y. Bai, X. Xie, and H. Jia, "Ffa-net: Feature fusion attention network for single image dehazing," *Proceedings of the AAAI Conference on Artificial Intelligence*, vol. 34, pp. 11908–11915, Apr. 2020.

[100] H. Wu, Y. Qu, S. Lin, J. Zhou, R. Qiao, Z. Zhang, Y. Xie, and L. Ma, "Contrastive learning for compact single image dehazing," *CoRR*, vol. abs/2104.09367, 2021.

[101] Y. Song, Z. He, H. Qian, and X. Du, "Vision transformers for single image dehazing," *arXiv preprint arXiv:2204.03883*, 2022.

[102] W.-L. Chen, C.-D. Kan, C.-H. Lin, Y.-S. Chen, and Y.-C. Mai, "Hypervolemia screening in predialysis healthcare for hemodialysis patients using fuzzy color reason analysis," vol. 13, p. 155014771668509, 01 2017.